NTNU

Norwegian University of
Science and Technology

Characterization of Substrate Binding and Hybrid Forming Abilities of Galectin-3

Sylvi Oliva Kjær

Chemical Engineering and Biotechnology
Submission date: June 2018
Supervisor: Marit Sletmoen, IBT

Norwegian University of Science and Technology
Department of Biotechnology and Food Science

Abstract

Glycans have over the last decade become a hot topic in biochemistry, cell biology and related research areas. Glycoproteins are today known to have critical roles in the organization and function of eukaryotic cells. Their incredible ability to store and display complex biological information, explains their crucial roles in a broad spectrum of cellular activities. However, their inherent complexity also raises great challenges in order for researchers to reveal their properties and many questions remain to be answered. Galectins are glycan binding proteins (GBP) that play important roles in interpreting and translating information expressed by glycans into appropriate responses. Understanding GBP - glycan interaction is considered a promising strategy to reveal the mysteries of glycans. In this study, the binding abilities of Galectin-3 in the wild type and the engineered homodimer form, was investigated using glycoproteins mucin-1 ST (MUC1(ST)) and asialofetuin (ASF) as ligands. The respective galectins and glycoproteins were immobilized on polystyrene beads and the inter-molecular binding force was quantified using optical tweezers. The results obtained in this study showed that interactions between Gal-3 WT and ASF, Gal-3 homodimer and ASF, Gal-3 WT and MUC1(ST) and Gal-3 homodimer - MUC1(ST) do form. Rupture forces were found to increase between 6.2 - 13.6 pN for loading rates between 45 - 158 pN/s for the Gal-3 WT – ASF system, between 10.1 - 28.1 pN for loading rates between 108 - 316 pN/s for Gal-3 homodimer – ASF, between 13.8 - 23.3 pN for loading rates between 63 - 213 pN/s for Gal-3 WT – MUC1(ST), and finally, between 8.8 - 28.6 pN for loading rates between 44 - 233 pN/s for Gal-3 homodimer - MUC1(ST). A slight difference in rupture force was observed between the two glycosylated proteins ASF and MUC1(ST). This difference might be explained by the different sugar moieties on the epitopes: LacNAc on ASF and Neu5Ac on MUC1(ST) or multiplicity due to the structural properties of the glycoproteins. In addition, the heterodimeric hybrid forming abilities of Gal-3 WT were investigated with the same approach, using Gal-1 WT and Gal-7 WT as ligands. It was found that Gal-3 WT seems to exhibit a certain inherent specificity to both galectins. Still, a lot is yet to be revealed related to *in vivo* behaviour of Gal-3, where research suggests multivalency to be a key feature. Furthermore, the hybrid forming abilities of galectins may potentially influence our future interpretation of galectin behaviour.

Sammendrag

Glykaner har det siste tiåret blitt et populært tema innenfor biokjemi, cellebiologi og andre relaterte forskningsområder. Glykoproteiner er i dag kjent for å ha en kritiske roller i organiseringen og funksjonaliteten til eukaryote celler. Deres utrolige evne til å lagre og vise kompleks biologisk informasjon, forklarer deres avgjørende rolle i et bredt spekter av cellulære aktiviteter. Glykoproteinenes iboende kompleksitet skaper også store utfordringer med å utforske deres egenskaper; mange ubesvarte spørsmål gjenstår. Galektiner er glykanbindende proteiner (GBP) som spiller viktige roller i å tolke og oversette informasjon uttrykt av glykaner til passende responser. Å forstå GBP - glykan interaksjoner er ansett som en lovende strategi for å avsløre glykanenes mysterier. I denne studien er bindingsevnen til Galektin-3 i villtype og homodimer formen blitt undersøkt ved bruk av glykoproteinene mucin-1 (ST) og asialofetuin som ligander. De respektive galektinene og glykoproteinene ble immobilisert på polystyrenkuler, og den intermolekylære bindingsstyrken ble kvantifisert ved bruk av optisk pinsett. I denne studien ble det oppnådd resultater som viste at interaksjoner mellom Gal-3 WT og ASG, Gal-3 homodimer og ASF, Gal-3 WT og MUC1(ST) og Gal-3 homodimer - MUC1(ST), oppstod. Det ble funnet at bruddstyrkerene økte mellom 6.2 - 13.6 pN for kraftlastrater mellom 45 - 158 pN/s for Gal-3 WT – ASF systemet, mellom 10.1 - 28.1 pN for kraftlastrater mellom 108 - 316 pN/s for Gal-3 homodimer – ASF, mellom 13.8 - 23.3 pN for kraftlastrater mellom 63 - 213 pN/s for Gal-3 WT – MUC1(ST), og mellom 8.8 - 28.6 pN for kraftlastrater mellom 44 - 233 pN/s for Gal-3 homodimer - MUC1(ST). En liten forskjell i bruddstyrke ble observert mellom de to glykoproteinene ASF og MUC1(ST). Denne forskjellen kan kanskje forklares av de forskjellige sukkermonomerene på epitopene: LacNAc på ASF og Neu5Ac på MUC1(S), eller multiplisiteten på grunn av strukturegenskapene til glykoproteinene. I tillegg ble de heterodimeriske hybrid-dannende evnene til Gal-3 WT undersøkt med samme fremgangsmåte, ved bruk av Gal-1 og Gal-3 som ligander. Det ble funnet at Gal-3 WT virker å inneha en iboende spesifisitet til begge galektinene. Det gjenstår fortsatt mye å avdekke relatert til *in vivo* oppførsel, hvor forskere mistenker multivalens for å være en nøkkelfunksjon. Videre kan potensielt de hybrid-dannende evnene til galektiner påvirke vår fremtidige tolkning av galektiners oppførsel.

Preface

This master thesis is submitted to the Department of Biotechnology and Food Science at the Norwegian University of Science and Technology (NTNU), and constitutes final work of the Master of Science in Chemical Engineering and Biotechnology. This master thesis is a continuation of the TBT4500 Biotechnology, Specialization Project titled "Characterization of substrate binding abilities of galectin-3" written fall 2017, hence, the work for this thesis has been executed from August 2017 to June 2018. The experiments were carried out in the laboratories at the Department Biotechnology and Food Science at NTNU. All figures except the one illustrating the optical tweezers instrument, are self made in Inkscape.

First of all, I would like to direct a major thanks to my supervisor Associate Professor Marit Sletmoen for great feedback, suggestions, and helpful conversations throughout the year.

I would also like to thank Professor Hans-Joachim Gabius at the Ludwig-Maximilians University, Munich, for providing samples and suggestions to interesting problems in the start and along the way.

Last but not least, I would like to thank friends and family for all love and support.

S-squad, I'm very grateful for our many lunch hours together with sharing whatever coming to our minds, all of our good and tough times.

Hydrogenjentene, its been a pleasure to share this journey with you.

Contents

Abstract i

Sammendrag ii

Preface iv

Abbreviations ix

Symbols xi

1 Introduction 1

2 Theory 3
2.1 Glycobiology . . . 4
2.1.1 Ligands for Galectin-3 studied in this thesis . . . 5
2.1.2 Lectins . . . 6
2.2 Methods important for the progress within the field of glycobiology 9
2.2.1 Glycan arrays . . . 10
2.2.2 Structure determination of glycoconjugates . . . 10
2.2.3 Sensitive force probes . . . 13
2.3 Force measurements on the single molecular level . . . 16
2.3.1 Dynamic force spectrum . . . 17

3 Materials and Methods 21
3.1 Materials . . . 22
3.2 Immobilization of proteins on polystyrene beads . . . 22
3.3 Preparation of the liquid cell . . . 23
3.4 The set up of the optical tweezers . . . 24
3.5 Calibration of the OT . . . 24
3.6 Data collection using OT . . . 25
3.7 Processing of data obtained using OT . . . 26

4 Results 29
4.1 Gal-3 interaction abilities . . . 30
4.2 Experimental data for Gal-3 - glycoprotein interactions . . . 33
4.2.1 Gal-3 WT - ASF . . . 33
4.2.2 Gal-3 homodimer - ASF . . . 38
4.2.3 Gal-3 WT - MUC1(ST) . . . 42

4.2.4 Gal-3 homodimer - MUC1(ST) 46
4.2.5 Parameters characterizing Gal-3 - glycoprotein interactions . 49
4.3 Hybrid formation in binary mixtures of galectins 53
4.3.1 Gal-3 WT - Gal-1 WT 53
4.3.2 Gal-3 WT - Gal-7 WT 57
4.3.3 Parameters characterizing Gal-3 - galectin interactions . . . 61

5 Discussion **63**
5.1 Interaction abilities of Gal-3 WT 64
5.2 Gal-3 - glycoprotein interaction and multivalency 65
5.3 Comparison of the interaction characteristics of the Gal-3 - glycoprotein systems studied 68
5.4 Hybrid forming abilities of Gal-3 WT 70
5.5 Evaluation of the suitability of the Bell-Evans model in the current study 71
5.6 Evaluation of optical tweezers as a tool to study glycan-lectin interactions 72

Conclusion **75**

A Interaction frequency data **81**

B DFS box plots **83**

Abbreviations

AFM	Atomic force microscope
ASF	Asialofetuin
BSA	Bovine serum albumin
CRD	Carbohydrate recognition domain
DFS	Dynamic force spectrum
Gal	Galactose
Gal-1	Galectin-1
Gal-3	Galectin-3
Gal-7	Galectin-7
GBP	Glycan binding protein
GlcNAc	N-Acetylglucosamine
IgG	Immunoglobulin G
LacNAc	N-acetyllactosamine
MS	Mass spectrometer
MUC1	Mucin-1
Neu5Ac	N-Acetylneuraminic acid
NMR	Nuclear magnetic resonance
NOE	Nuclear Overhauser effect
OT	Optical tweezers
Ser	Serine
Siglec	Sialic acid-binding Ig-like lectin
ST	α-Neu5Ac(2,3)β-Gal(1,3)-GalNAc-Ser/Thr
Thr	Theronine
WT	Wild type

Symbols

β	sensitivity constant	-
f*	Most likely rupture force	N
r_f	Loading rate	N/s
k_{off}	Dissociation rate	s^{-1}
x_β	Distance between bound and unbound state in energy landscape	m
τ	Lifetime	s
P_{int}	Intraction frequency	%
ΔG^u	Gibbs free unbinding energy	J

Chapter 1

Introduction

The role of sugars as a nutrient has been common knowledge for decades, however, the role of sugars as a major information carrier in cell biology, is a relatively new thought. Monosaccharides possess the incredible ability to assemble into extremely complex oligosaccharides as a result of their many linking opportunities, orientation dependency and branching ability. Through glycosylation proteins, lipids and peptides become heavily and carefully decorated with chains of sugars, creating highly complex structures. Because of the large amount of information that can potentially be transferred by one single glycoconjugate, they make perfect candidates as messengers on the dense cell surface. Today, a lot still remains to reveal the significance of glycans in the cell world. To fully understand the functions of glycans and decode the "sugar code", deeper knowledge about the interpreters of the information stored in glycan structures: i.e. glycan binding proteins(GBP), is required. Galectin-3 is a β-galactoside specific GBP involved in a variety of biological activities, including cell adhesion, apoptosis and cell differentiation. It has also been found to play a prominent role in pathogenesis and cancer progression. In this study, Gal-3 is to be further investigated through comparing the binding ability of two structural forms of Gal-3: wild type and homodimer, to bind two different glycoproteins: asialofetuin and mucin1-ST. In addition, the ability of Gal-3 to interact with other galectins and potentially form heterodimeric hybrids is also to be investigated using Gal-1 WT and Gal-7 as ligands. Optical tweezers are used to quantify the inter-molecular force prior to bond rupture. The aim of this study is to improve our understanding of the ligand binding and hybrid forming abilities of Gal-3.

This master thesis is a continuation of a specialization project written fall 2017 for the department of biotechnology and food science at NTNU.

Chapter 2

Theory

This chapter provides an introduction to the most relevant topics to give a theoretical basis needed for understanding the principles discussed later in the thesis. The first part of the text is an introduction to glycobiology, with emphasis on the glycans and lectins studied in this thesis. The second part of the theory is an introduction to methods that have been important for progress within the field of glycobiology and how information is obtained from some of these methods.

2.1 Glycobiology

Glycobiology can in the broadest sense be defined as the study of the structure, biosynthesis, biology and evolution of saccharides and the proteins that recognize them (Cummings *et al.* 2017). These monosaccharides and oligosaccharides are generally termed "glycans", and are the most abundant organic polymer in the biosphere and essential for all living organisms. Their role in the biological world is especially prominent in the context of communication and interaction between cells and the surrounding matrix. Hence, glycans are highly present on the cell surface where they are typically appear as glycoconjugates. Through the biological process of glycosyltaion, glycans get covalently linked to other biological molecules, typically lipids and proteins, resulting in glycoconjugates. Together, these glycoconjugates make up a layer on the cell surface generally termed the "glycocalyx". It ranges between 10 - 1000 nm in thickness up into the extracellular space and is responsible for the most complex biological processes in a cell as cell motility, cell-cell binding and signal transduction. These glycoconjugates can be broadly classified into glycolipids, proteoglycans and glycoproteins, illustrated in Figure 2.1.

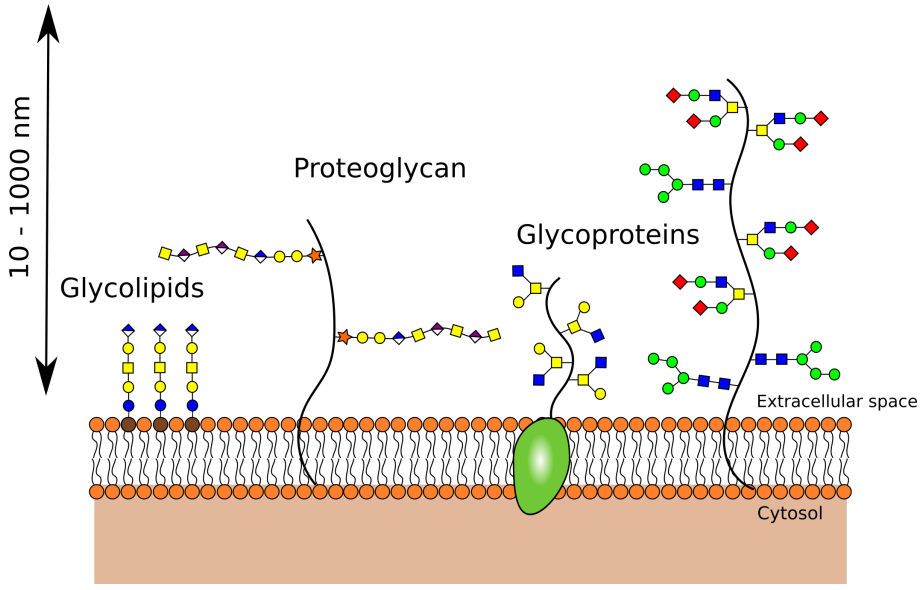

Figure 2.1: Simplified illustration of the classes of glycoconjugates found on the cell surface, together making up the 10-1000 nm thick glycocalyx.

Glycans and glycoconjugates exhibit properties which qualifies them as ultimate information carriers (Gabius 2009). Due to a high variety of different monosaccharides (monomers), their many linking possibilities into oligosaccharides, and the further possibility of multiple oligosaccharides branching from one single glycoconjugate, enables an incredible structural variety. Thus, the density of information that can be achieved by oligosaccharides is much higher compared to linear biomolecules as oligopeptides and oligonucleotides.

This complexity is also reflected in the glycan binding proteins (GBP); to "read" advanced messages requires advanced "readers". GBPs are essential for interpreting and conducting the information glycans express. One way of doing this is through multivalent interactions with glycan ligands. This multivalency enhances binding to the ligands through increased avidity and allows ligand cross-linking through multiple CRDs, making investigation of glycan interactions extremely difficult and complex.

2.1.1 Ligands for Galectin-3 studied in this thesis

Glycoconjugates further investigated in the current study are two human glycoproteins: mucin-1 (ST) (MUC1(ST)) and asialofetuin (ASF). Both are well characterized and commonly used in glycobiology studies (Spiro 1973, Corfield 2015).

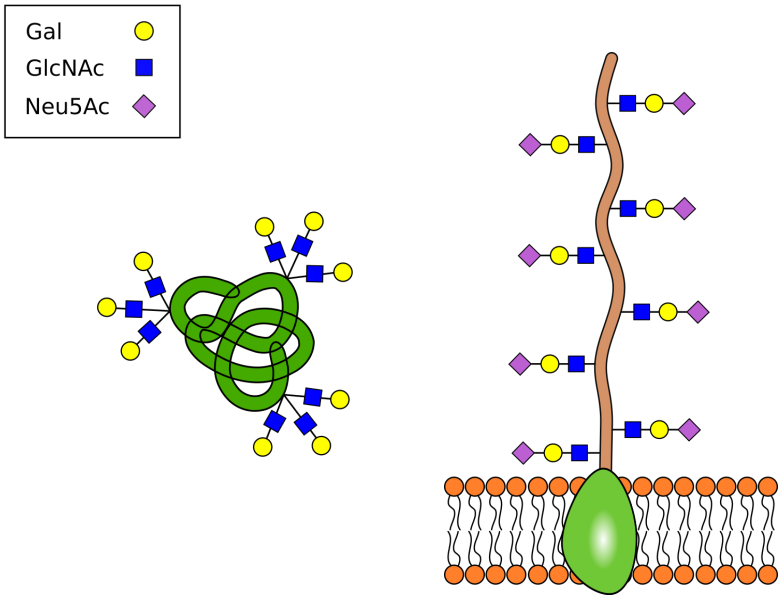

(a) Asialofetuin **(b)** Mucin-1 (ST)

Figure 2.2: Simplified illustration of the structures of the two glycoconjugates used as ligands for Gal-3 in this study: (a) Asialofetuin and (b) Mucin-1 (ST)).

Asialofetuin (ASF)

Asialofetuin (ASF) is a multivalent, globular glycoprotein expressing nine LacNAc epitopes (Figure 2.2a) found to interact with Gal-3 (Dam *et al.* 2005). Fetuins are proteins abundantly found in animal fetal serum and is commercially extracted from fetal calf serum (Spiro 1973). ASF is one of the main ligands to the Asialoglycoprotein receptor (c-type lectin), which is found primarily on hepatocytes in the human liver (Stockert 1995). Because of this property, ASF has been investigated for use in gene therapy aimed on the liver (Farinha *et al.* 2014). It is widely used as a "standard"- ligand in studies of galectins.

Mucin-1

MUC1 is a linear, transmembrane glycoprotein found on epithelial cells in lung tissue, abdomen, small intestine and breast tissue (Cummings *et al.* 2017). In healthy cells, MUC1 glycoconjugates are randomly and heavily O-glycosylated. However, an interesting discovery is when the cells becomes cancerous the core-structure changes as well as the glycosylation pattern from elongated to shorter structures (Burchell *et al.* 2001). These changes generate novel cancer-specific glyco-antigens, one of these glyco-epitopes expressed by carcinomas is ST (α-Neu5Ac(2,3)β-Gal(1,3)-GalNAc-Ser/Thr), illustrated in Figure 2.2b, which is the MUC1 variant used in this study.

2.1.2 Lectins

Lectins are glycan-binding proteins found in all living organisms (Cummings *et al.* 2017). They can be considered as bridges between proteomics and glycomics because of their ability to interpret and translate the information expressed by the glycan structures into appropriate responses (Belardi and Bertozzi 2015, Gabius and Roth 2017, Solís *et al.* 2015, Gabius 2009). Lectins play many roles in biological processes involving interactions resulting in movement of molecules, cells and information (Cummings *et al.* 2017). Their main functional areas are cell adhesion, movement of proteins, immunity and infection. They can exist both within aggregates or as separate proteins. Due to topological factors, which form they exist in can affect their avidity and selectivity to their ligands (Manning *et al.* 2017). Affinity also depends on the structure of the ligand: monosaccharides or small oligosaccharides are typically low-affinity ligands, whilst bigger and more complex glycans typically binds with higher affinities, often due to multivalency. There are several classes of lectins. They are classified into different evolutionary-related families based on the primary and three-dimensional structural similarities of the carbohydrate-recognition domain (CRD).
The most widely expressed class within animal lectin families are galectins. Galectins are characterized by their specific binding affinity to β-galactose sugars (Cummings *et al.* 2017, Klyosov 2008). They are produced by a variety of cell types and can be found both intra- and extracellularly in animals. Galectins can be

further classified into prototypical galectins, containing one single CRD that may associate as dimers, chimera type galectin, characterized by a single CRD with a amino-terminal polypeptide "tail", and tandem-repeat galectins, recognized by having two CRDs connected by a peptide linker (Figure 2.3). Galectins with multiple CRDs have a natural multivalency contributing to complex and high affinity binding to their ligands. Galectins exerts a remarkable diversification of

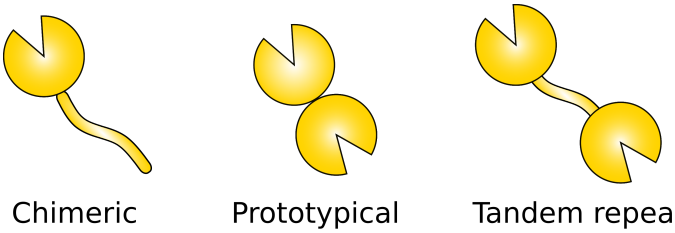

Figure 2.3: Illustration of the three classes of galectins: prototypical, chimeric and tandem repeat.

roles in biological processes, e.g. cancer development, cell-cell interactions, tissue-regeneration, pre-mRNA splicing, immune homeostasis and recognition functions against potential pathogens, some of these are illustrated in Figure 2.4.

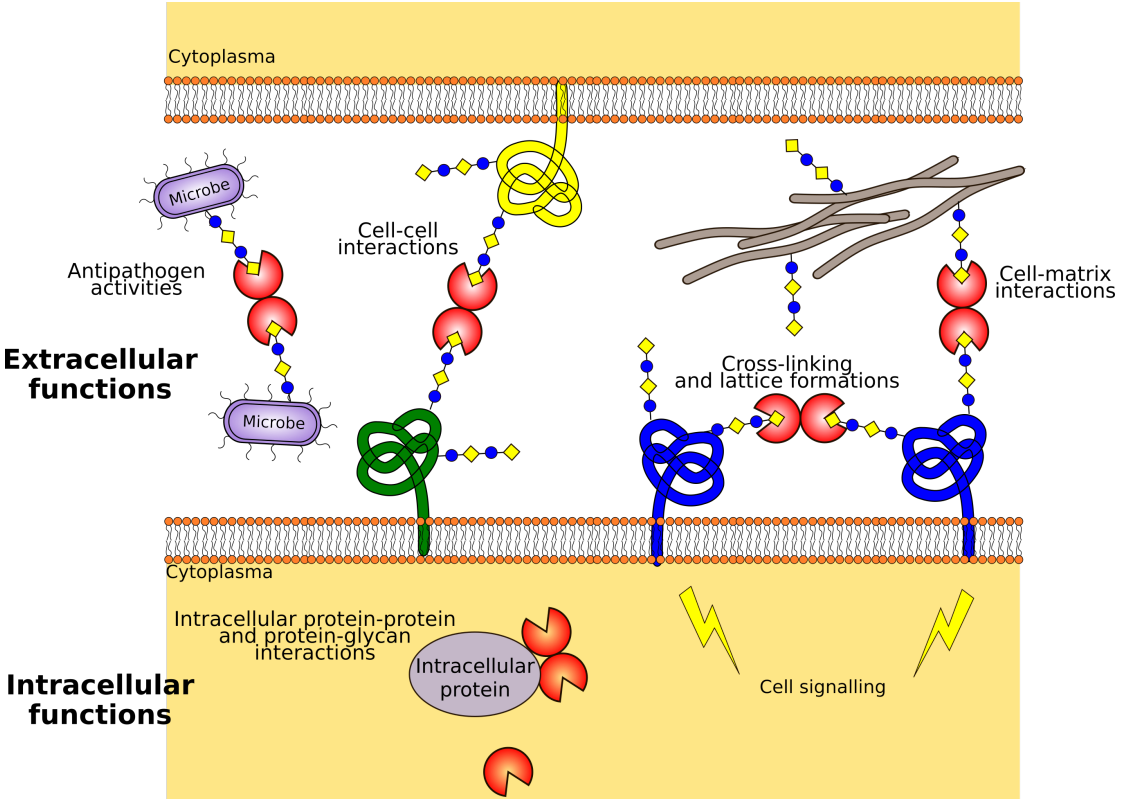

Figure 2.4: Illustration of the some main intra- and extracellular functions of lectins illustrated with a galectin dimer.

Galectin 3

Gal-3 a is member of the galectin family and is recognized by its binding specificity to β-galactosides and evolutionary amino acid sequences (Dumic *et al.* 2006, Ruvolo 2016). Gal-3 is unique among the galectins because of its N-terminal domain structure, making it the only vertebrate chimera type of lectin (Figure 2.5). The N-terminal domain is composed of 110 - 130 amino acids forming a relatively flexible collagen-like structure rich in proline and glycine. Although this domain has been shown to lack carbohydrate-binding activity, it allows the galectin to form pentamer structures, giving rise to the multivalency of Gal-3 (Figure 2.5) (Nisar Ahmad *et al.* 2004).
The second domain of the Gal-3 structure is the C-terminal domain. It consists of 130 amino acids forming a globular structure and is the location of the carbohydrate-recognition site, which is responsible for the lectin activity. However, importance of the N-termial domain in self-association and ligand binding has been discussed as trucated Gal-3 (Gal-3 CRD) is found to be present *in vivo*, as a result of cleavage of Gal-3 by proteases (Yang *et al.* 1998, Kuklinski and Probstmeier 1998). Recent research also reveal that the C-terminal domain seems to attach to neutrophils with approximately same affinity as the intact Gal-3, and even the attachment of one of them increases by presence of the other (Sundqvist *et al.* 2018, Ahmad *et al.* 2004).

Binding to a ligand is achieved through a conformational change and rearrangement of the backbone loops near the binding site. The sugar binding affinity is strongly affected by phosphorylation at the position Ser^6 and is proposed to act as an on/off switch of its downstream biological effects. Gal-3 is involved in sev-

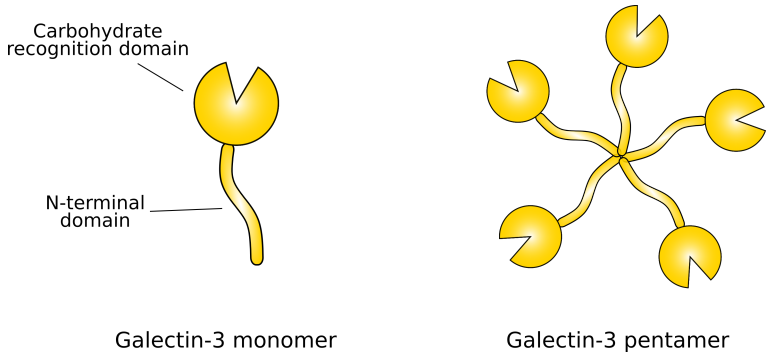

Figure 2.5: Illustration of Galectin-3 protein in its two structural forms: monomer and pentamer.

eral biological activities such as apoptosis, cell differentiation, cell adhesion, cell activation, chemoattraction, cell cycle progression, mRNA splicing and immune responses (Dumic *et al.* 2006, Cummings *et al.* 2017). Given its broad functionality, Gal-3 has been found to be a key molecule in the progression of tumors and generally prominent in the tumor microenvironment (Ruvolo 2016). Extended research has been executed concerning Gal-3 as a significant factor in specific cancer types, especially melanoma, colon and breast cancer types (Brown *et al.* 2012, Kim *et al.* 1999, Serizawa *et al.* 2013, Sciacchitano *et al.* 2018). The progression

of these forms of cancer are characterized by overexpression and changes in localization of the galectin. A property of Gal-3 which is particularly prominent in cancer progression, is the pro and anti apoptotic activity (Nakahara *et al.* 2005). By inducing T-cell apoptosis, Gal-3 promotes cancer cell survival and thus tumor growth. Gal-3 has also been found to be a important factor in metastasis (Takenaka *et al.* 2002).

2.2 Methods important for the progress within the field of glycobiology

Progress within a research field and available methods and tools, depend heavily on each other; breakthroughs can be obtained with the right methods, and new methods can be developed as a consequence of new discoveries. In the case of glycobiology, the progression rate has increased significantly over a relatively short time span. For a long time this field gained only limited interest within the research community, but over time it has become one of the most rapidly developing fields in natural sciences (Cummings *et al.* 2017).

Carbohydrates first gained attention in the first part of the 20th century, but at that time primarily as a source of energy and as structural material. When the molecular biology revolution came in the 1970s, glycan research already lagged far behind and not until the late 1980s, was "glycobiology" for the first time introduced as a term that designated the merge of the traditional carbohydrate chemistry and biochemistry disciplines, which was based on new thoughts about the role of glycans in cell biology. This was a milestone in glycan research which emphasized their biological role and the progress started to accelerate. Reasons why the research in the glycobiology field lagged behind in the start are partly because of the inherent structural complexity of glycans and partly also because of a lack of suitable tools available for researchers at the time. Today, however, a range of methods are available for studying glycans and glycan interactions. The main areas in glycan studies include specificity and affinity analysis, structure analysis and chemical synthesis of glycans.

For structural analysis, mass spectroscopy (MS) and nuclear magnetic resonance (NMR) spectroscopy are the most traditionally and commonly used research tools. In the case of specificity and affinity studies new methods has been developed relatively fast. Traditionally, methods as isothermal calorimetry (ITC), surface plasmon resonance (SPR) and enzyme-linked lectin assays (ELLAs) have been used (Oyelaran and Gildersleeve 2009). However, these methods typically only provide information about the monovalent interactions between a single carbohydrate ligand and a single-binding domain of the protein. As mentioned, GBPs often possess two or more binding sites, opening for multiple interaction and increased bond strength and lifetime. Hence, to more correctly evaluate and interpret glycan interactions and their biological effects, glycans should be displayed and studied in a scenario closer to what is found in the cellular environment. This includes

improved mimicking of the molecular organization (including their spacing) down to a nanometer scale. Glycan arrays and sensitive force probes are examples of methods which can assist in obtaining this goal. Following is an introduction to these methods currently important for the progress in the glycobiology field, why they are important and their basic working principle.

2.2.1 Glycan arrays

More recent methods for studying glycan interactions are through glycan arrays (Liang and Wu 2009, Oyelaran and Gildersleeve 2009). Glycan arrays have already become very important research tools in the field of glycosciences since the first type was introduced in 1986 (Dosekova *et al.* 2016). The concept behind the glycan array technology, is to immobilize glycan biomolecules to a solid support in a spatially defined arrangement. With array technology, many of the earlier challenges associated with the traditional methods are overcome; this new technique is both low-cost and a high-throughput methology for screening glycan interactions, using only fractions of the amount of each carbohydrate compared to the traditional methods (Liang and Wu 2009). They also provides the possibility to probe hundreds of receptor-ligand interactions in one single experiment. The main advantage of this array-based technique is the multivalent presentation of arrayed glycans, which can resemble the actual cell surface and thus gives a more realistic environment to study real glycan-mediated interactions as they appear in nature (Huang and Godula 2016).

Despite recent important advances in the use and fabrication of glycan arrays, some challenges still remain. To achieve high avidity multivalent binding, the spacing and orientation of the carbohydrate ligands is critical. This can be optimized by changing parameters as concentrations and type of linker between the glycan and the solid surface during the preparation step (Oyelaran and Gildersleeve 2009).

2.2.2 Structure determination of glycoconjugates

Knowledge related to the structure of the glycan is useful when aiming at elucidating their function (Cummings *et al.* 2017). For glycoconjugates, the function often heavily depends on their oligosaccharide structures. The growing interest of the glycobiology field has been an important driving force in developing methods for addressing questions relating to structure and stereochemistry, and the fast evolution in the field is also a consequence of this. As mentioned earlier, the structure of glycans can be extremely complex and in contrast to the synthesis of the linear molecules DNA, RNA and proteins, glycans are synthesized in a non-template fashion and are usually branched. The final structure of the glycan depends on different factors such as enzymatic activity, compartment in cell and state of the cell. Hence, it is impossible to predict the glycan expression of a cell and this makes structure analysis a challenge. Thus, glycan analysis often requires several steps of iterative combinations of physical, chemical, and enzymatic approaches in order

to get insight into the detailed complete structure, as simplified schematically in Figure 2.6.

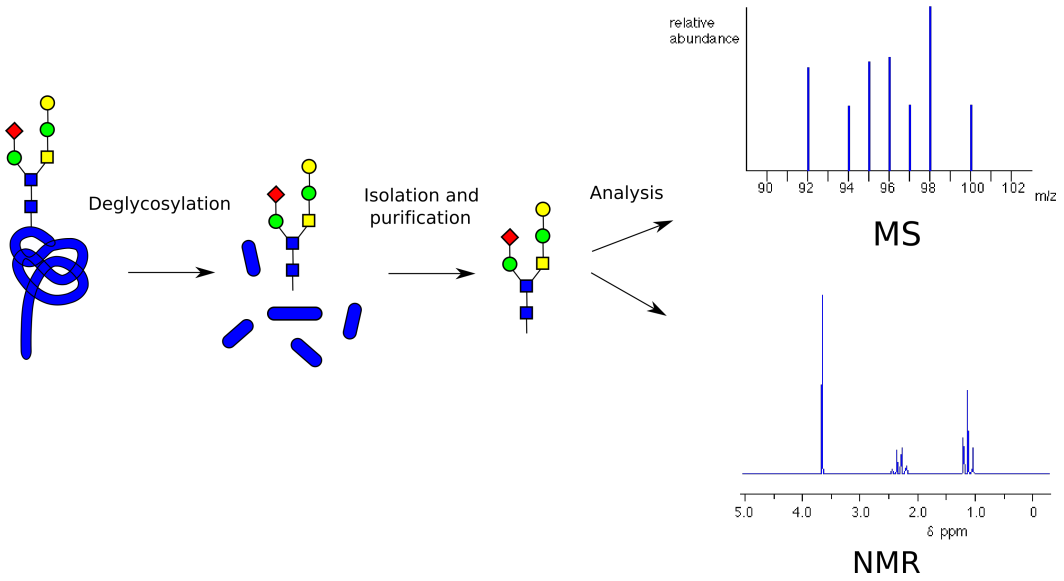

Figure 2.6: Simplified schematic overview of the typical steps in structure analysis of glycans.

Today, oligosaccharide analysis relies increasingly on MS and high resolution NMR spectroscopy. These techniques are therefore further explained in the following.

Mass spectroscopy

MS is currently the primary high sensitive technique for characterizing the nature of a small quantity of individual glycans (Cummings *et al.* 2017). The principle of MS is production and detection of ions separated according to their mass to charge (m/z) ratios (Han and Costello 2013). The detection of the ions results in a mass spectrum showing the relative abundance of the ions detected as a function of their m/z-ratio, based on this, the mass can be calculated with very high precision. The instrument consists of four parts, each being responsible for one essential process: ionization, acceleration, deflection and detection as illustrated in Figure 2.7. The sample is injected in the ionization part where it gets heated until vaporization and then ionized by an electron source. The ionized sample then gets accelerated before entering a magnetic field which separates the ions based on the m/z-ratio. The detection of the ions results in a mass spectrum which can be further analyzed, and the molecules identified. One of the main advantages with the MS is that one singe analysis gives a high amount of information about which glycans are present and their relative abundance. MS is typically the last step in glycan characterization and either purified glycans or glycans attached to protein (glycopeptides) fragments can be analyzed depending on the sample or desired output.

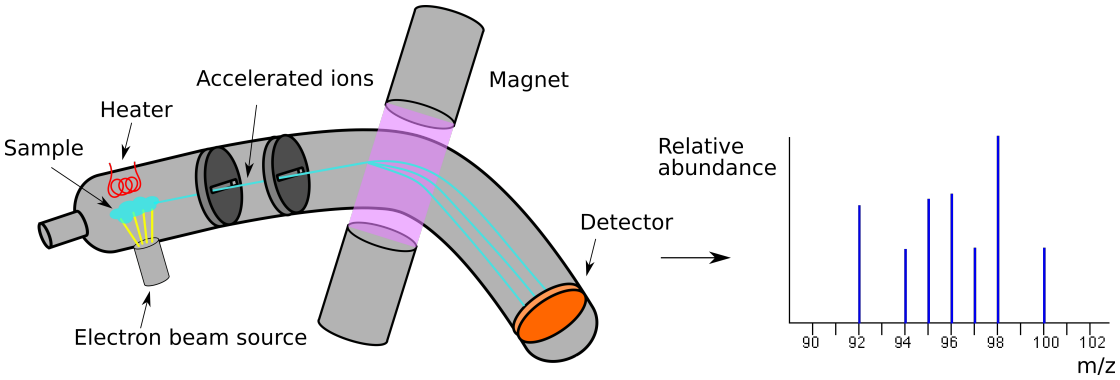

Figure 2.7: Schematic illustration of the basic principle of a mass spectrometer. A sample is vaporized by the heater and ionized by an electron beam source. The ions are accelerated through two slits before entering the deflection part where they are exposed to a strong magnetic field which separates the ions based on mass to charge ratio. A detector records the ion as they collide and a mass spectrum of the relative abundance of the molecules in the sample is generated.

Nuclear magnetic resonance

NMR spectroscopy is also a powerful tool in glycan characterization by allowing detailed structural information of both purified glycans and glycan mixtures (Cummings *et al.* 2017). NMR spectroscopy takes advantage of the quantum mechanical property of the atomic nuclei: nuclear spin angular momentum (Nelson 2013). The nuclear spin generates a magnetic dipole which, when exposed to a strong, static magnetic field as in NMR spectroscopy, align in the field either parallel (low energy) or antiparallel (high energy) relative to the field. A short pulse of electromagnetic energy of suitable frequency (typical radio frequency length) is then applied in right angles relative to the nuclei (aligned in the magnetic field), and an absorption spectrum is then generated as some of this energy gets absorbed when nuclei switch to the high-energy state. By repeating the experiment, the data is averaged resulting in increased signal-to-noise ratio and a final NMR spectrum of the sample is generated through Fourier transformation. This is schematically illustrated i Figure 2.8. The generated spectrum reveals information about the identity of the nuclei and their immediate chemical environment. Through NMR structural analysis of oligosaccharides, three parameters are determined based on the NMR spectra to characterize the structure: chemical shifts, nuclear Overhauser effects (NOEs) and coupling constants (Battistel *et al.* 2014). The chemical shift is the resonance frequency of a nucleus relative to a standard in the magnetic field. Chemical shift values depend on the chemical environment of the nucleus giving rise to the signal, typically electron densities. The parameter is denoted δ, ppm, and denotes the x-axis of the NMR spectrum. Certain chemical environments have distinct chemical shifts and can thus easily be identified in a NMR spectrum, e.g. primary alkyl group in 1H NMR. Coupling arises between a pair of nuclei from the interaction of the magnetic dipoles between them. Typically coupling observed in NMR spectra are within 2-3 bonds away from the nucleus producing the signal, resulting in splitting of the signal into multiple peaks. The coupling constant

is especially important for determining ring conformations and thus characterizing monosaccharides, and the overall conformational shape of oligosaccharides in solution.

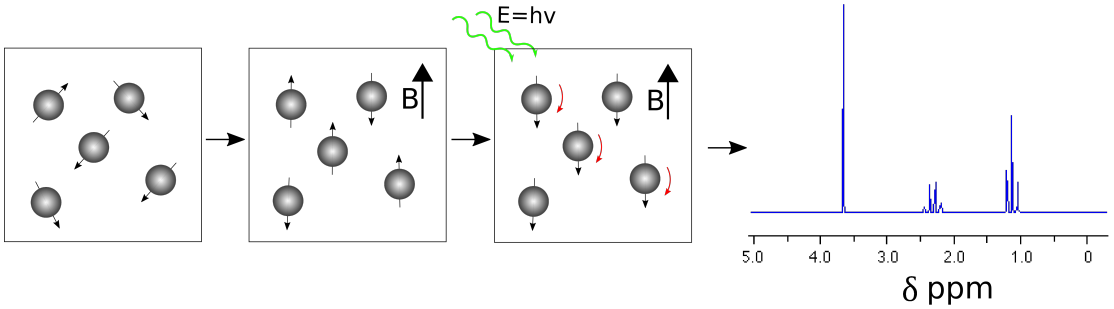

Figure 2.8: Schematic illustration of the basic principle of nuclear magnetic resonance spectroscopy. Atomic nuclei possess the property of spin which generates a magnetic dipole. When exposed to a strong, static magnetic field, B, the nuclei align either parallel (low energy) or antiparallel (high energy) with B. A short pulse of electromagnetic energy, E, is then applied which is absorbed by the low energy nuclei making them switch to the high energy state. This results in a NMR spectrum.

NOEs denotes/describes an effect on intensities of resonance in NMR spectra that is often related to internuclear distances. In contrast to coupling, NOE occurs in space not through chemical bonds and can appear over longer distances than coupling. That way, NOE contains more information about nuclei located further away. NOE is an especially important parameter in computational modeling of 3D structures of the glycan.

Using NMR information, it is therefore possible to determine the sequence, linkage position and anomeric carbon configuration of glycans. As data bases are developed and increases in size, characterization will get more and more efficient. However, some limitations are still associated to NMR spectroscopy; the sensitivity of the instrument is both an advantage and a disadvantage. Because of the sensitivity the instruments typically require several nanomoles of glycan for even the simplest structure experiment. NMR spectrometers are also relatively high in cost and the level of expertise required for interpreting NMR spectra is high.

2.2.3 Sensitive force probes

Sensitive force probes is another method that is currently relevant in the progress of the glycobiology field (Neuman and Nagy 2008). Every process on the cell surface, including glycan interactions, involves molecular forces in different forms; hydrophobic, hydrophilic, electrostatic, van der Waals and hydrogen interactions. Force probes/spectroscopy is a method which can be used to quantify the sum of these forces that occurs during a single glycan interaction. By quantifying these forces, properties such as lifetime and energy landscape can be obtained for the

specific interaction. The two most commonly used instruments to obtain this information are atomic force microscopy (AFM) and optical tweezers (OT), which will be presented in the following.

Atomic force microscopy measurements

In many ways, the invention of the AFM in 1986 is considered to be the start of the nanotechnology as a scientific discipline (Dosekova *et al.* 2016). For the first time, surface characteristics could be mapped with sub-nanometer resolution using a proximal probe. Up to this point, mapping of nanoscale surface structures was highly limited due to the lack of appropriate imaging techniques (Neuman and Nagy 2008). The AFM consists of three main components: the cantilever with a sharp tip, the piezoelectric scanning sample stage and the optical deflection system consisting of a laser diode and a photodetector as illustrated in Figure 2.9. Images of the sample surface are created when scanning the surface in both x- and y-direction with the sharp tip, using the interaction force between the tip and the sample to probe the topography of the surface.

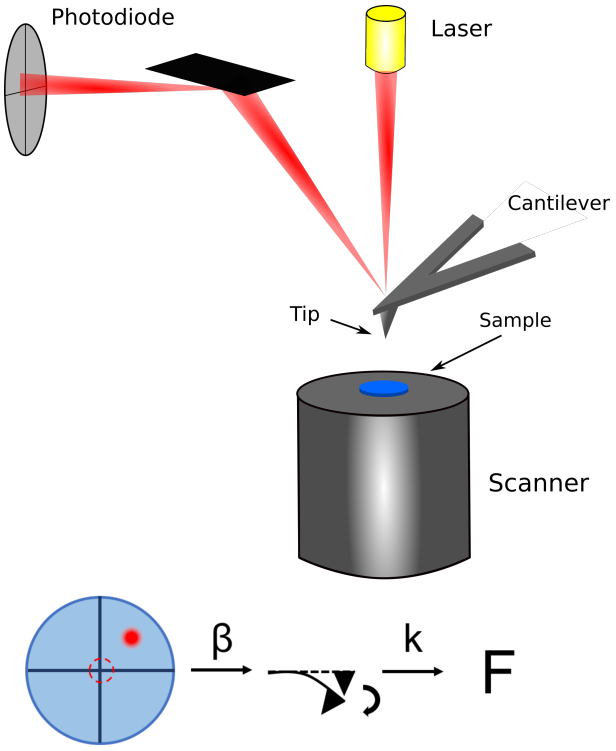

Figure 2.9: Schematic illustration of the general principle of the atomic force microscope. Imaging is performed by bringing the sharp tip in physical contact with the sample surface to enable interaction. By retracting the sharp tip from the surface, the change in position of the cantilever due to interaction forces, causes a relative change in the position of the reflected laser, detected by a quadratic photodiode. Volt signal from the detector is translated into Force through the conversion factors β and k, obtained from calibration.

The interaction force is determined by the displacement of the tip in z-direction detected by the reflection of the laser beam off the cantilever onto the photodetector. The photodetector is divided into 4 identical quadrants, each sensing the relative change in position of the deflection from the equilibrium position. The cantilever can be considered as a spring system with spring constant k. The volt signal generated from the photodiode due to the bending of the cantilever and thus displacement of the tip is directly proportional to the force. During calibration, a sensitivity constant, β, and the spring constant, k, is determined, and from these, the volt signal can easily be converted to force as illustrated in Figure 2.9.

The instrument has a variety of applications. It was initially intended to overcome limitations of the scanning tunneling microscope in imaging nonconductive samples (Neuman and Nagy 2008). But was soon found to be a powerful tool in cell biology research, as a glycan array. Its ability to detect incredibly small interaction forces, has led to new opportunities in studying macromolecule interactions in the cell biology world. For the first time it was possible to achieve nanometer-scale details of the living cell, organelles and biomolecules, which was previously impossible due to resolution limitations of light microscopes. Its unique features also allows researchers to study interactions in near physiological conditions, which is one of the main advantage of glycan arrays.

Optical Tweezers

OT was developed by Arthur Ashkin after detecting optical gradient and scattering forces on micron sized particles in 1970 (Ashkin 1970). The working principle of OT, also called gradient force trap, is using lasers to stably trap and immobilize dielectric particles in three dimensions (Neuman and Block 2004). The optical trap is formed when a laser is focused to a diffraction-limited spot with a high numerical aperture microscope objective. A dielectric particle in a trap is exposed to two force components responsible for three-dimensional trapping: the scattering and gradient force. The scattering force works in the direction of light propagation and the gradient force in the direction of the spatial light gradient. When the photons and dielectric particle collide, are parts of the momentum carried by the photons transferred to the particle resulting in a trapping force that the particle is experiencing. For the trap to be stable in all directions, the gradient forces must exceed the scattering forces. Only then is the forces that push the particle towards the focal region larger than the forces pushing it away from that region, resulting in the particle to be trapped. This strong gradient force can be achieved by focusing the laser sharply, for this a microscope with high numerical aperture is required (Moffitt *et al.* 2008).

Correct and precise calibration of the trap is essential to achieve accurate force and position measurements (Neuman and Block 2004). Similarly to the AFM, is the displacement of the particles detected by a quadratic photodiode placed in the condenser back-focal plane of the instrument. Change in axial position of the trapped particle causes a relative change in the amount of light impingement on

the photodetector, whereas change in lateral position causes an asymmetric interference profile on the photodiode which generates a detector signal proportional to the particle displacement. Through a conversion constant β obtained from calibration, the volt signal is converted to displacement, x. During small displacements the can probe be treated as a spring with spring stiffness, k, which makes Hooke's law valid (Eq. 2.1). The force, F, can then be determined according to:

$$F_{trap} = -kx \tag{2.1}$$

where x is the lateral displacement generated from the photodiode, as illustrated in Figure 2.10. Calibration of the stiffness is often based on thermal fluctuations of the trapped particle, which correspond to Brownian motion of an over-damped spring. The degree of stiffness depends on the laser intensity and particle properties.

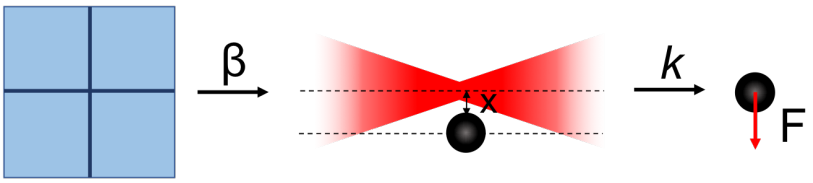

Figure 2.10: Schematic illustration of how the conversion factors is related to each other to determine the forces acting on a particle trapped by the laser in an Optical Tweezers instrument. Changes in the intensity photons detected by the photodiode is converted to displacement, x, of the particle by a sensitivity constant, β, determined from calibration. The displacement is further converted to force, by multiplying with the stiffness of the optical trap, k.

OT are widely used in both physical and biological sciences. Compared to the AFM, is the OT capable of measuring even smaller magnitudes of forces due to lower spring stiffness (0.1 - 100 pN for OT, 10 - 10^5 pN for AFM)(Neuman and Nagy 2008). Some OT's has the ability of splitting the laser into multiple beams, giving rise to the opportunity to probe multiple particles simultaneously. This makes the OT convenient to use in studies investigating ligand-receptor interactions and other biological force driven systems as motor proteins and translation (Kuo and Sheetz 1992, Moffitt *et al.* 2008).

2.3 Force measurements on the single molecular level

Many biological processes depends on specific interactions between biomolecules (Cost *et al.* 2015, Florin *et al.* 1994). These processes often involves stimulation or inhibition of different types of receptors due to binding and unbinding events. To reveal mechanistic details of molecular processes that cannot be observed during bulk experiments, one need to study the processes on a single molecular level. The force probes mentioned in the section above are perfect tools for this task.

In the following, information obtainable through the use of these force probes is explained.

2.3.1 Dynamic force spectrum

The intermolecular interactions involved in biological processes are dominated by non-covalent bonds such as $\pi - \pi$ bonds, electrostatic interactions, hydrophobic interactions and Van der Waals interactions (Evan Evans 1999, Florin *et al.* 1994, Evan Evans and Calderwood 2007). These types of bonds have limited lifetimes, meaning the bond will rupture if exposed to a pulling force for a sufficient amount of time and strength. Through manipulations of biomolecular bonds using ultra-sensitive force probes as AFM and OT, the rupture forces of the the interaction can be quantified. Dynamic force spectroscopy (DFS) is a method for further analyzing and determine the properties of the intermolecular interaction, such as lifetime and rupture forces (E. Evans and Ritchie 1997). The basis of DFS method is the DFS-plot, a scatter plot visualizing the relationship between rupture forces (pN) on the y-axis, and the logarithm of the loading rate (pN/s) (applied force per unit time (r_f, $\frac{\Delta f}{\Delta t}$)) on the x-axis. This plot creates a dynamic spectrum of bond strengths providing information about the energy landscape along the unbinding pathway.

Biomolecular bonds can be described by energy landscapes based on the kinetic energy involved in the binding (E. Evans and Ritchie 1997, Evan Evans 1999). An interaction can form several different conformational states, each having a specific amount of energy related to it. From a thermodynamic point of view, a stable state is defined as the state with least possible Gibbs free energy involved and is the state that the bond preferably will stay in. However, when external forces is applied and manipulates the bond, the bond is forced to change to states with higher degree of energy, called transition states. This is due to disrupting and forming new interaction within e.g. the binding pocket which are not favorable, until the two molecules are completely unbound. For molecules to achieve binding or conversely, they have to overcome one or several activation barriers described by the energy landscape. A specific amount of energy that has to be put into the system for the molecules to enable or break a bond (ΔG_u). When the bond is exposed to an external, mechanical force, it adds a mechanical potential that tilts the energy landscape and lowers the barriers which is graphically illustrated in Figure 2.11. During dissociation, the ligand-receptor complex follows a reaction path which can be mapped through DFS and the activation barriers can be quantified, as well as lifetime and the distance from stable state to the activation barrier.

Interaction between two molecules with equal affinity for each other, A and B, forming a complex AB can be described by the following equation:

$$\frac{d[AB]}{dt} = k_{\text{on}}[A][B] - k_{\text{off}}[AB] \tag{2.2}$$

where [A], [B] and [AB] is the concentration of the respective molecule, (k_{on}) is the association rate and (k_{off}) is the dissociation rate (Bizzarri and Cannistraro 2010). When a bond is exposed to external pulling forces, the energy landscape is altered, resulting in lower activation energy (Figure 2.11). Bell predicted that the decrease of activation free energy from a reaction of zero force is proportional by a factor to the applied force, f. Following from this and Eq. 2.2, the dissociation rate at applied force, $k_{\text{off}}(f)$, increases exponentially described by the following equation:

$$k_{\text{off}}(f) = k_{\text{off}}(0) \exp\left(\frac{f x_\beta}{k_B T}\right) \tag{2.3}$$

where k_B is the Boltzman constant, T is temperature, $k_{\text{off}}(0)$ is the dissociation rate at zero force and x_β is is the reaction coordinate corresponding to to the separation distance between the bound and the transition state and is assumed not to be affected by the force, f. Accordingly, the lifetime of the bond, τ, is also shortened due to the decrease in k_{off} by the following relationship:

$$\tau = \frac{1}{k_{\text{off}}} \tag{2.4}$$

Based on Bell's prediction, Richie and Evans developed the Bell-Evans model that describes the experimentally measured distribution, P(f), of rupture forces with time dependent force, $f(t)$, thus explaining the dependence of the unbinding force on the loading rate (E. Evans and Ritchie 1997). Assuming that: 1) loading rate, r_f, is constant during the measurement, 2) only a single pair of molecules is investigated during the process, 3) the rupture time is longer than the diffusional relaxation time, 4) rebinding process is negligible and 5) that the pulling force works is the direction of the reaction coordinate, x. The survival probability, $S(t)$, of the binding, stating the probability that the unbinding of the molecules has not yet occurred at time, t, can be derived using a first-order rate equation:

$$S(t) = \exp\left[-\int_0^t k_{\text{off}}(t')dt'\right] \tag{2.5}$$

where $k_{\text{off}}(t)$ is the time-dependent dissociation rate.

The survival probability, S(t), is related to the unbinding force probability distribution, $P(F)$, the following way: $P(F)dF = -\dot{S}(\tau)$, where τ is the lifetime of the bond. Taking Bells assumptions into account and perform the integration, the distribution can be described by the following equation

$$P(f) = \frac{k_{\text{off}}}{r_f} \exp\left[\frac{f x_\beta}{k_B T} + \frac{k_{\text{off}} k_B T}{x_\beta R}\left(1 - \exp\left(\frac{f x_\beta}{k_B T}\right)\right)\right]. \tag{2.6}$$

Finally, the most probable unbinding force, f^*, at a specific loading rate, r_f, can be found by calculating the maximum of Equation 2.6:

$$f^* = \frac{k_B T}{x_\beta} \ln\left(\frac{r_f x_\beta}{k_{\text{off}} k_B T}\right) \tag{2.7}$$

Equation 2.7 shows the linear relationship between the most probable rupture force and the logarithm of the loading rate. Hence, by obtaining these two variables experimentally, the dissociation rate at zero force, $k_{\text{off}}(0)$, and the distance from the free energy minimum to the energy barrier, x_β, can be extracted from the slope and the intercept of the fitted linear curve, respectively. These parameters are fundamental to the understanding of the kinetics and thermodynamics of the interaction of a pair of molecules and allow the comparison of kinetics between different systems and factors which may affect the affinity of two molecules.

Many biomolecular interactions usually have more than one energy barrier. According to the Bell-Evans model, these can be observed in the most probable rupture force vs. ln r_f curves having several regions with linear trends but different slopes and the graph has to be fitted to all linear regions.

Figure 2.11 shows an interpretation of the kinetics of a bond with a single energy barrier and how an externally applied force lower this barrier and increases the unbinding rate of the bond. The dissociation rate (k_{off}), the distance between the bound and transition state (x_β) and the difference in free energy of the bound and transition state is indicated in the graph.

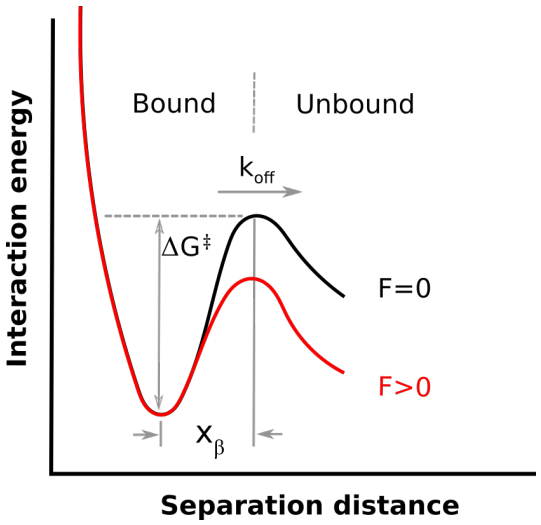

Figure 2.11: Graphic interpretation of how an external applied force, F, alters the unbinding barrier and dissociation rate, k_{off}, in the free energy landscape of a single barrier unbinding process. ΔG^u represents the activation free energy for unbinding and x_β the distance between the bound and transition state.

Chapter 3

Materials and Methods

3.1 Materials

The following list provides information about the materials used in this experiment.

- EDC (N-(3-Dimethylaminopropyl)-N-ethylcarbodiimide hydrochloride), Sigma-Aldrich, CAS Number: 25952-53-8
- Carboxyl-polystyrene beads, 3.07 μm, Spherotech
- Amino-polystyrene beads, 2.18 μm, Spherotech
- HEPES buffer (4-(2-Hydroxyethyl)piperazine-1-ethanesulfonic acid), Sigma-Aldrich, CAS Number 7365-45-9.
- Boric acid (H_3BO_3), pH 5.8, Sigma-Aldrich, CAS Number 10043-35-3.
- Calcium chloride dihydrate ($CaCl_2 \cdot 2H_2O$), Sigma-Aldrich, CAS Number: 10035-04-8
- Manganese(II) chloride tetrahydrat ($MnCl_2 \cdot 4H_2O$), Sigma-Aldrich, CAS Number: 13446-34-9
- Bovine Serum Albumin (BSA), Sigma-Aldrich, CAS number: 9048-46-8.
- Sialic acid-binding Ig-like lectin 9 (Siglec9), RD systems, Cat number: 110-HG

ASF, Gal-1 WT, Gal-7 WT and all of the Gal-3 samples were kindly provided by Prof. Hans-Joachim Gabius, Ludwig-Maximilians University, Munich. The MUC1-ST sample with attached immunoglobulin G (IgG) were kindly provided by Gianfranco Picco, King's College, London. The epimerase AlgE4 was kindly provided by Wenche Iren Strand at the institute for Biotechnology and Food science at NTNU. All proteins were provided in solid state and reported to have a high degree of purity.

3.2 Immobilization of proteins on polystyrene beads

The different galectins and glycoproteins were immobilized on the surface of polystyrene beads in order to be trapped and analyzed in the OT. To distinguish between the beads, two different diameters were used (3.07 μm for Gal-3 and 2.18 μm for glycoproteins, proteins, Gal-1 WT and Gal-7 WT). Proteins provided in solid state were diluted with HEPES buffer (25 mM HEPES, pH 7.4, 150 mM NaCl) to a final concentration of 2 mg/ml, to achieve a stock solution for further sample preparation. The glycoproteins and galectins (2.5 μL) were added to separate eppendorf tubes together with boric acid (50 μL, 50 mM) and functionalized polystyrene beads (3 μL). Gal-3 (Gal-3 WT and Gal-3 homodimer) were conjugated through a primary

amine group located on the surface of the protein to a COOH group on a COOH-functionalized polystyrene bead (diameter 3.07 μm). The glycoproteins (ASF and MUC1-ST), Gal-1 WT, Gal-7 WT, siglec9, BSA and AlgE4 were coupled through its carboxylate groups to the amine groups on NH_2-functionalized polystyrene beads (diameter 2.18 μm). To facilitate the reaction between amine and carboxylic acid groups, ethyl-N-(3-dimethyl-aminopropyl)carbodiimide (EDC) (0.4 mg) was added. The EDC were then allowed to function for 45 minutes.
To ensure no excess proteins in the final mixture, the beads were washed 5 times through sentrifugation for 6 minutes at 7500 rpm. The supernatant were then discarded and the pellet was resuspended in HEPES buffer (50 μL) between every sentrifugation. After the last sentrifugation the pellet was resuspended in 150 μL HEPES buffer. All eppendorf tubes were infused with filtered pressurized N_2 gas before use to minimize the chance of impurities in the samples.

3.3 Preparation of the liquid cell

Samples have to be injected into a liquid cell in order to be investigated with the OT instrument. The liquid cell consists of a circular BSA-treated cover glass attached to a rectangular cover glass with two strips of double sided tape, as illustrated in Figure 3.1 This creates a 2 mm wide cell were the sample is drawn in by capillary forces. The liquid cell is assembled right prior to the OT analysis. To prevent the functionalized beads from adhere to the glass slip during OT investigation, it was treated with BSA. The BSA treated circular glass were made by covering a circular coverslip (30 mm diameter, thickness 1) with filtered BSA solution (1 mg/ml, 0.2 μm filter) for 15 minutes. The excess BSA solution were then removed by a pipette before dried completely using N_2 gas. These treated cover glass were made the same day as the experiments were executed. The final sample solution were made by mixing 15 μL of each of the two washed and diluted bead suspensions into a new eppendorf tube which were further diluted with 20 μL HEPES buffer. The final solution (15 μL) was applied to one aperture of the liquid cell until completely filled up. To prevent vaporization of the sample during analysis a thin layer of regular nail polish was applied to seal the upper and bottom aperture.

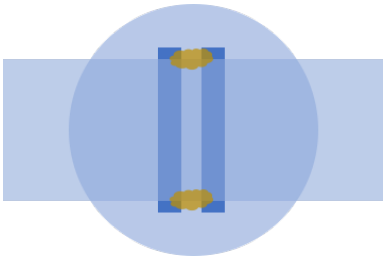

Figure 3.1: Illustration of the liquid cell used to hold a sample for investigation in Optical Tweezers. The cell consists of a circular cover glass attached to a rectangular cover glass with two strips of double sided tape(dark blue) and sealed with nail polish(brown).

3.4 The set up of the optical tweezers

The OT instrument used in this experiment is the NanoTracker with integrated Zeiss Axio Observer Inverted optical microscope delivered by JPK Instruments, schematically illustrated in Figure 3.2. It is equipped with TEM_{00} laser with 3W maximum power and option of a dual beam mode with scalable split-ratio. The laser has a Gaussian beam profile and the two traps can be controlled independently of each other. A quadrant photodiode placed at the back-focal plane of the condenser detects the displacement of the trapped beads. To minimize external vibrations, the instrument is stationed on a vibration isolation table. The software used to control and record the force data was "NanoTracker 2.0", also delivered by JPK Instruments.

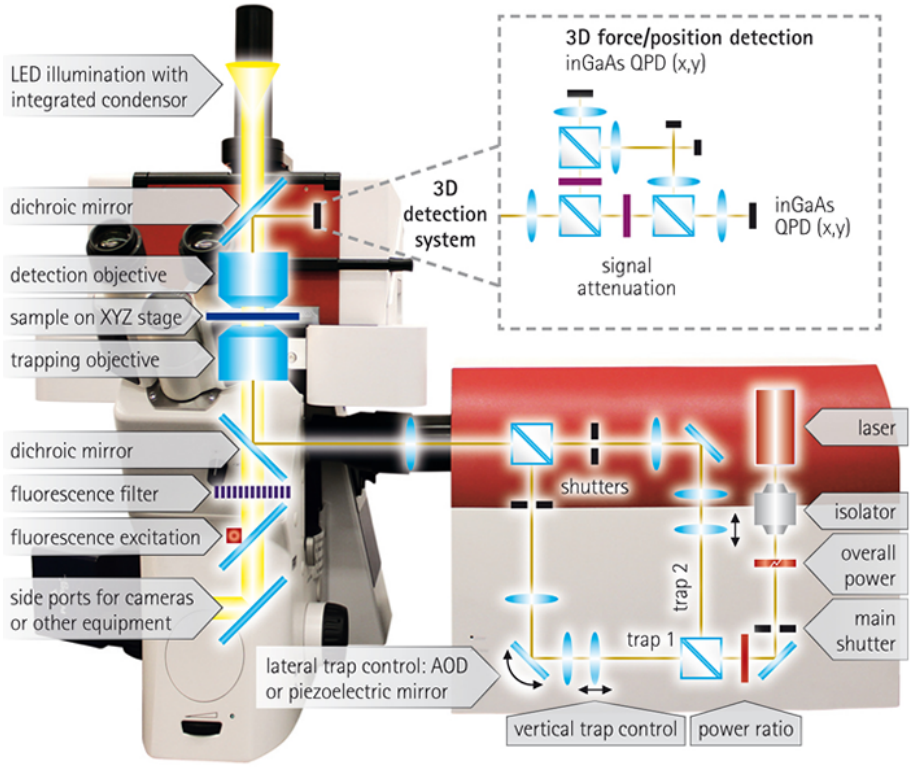

Figure 3.2: Schematic illustration of the NanoTracker Optical Tweezers instrument delivered by JPK Instruments (JPK n.d.).

3.5 Calibration of the OT

To assure that the laser was completely stable before initiating measurements, the laser system was turned on at least 1 hour prior to sample recordings. When the liquid cell was injected with the final sample solution and sealed, it was placed on the sample stage inside the OT. To achieve optimum illumination of the sample,

a Köhler illumination procedure was performed. After setting the position of the objectives for optimal focus of the beads, two beads of different size were trapped in each laser. A calibration for both bead diameter sizes (2.18 μm and 3.07 μm) was performed for all directions (x, y and z) to determine the trap stiffness and sensitivity, so that the QPD signal could be converted from volt to force. This was performed by the implemented calibration function in the NanoTracker software. The program detects the Brownian motions of the beads and calculates the spring constant based on 8 recordings and suggests a Lorentzian fitting curve, $S(f)$, to the detected bead movement. From this fitting curve, the specific sensitivity and stiffness is derived. If the fitting curve correlates badly to the recorded data, it may indicate that the bead has some defects or is attached to something in the cell which restricts its movement, hence, the constants calculated from the curve has a high degree of uncertainty. In the case of this, another bead should be used for the final recordings.

3.6 Data collection using OT

During the force measurements, one bead was kept stationary whilst the other approached and retracted it, in an oscillating movement. Before the main measurements could be recorded, a set of parameters had to be optimized: the displacement of the moving bead, speed of approach, z-position of the beads and hold-time when in contact. The displacement of the approaching and retracting bead is directly affecting the push force on the stationary bead when in contact; if too strong/large displacement, the pushing force exceeded the trap force and the stationary bead escaped the laser trap. During all experiments, this force were kept at approximately 6 - 10 pN. The speed was varied between 1.0 - 2.3 μm/sec and the hold-time between 0.2 - 1 seconds. The z-position of the moving bead was also varied related to the stationary bead until binding was achieved. Main measurements were recorded in series of about 200 oscillations, where some of the parameters were varied between each run. Total measurements depended on the binding frequency. This generated force curves showing the relationship of force (pN) as a function of bead displacement from start position (nm) for each oscillation.

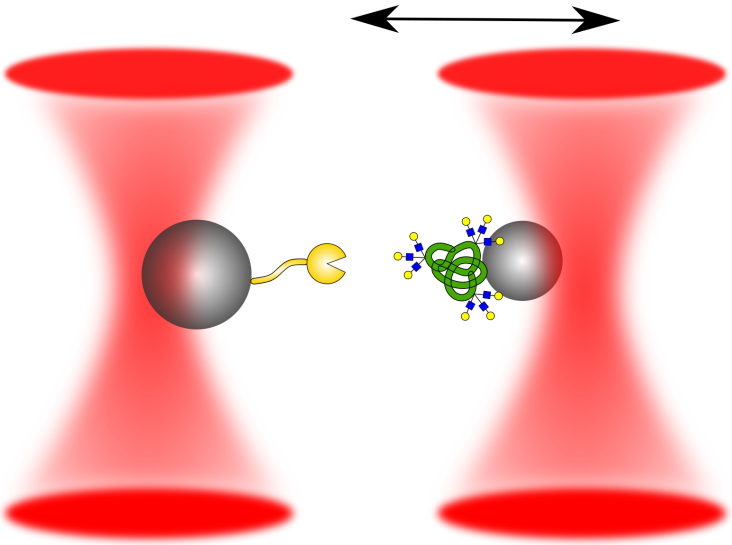

Figure 3.3: Simplified illustration of the trapping scenario in the OT where the Gal-3 is immobilized on the largest bead and the glycoprotein on the small bead. During investigations the big bead is kept stationary whilst the other is being approached and retracted by moving the trapping laser according to the arrows.

3.7 Processing of data obtained using OT

The force curves obtained from the OT analysis were further analyzed with programs written by Bjørn Torger Stokke, Professor at the Department of Physics at NTNU, run by the IDL Data Visualization Software. The four programs used in this experiment were: iNanoTrackerOT3DPreProcess.pro, iNanoTrackerOT3DPostProcess2.pro, iNanoTrackerGallery.pro and ForceSpecAnalysev8.pro. The force files generated from NanoTracker were first processed by the pre-process program to combine the retraction and approach curve from both beads and generate a single position-coordinate, using Eq. 3.1 and Eq. 3.2:

$$\Delta F = F(retract) - F(approach) \tag{3.1}$$

$$\sum F = \Delta Fx + \Delta Fy + \Delta Fz. \tag{3.2}$$

This also evened out the baseline, resulting in a straight, horizontal baseline for the combined force curves, making further analysis easier. The new combined curves were then analyzed in the post-process program where curves with interaction were separated from the curves without and the slope of the force curves with interaction could be manually fitted. The rupture force, f^*, and the loading rate, r_f, is determined from this curve. The loading rate is defined as external force applied per unit time (df/dt), and thus can be calculated from the slope as shown in Eq. 3.3:

$$r_f = \frac{\Delta y}{\Delta x} = \frac{\Delta f}{\Delta d} \tag{3.3}$$

where Δd is the change in displacement of the beads(nm). Whilst the rupture force (pN), r_f, is found from the height of the force peak relative to the baseline. Some curves may have several rupture events (peaks) due to multiple bindings being ruptured. To make galleries of the curves generated, the iNanoTrackerGallery.pro program was used. For the rest of the the graphs, SigmaPlot was used. For generation of the DFS, splitting into histograms and calculation of the energy landscape parameters, ForceSpecAnalysev8 was used.

Chapter 4

Results

Interactions between Gal-3 and the ligands were visualized by force curves generated by the OT using polystyrene beads functionalized with the respective galectin and glycoprotein. The force curves show how the forces acting on the polystyrene beads change with increasing inter-bead distance (nm) caused by the separation of the polystyrene beads in the optical traps. When the beads are in contact, intermolecular bonds can form between galectins immobilized on one bead and its ligand immobilized on the other bead. In the case of interaction, force jumps can be observed in the recorded force - distance curves.

Based on the force curves generated from the OT a DFS was produced for each system. The DFS plots show the distribution of the rupture forces with increasing force loading rate. Based on the determined force loading rates, the continuous distribution of rupture events was divided into subgroups, and for each subgroup a histogram showing the distribution of the rupture forces within that loading rate interval, was generated. The probability density fit, P(f) (Eq. 2.6), is also determined and plotted together with the histograms.

The following chapter presents the results obtained from investigating interaction between two structural forms of Gal-3: wild type and homodimer, and two glycoproteins: ASF and MUC1(ST). In addition, the hybrid forming abilities of Gal-3 using Gal-1 and Gal-7 as ligands were also investigated. All the molecular pair interactions are investigated using OT. In chapter 4.1 the interaction frequencies of Gal-3 and different ligands presented, characterizing the interaction abilities of Gal-3. Chapter 4.2 presents galleries of typical and system specific force curves, as well as the DFS for each of the different Gal-3 - glycoprotein systems. A summary of the parameters characterizing the interactions determined from the DFS analysis is presented at the end of that section. Finally, chapter 4.3 presents galleries, DFS and characterizing parameters for the Gal-3 - Gal-1, as well as Gal-3 - Gal-7 molecular pairs.

4.1 Gal-3 interaction abilities

Lectins can potentially give rise to unspecific interactions (Celik and Moy 2012), to confirm the validity of the recorded data knowing this, Gal-3 WT were allowed to interact with a set of chosen proteins and naked NH_2-functionalized beads. For negative controls the lectin Siglec-9, the epimerase AlgE4, bovine serum albumin and naked NH_2-functionalized beads were used. The interaction frequency of the systems further studied in this master thesis were calculated based on the ratio of the number of force curves for which the slope and thus the force loading rate could be reliably calculated and included in the DFS analysis only, divided by the total number of retractions obtained. Thus, it is reasonable to believe that they are underestimated. Whilst the interaction frequency for the negative control experiments were based on all observable interactions. Figure 4.1 presents the interaction frequencies between Gal-3 WT and different ligands: Siglec-9, AlgE4, BSA, naked NH_2-functionalized beads, ASF, MUC1(ST), Gal-7 WT and Gal-1 WT. Interaction frequencies for the Gal-3 - glycoprotein systems are presented in

Figure 4.2. Number of bead pairs investigated, number of force curves recorded, interaction frequency (P_{int}) with associated standard deviation (SD) are listed for all of the systems in Table 4.1, data for the negative controls is presented in Appendix A. In addition to investigating several bead pairs, were 3 - 4 different z-positions of the small bead used during investigation for each bead pair examined. For the Gal-3 WT and naked NH_2-functionalized beads, 3 out of 4 bead pairs got stuck together due to very strong interactions, making the lasers unable to tear them apart. In the case of the Gal-3 WT - AlgE4 system, 5 out of 6 bead pairs did not interact. The interactions observed for the 6th pair were thus believed not to be related to a specific protein-interaction and were not included in the calculation of interaction frequency.

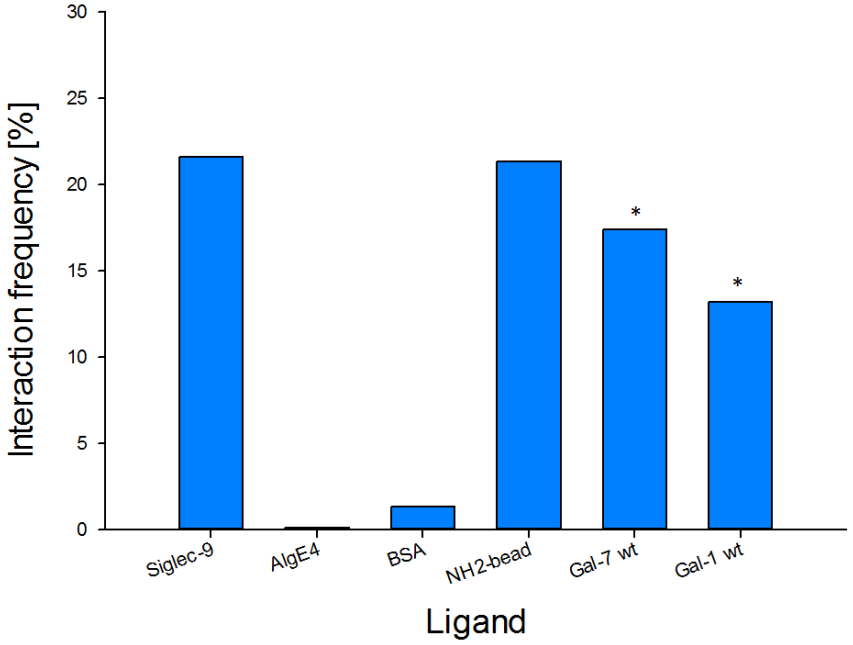

Figure 4.1: Interaction frequencies (%) between Gal-3 WT and the different ligands: sialic acid-binding Ig-like lectin 9 (Siglec-9), epimerase AlgE4, bovine albumin serum (BSA), naked NH_2-functionalized beads, galectin-7 WT (Gal-7 wt) and galectin-1 WT (Gal-1 wt). The frequencies are found based on data obtained by OT by immobilizing Gal-3 WT on COOH-functionalized beads and the respective ligands on NH_2-functionalized beads. Interaction frequencies for the systems marked with a star (*) are calculated based only on force curves which the slope and thus, the force loading rate could be reliably calculated and included in the DFS. Data is listed in Appendix A.

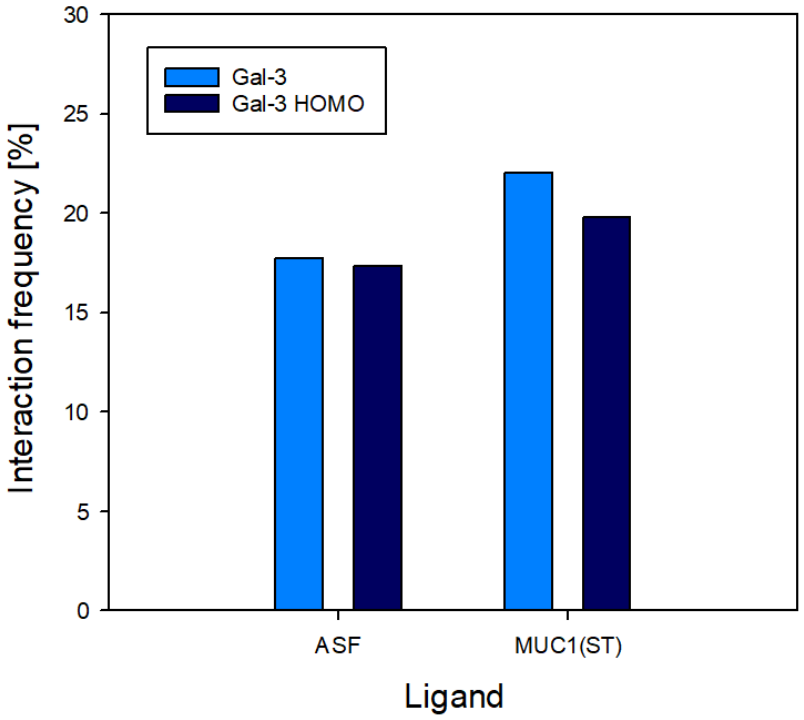

Figure 4.2: Interaction frequencies (%) between Gal-3 WT and Gal-3 homodimer and the different glycoproteins: ASF and MUC1(ST). The frequencies are calculated based on force curves with interaction of which the slope and thus, the force loading rate could be reliably calculated and included in the DFS. The data was obtained by OT approach by immobilizing the galectin and glycoprotein on COOH-functionalized and NH_2-functionalized beads, respectively.

Table 4.1: Interaction frequency data for negative controls and the systems investigated in this thesis. The associated standard deviation (SD) i also included in the table.

Galectin	Ligand	No. of bead pairs	No. force curves	P_{int} [%]	SD
Gal-3 WT	Siglec9	3	470	22	20
	AlgE4	6	570	7	16
	BSA	5	750	1.3	0.5
	NH_2 beads[a]	4	400	17[a]	18
	Gal-7 WT	11	5490	17.4[b]	-
	Gal-1 WT	8	4579	13.2[b]	-
	ASF	12	2897	17.7[b]	-
	MUC1(ST)	6	3637	22.0[b]	-
Gal-3 HOMO	ASF	10	4632	17.3 [b]	-
	MUC1(ST)	9	4123	19.8[b]	-

[a] 3 out of 4 bead pairs of the system got stuck together due to very strong interactions, making the lasers unable to tear them apart.
[b] The frequencies are calculated based on force curves with interaction of which the slope and thus, the force loading rate could be reliably calculated and included in the DFS, thus, the values are underestimated.

4.2 Experimental data for Gal-3 - glycoprotein interactions

In the first part of the study were the substrate binding abilities of Gal-3 investigated using two different structural forms of Gal-3: wild type and homodimer, with the two glycoproteins: ASF and MUC1(ST) as substrates. By analyzing the data obtained from the OT retraction experiments, galleries of force curves and DFS were generated. Below galleries of typical and characteristic force curves and the DFS are presented for each of the four systems investigated: Gal-3 - ASF, Gal-3 homodimer - ASF, Gal-3 WT - MUC1(ST) and Gal-3 homodimer - MUC1(ST). Parameters describing the interactions are presented in the end of the section, and comparison plots.

4.2.1 Gal-3 WT - ASF

Galleries

A selection of the most frequently observed types of force curves are presented in Figure 4.3, where Figure 4.3b shows examples of curves showing a more steep exponential rise in force. The system was found to have a low tendency of forming multiple interaction. However, a selection of some of the ones that were observed are presented in Figure 4.4. Figure 4.4a presents double rupture events occurring within a short interval of inter-bead separation distance, compared with the ones in Figure 4.4b.

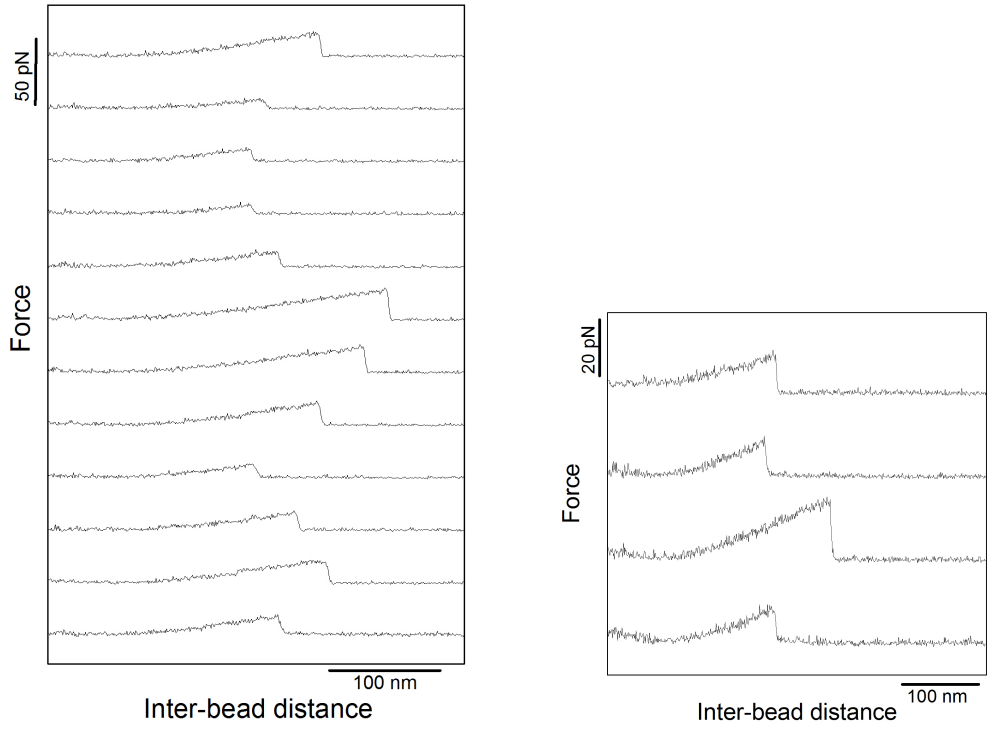

(a) Normal force curves **(b)** Exponential rise in force

Figure 4.3: Examples of the most frequent type of force vs. inter-bead distance curves obtained for the Gal-3 WT - ASF system (a). The curves were generated using OT with polystyrene beads functionalized with Gal-3 and ASF, respectively. (b) More detailed representation of force curves with an exponential rise in force prior to bond rupture.

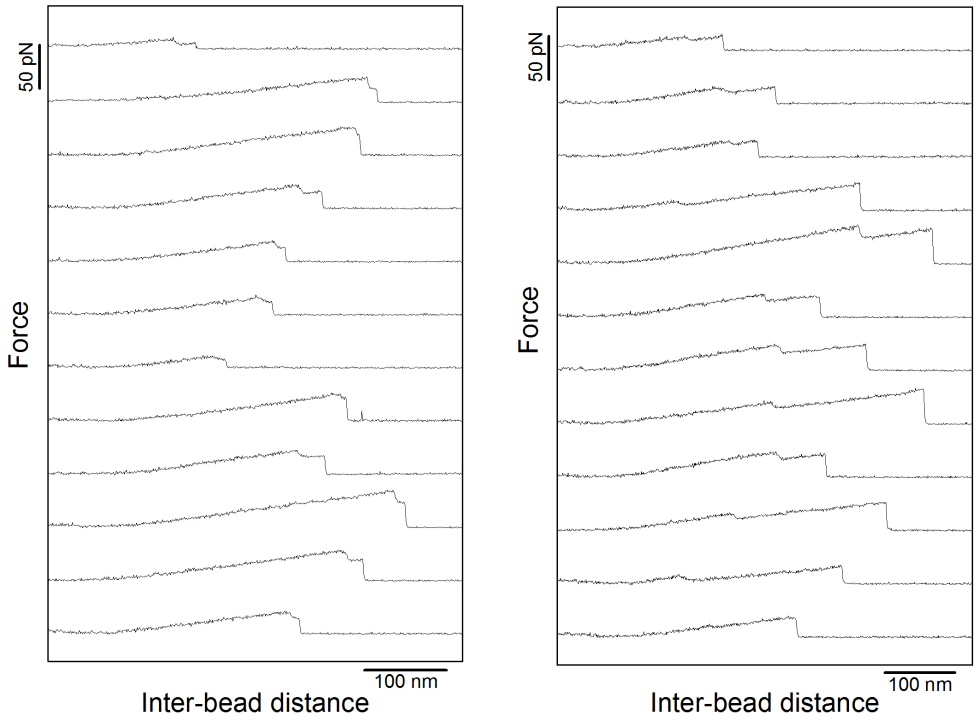

(a) Short rupture intervals **(b)** Long rupture intervals

Figure 4.4: Examples of force vs. inter-bead distance curves with double rupture events obtained for the Gal-3 WT - ASF system. (a) Rupture events occurring within a short interval of increasing inter-bead distance. (b) Curves showing multiple rupture events occurring within a wide interval of inter-bead separation distance. The curves were obtained using OT set up with polystyrene beads functionalized with Gal-3 and ASF, respectively.

Dynamic force spectrum

Figure 4.5 presents the DFS generated from 407 recorded force curves from the interactions between Gal-3 WT and ASF. Histograms of the distribution of the rupture forces with a corresponding fitted line, P(f), for each subgroup are presented in Figure 4.6. The colours of the histograms correspond with the colour in the DFS-plot. The most likely rupture force, f*, determined from the fitted line, and the average loading rate of the subgroup, r_f, is included in each histogram.

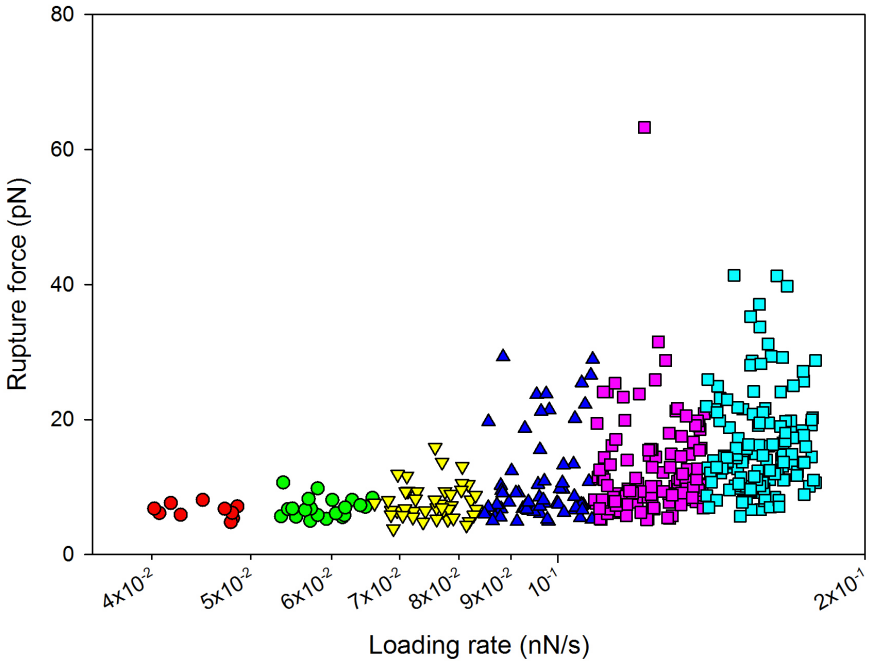

Figure 4.5: Dynamic force spectrum obtained from the interactions between Gal-3 WT and ASF showing the distribution of the rupture force (y-axis) with increasing loading rate (logarithmic x-axis). Subgroups for further histogram analysis is indicated with different colours. The plot is generated based on information contained in force curves obtained with OT with polystyrene beads functionalized with Gal-3 WT and ASF, respectively.

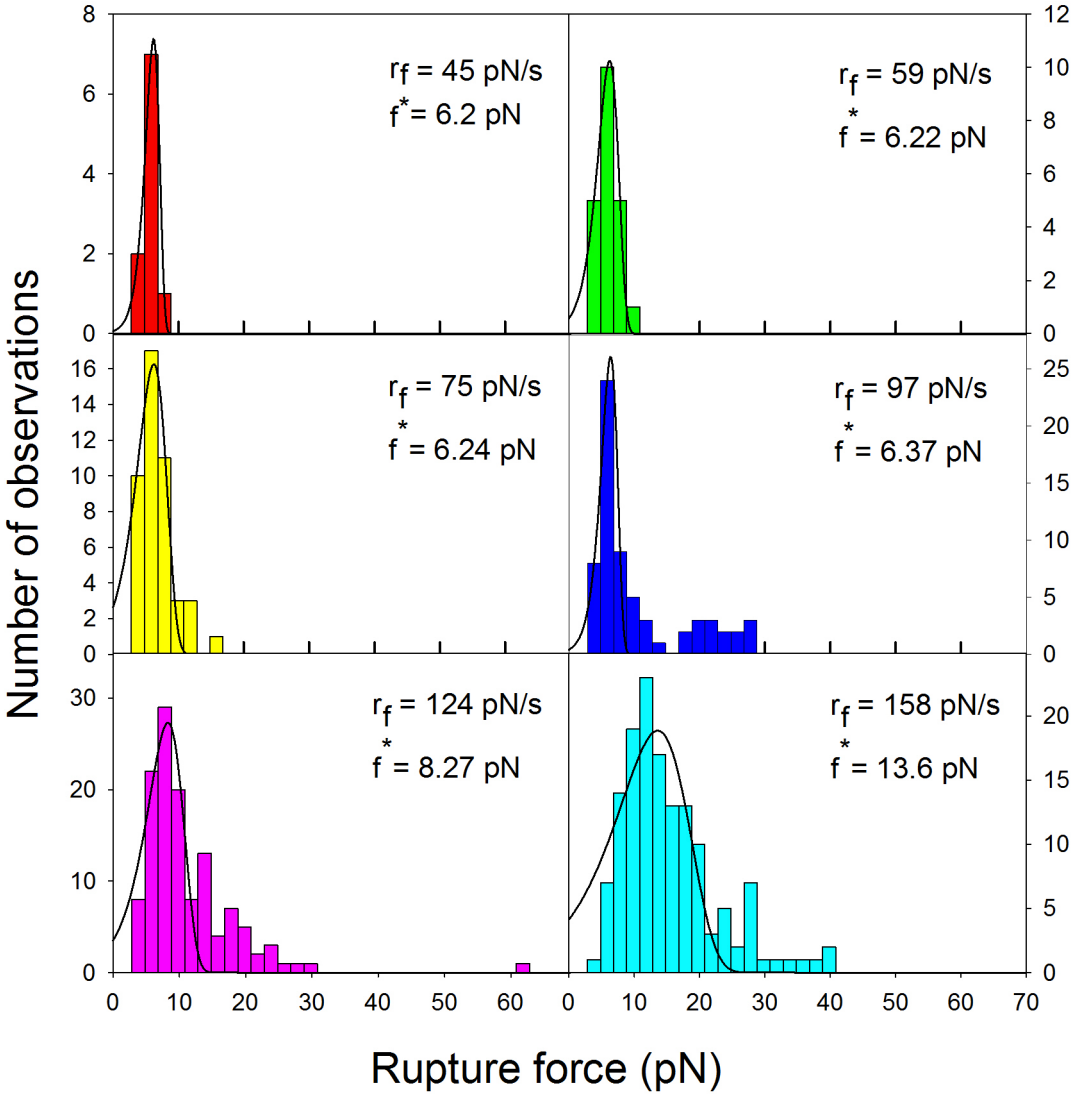

Figure 4.6: Histograms revealing the distribution of experimentally determined inter-molecular rupture forces between Gal-3 WT and ASF within an interval of loading rates predefined from the continuous distribution of bond rupture observations plotted in a rupture force vs. log loading rate plot (DFS-plot). The most likely rupture force, f*, and the average loading rate, r_f, for the subgroup is included in each histogram. The continuous line shows the fit of P(f) (Eq. 2.6) to the histograms. The rupture observations were obtained from OT using polystyrene beads functionalized with Gal-3 WT and ASF, respectively. The colour of each histogram correspond to the defined loading rate intervals in the DFS-plot in Figure 4.5.

4.2.2 Gal-3 homodimer - ASF

Galleries

Examples of typical force curves for the system is presented in Figure 4.7. This

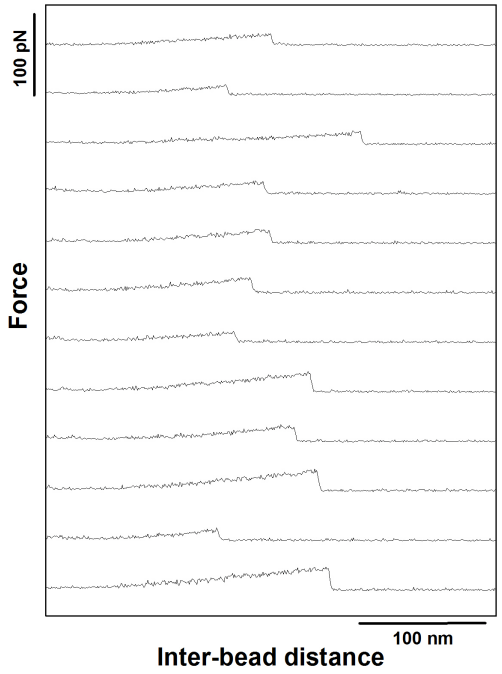

Figure 4.7: Examples of the most frequent type of force vs. inter-bead distance curves obtained for the Gal-3 homodimer - ASF system. The curves were generated using OT with polystyrene beads functionalized with Gal-3 homodimer and ASF, respectively.

system also showed a tendency for multiple rupture events occurring in a single retraction of the beads. Evidence for this is presented in Figure 4.8b. The frequency of these double rupture events was also higher than for the Gal3 WT - ASF system. Some curves with significantly higher rupture forces (50 - 100 pN) were also observed, as shown in Figure 4.8a. However, these events were relatively rare.

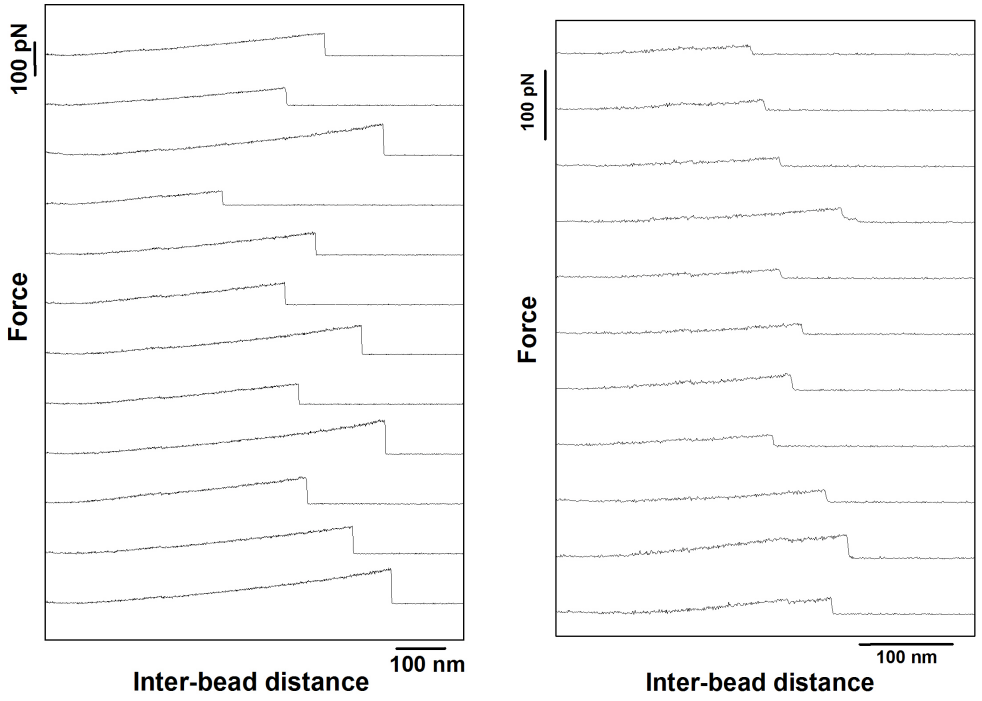

(a) Strong rupture force curves **(b)** Double rupture events curves

Figure 4.8: Examples of characteristic force vs. inter-bead distance curves obtained for the Gal-3 homodimer - ASF system. (a) Examples of curves with strong rupture forces. (b) Examples of double rupture events. The curves were obtained using OT with polystyrene beads functionalized with Gal-3 homodimer and ASF, respectively.

Dynamic force spectrum

In Figure 4.9 is the DFS presented for the Gal-3 homodimer - ASF system, determined from 584 recorded force curves. Histograms of the distribution of the rupture forces with a corresponding fitted line, P(f), for each subgroup are presented in Figure 4.10. The colours of the histograms corresponds with the colour in the DFS-plot. The most likely rupture force, f*, determined from the fitting line, and the average loading rate of the subgroup, r_f, is included in each histogram.

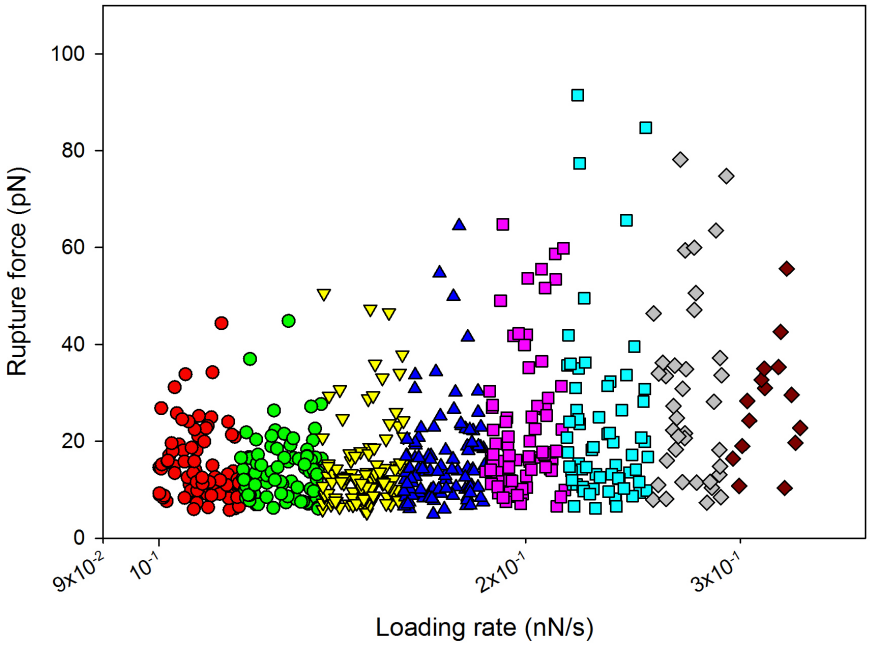

Figure 4.9: Dynamic force spectrum obtained from the interactions between Gal-3 homodimer and ASF showing the distribution of the rupture force (y-axis) with increasing loading rate (logarithmic x-axis). Subgroups for further histogram analysis is indicated with different colours. The plot is generated based on information contained in force curves obtained with OT with polystyrene beads functionalized with Gal-3 homodimer and ASF, respectively.

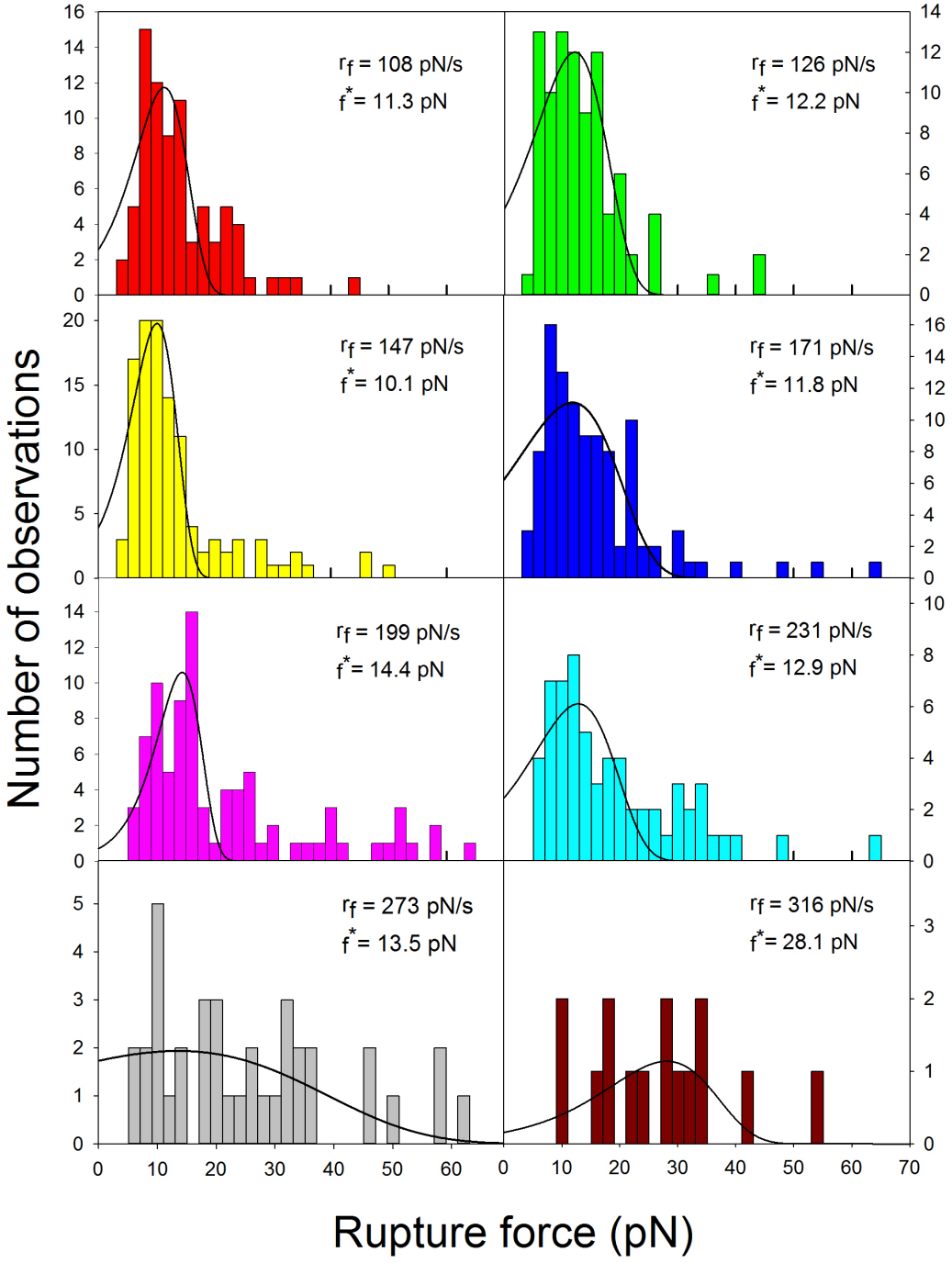

Figure 4.10: Histograms revealing the distribution of experimentally determined inter-molecular rupture forces between Gal-3 homodimer and ASF within an interval of loading rates predefined from the continuous distribution of bond rupture observations plotted in a rupture force vs. log loading rate plot (DFS-plot). The most likely rupture force, f*, and the average loading rate, r_f, for the subgroup is included in each histogram. The continuous line shows the fit of P(f) (Eq. 2.6) to the histograms. The rupture observations were obtained from OT using polystyrene beads functionalized with Gal-3 homodimer and ASF, respectively. The colour of each histogram correspond to the defined loading rate intervals in the DFS-plot in Figure 4.9.

4.2.3 Gal-3 WT - MUC1(ST)

Galleries

Examples of typical force curves for the Gal-3 WT - MUC1(ST) system are presented in Figure 4.11a. Curves obtained for this system showed a higher frequency of both strong rupture forces (Figure 4.11b) and multiple rupture events during separation (Figure 4.12), than for the other two previous systems.

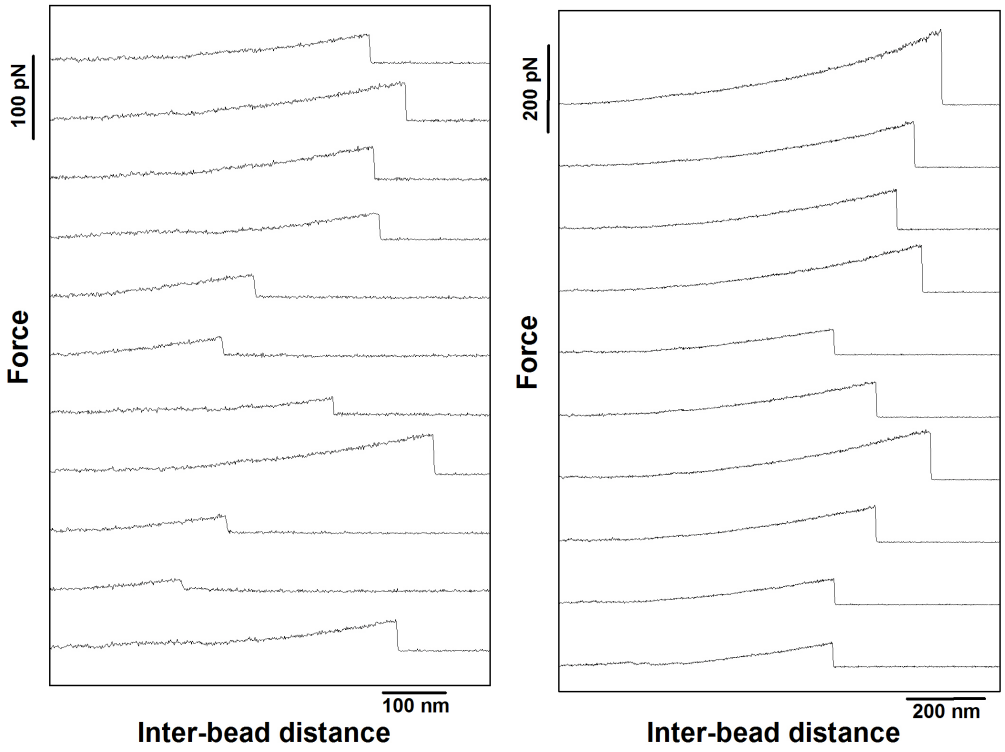

(a) Normal force curves **(b)** Strong rupture force curves

Figure 4.11: Examples of force vs. inter-bead distance curves obtained for the Gal-3 WT - MUC1(ST) system. (a) Selection of the most frequent observed type of curves. (b) Examples of curves with relatively high rupture forces. The curves were generated using OT with polystyrene beads functionalized with Gal-3 WT and MUC1(ST), respectively.

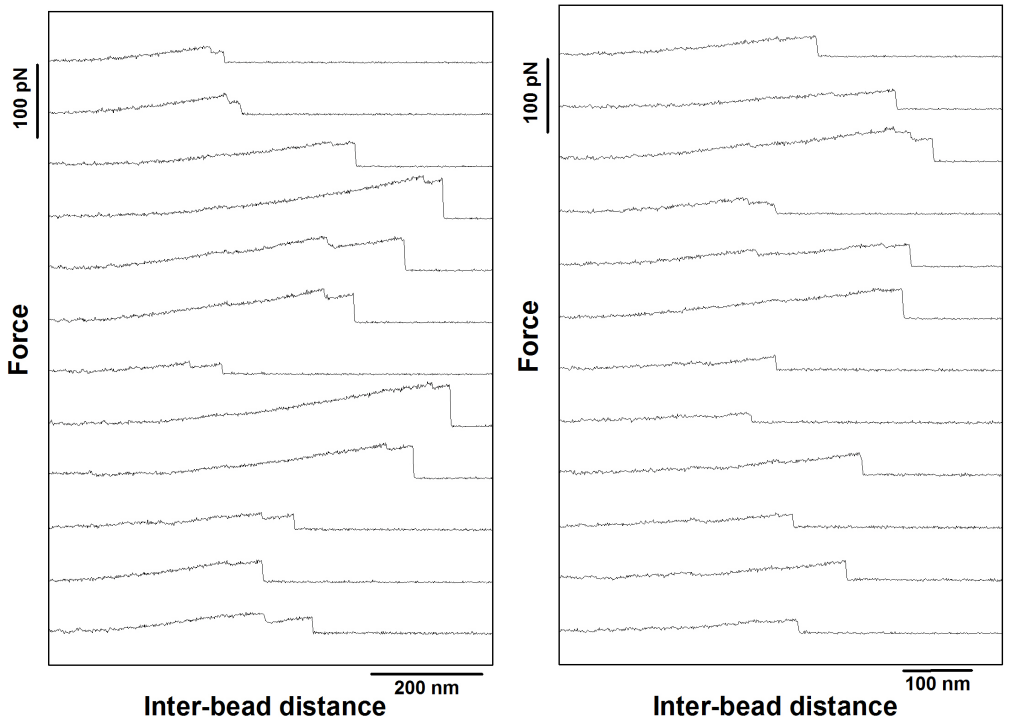

(a) Double rupture peaks **(b)** Multiple rupture peaks

Figure 4.12: Examples of force vs. inter-bead distance curves with successive rupture events obtained for the Gal-3 WT - MUC1(ST) system. (a) Selection of force versus distance curves showing double rupture events. (b) Examples of curves with multiple rupture events. The curves were generated using OT with polystyrene beads functionalized with Gal-3 WT and MUC1(ST), respectively.

Dynamic force spectrum

In Figure 4.13 the DFS is presented for the Gal-3 WT - MUC1(ST) system, determined from 587 recorded force curves. Histograms of the distribution of the rupture forces with a corresponding fitted line, P(f), for each subgroup are presented in Figure 4.14. The colours of the histograms corresponds with the colour in the DFS-plot. The most likely rupture force, f*, determined from the fitting line, and the average loading rate of the subgroup, r_f, is included in each histogram.

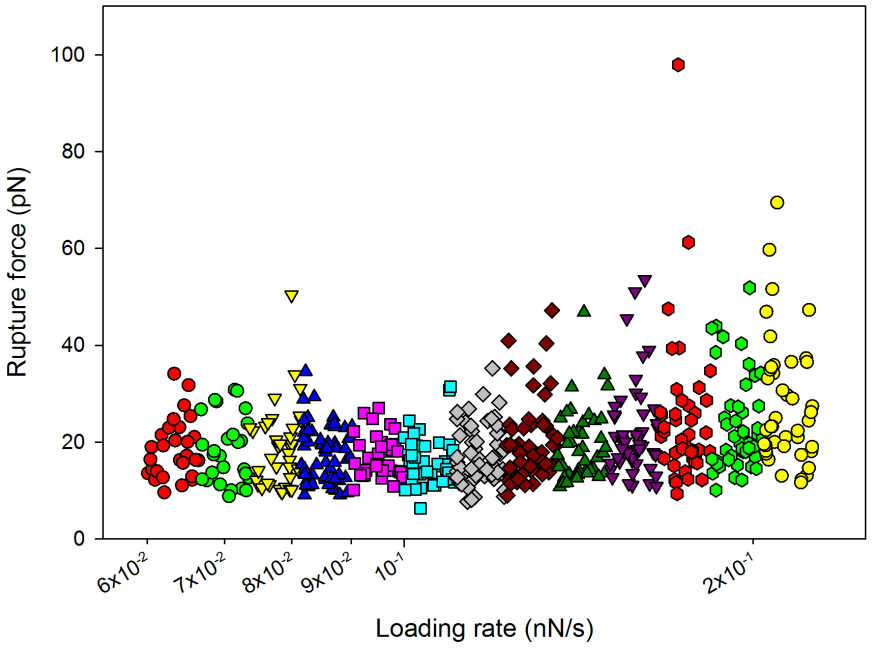

Figure 4.13: Dynamic force spectrum obtained from the interactions between Gal-3 WT and MUC1(ST) showing the distribution of the rupture force (y-axis) with increasing loading rate (logarithmic x-axis). Subgroups for further histogram analysis is indicated with different colours. The plot is generated based on information contained in force curves obtained with OT with polystyrene beads functionalized with Gal-3 WT and MUC1(ST), respectively.

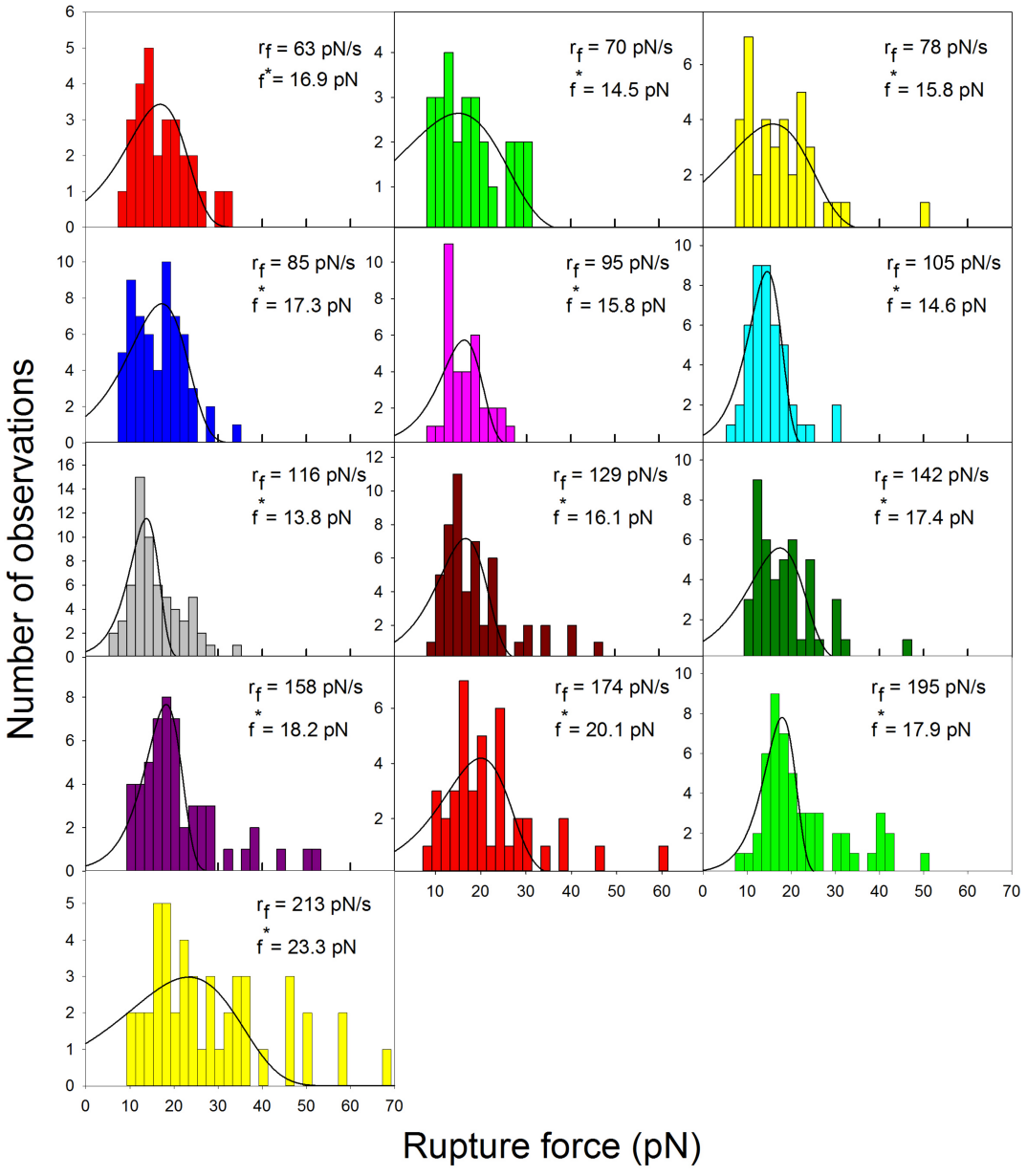

Figure 4.14: Histograms revealing the distribution of experimentally determined inter-molecular rupture forces between Gal-3 WT and MUC1(ST) within an interval of loading rates predefined from the continuous distribution of bond rupture observations plotted in a rupture force vs. log loading rate plot (DFS-plot). The most likely rupture force, f*, and the average loading rate, r_f, for the subgroup is included in each histogram. The continuous line shows the fit of P(f) (Eq. 2.6) to the histograms. The rupture observations were obtained from OT using polystyrene beads functionalized with Gal-3 WT and MUC1(ST), respectively. The colour of each histogram correspond to the defined loading rate intervals in the DFS-plot in Figure 4.13.

4.2.4 Gal-3 homodimer - MUC1(ST)

Galleries

Galleries of the Gal-3 homodimer - MUC1(ST) system i presented in Figure 4.15. 4.15a shows a selection of typical appearing curves, whereas 4.15b shows a selection of some force curves with double peaks occurring with varying inter-bead distance, slope and force difference. Curves obtained for this system showed a higher frequency of multiple rupture events during separation, than for the other three previous systems.

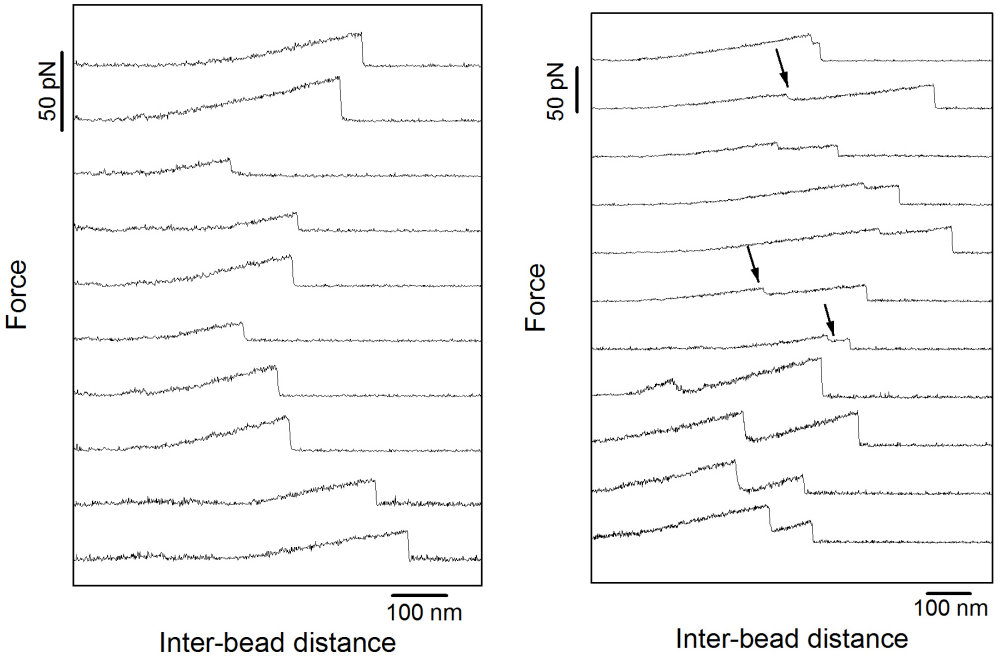

(a) Normal curves **(b)** Double force jump curves

Figure 4.15: Examples of force vs. inter-bead distance curves with successive rupture events obtained for the Gal-3 WT - MUC1(ST) system. (a) Selection of normal force versus distance curves. (b) Examples of curves with multiple rupture events. The curves were generated using OT with polystyrene beads functionalized with Gal-3 WT and MUC1(ST), respectively. Arrows indicate weak force jumps.

Dynamic force spectrum

In Figure 4.16 is the DFS plot presented for the Gal-3 homodimer - MUC1(ST) system, determined from 758 recorded force curves. Histograms of the distribution of the rupture forces with a corresponding fitted line, P(f), for each subgroup are presented in Figure 4.17. The colours of the histograms corresponds with the

colour in the DFS-plot. The most likely rupture force, f*, determined from the fitting line, and the average loading rate of the subgroup, r_f, is included in each histogram.

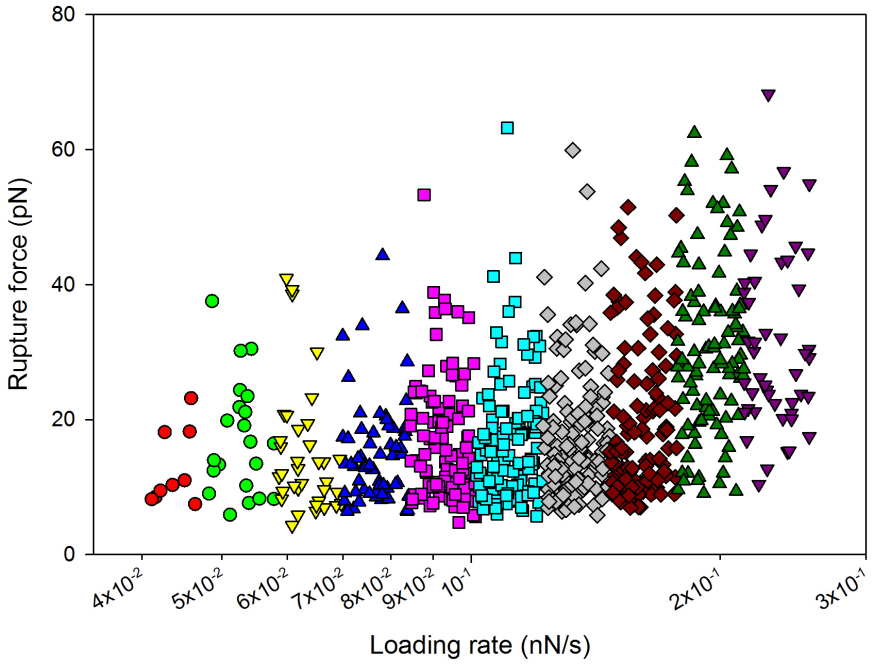

Figure 4.16: Dynamic force spectrum obtained from the interactions between Gal-3 homodimer and MUC1(ST) showing the distribution of the rupture force (y-axis) with increasing loading rate (logarithmic x-axis). Subgroups for further histogram analysis is indicated with different colours. The plot is generated based on information contained in force curves obtained with OT with polystyrene beads functionalized with Gal-3 homodimer and MUC1(ST), respectively.

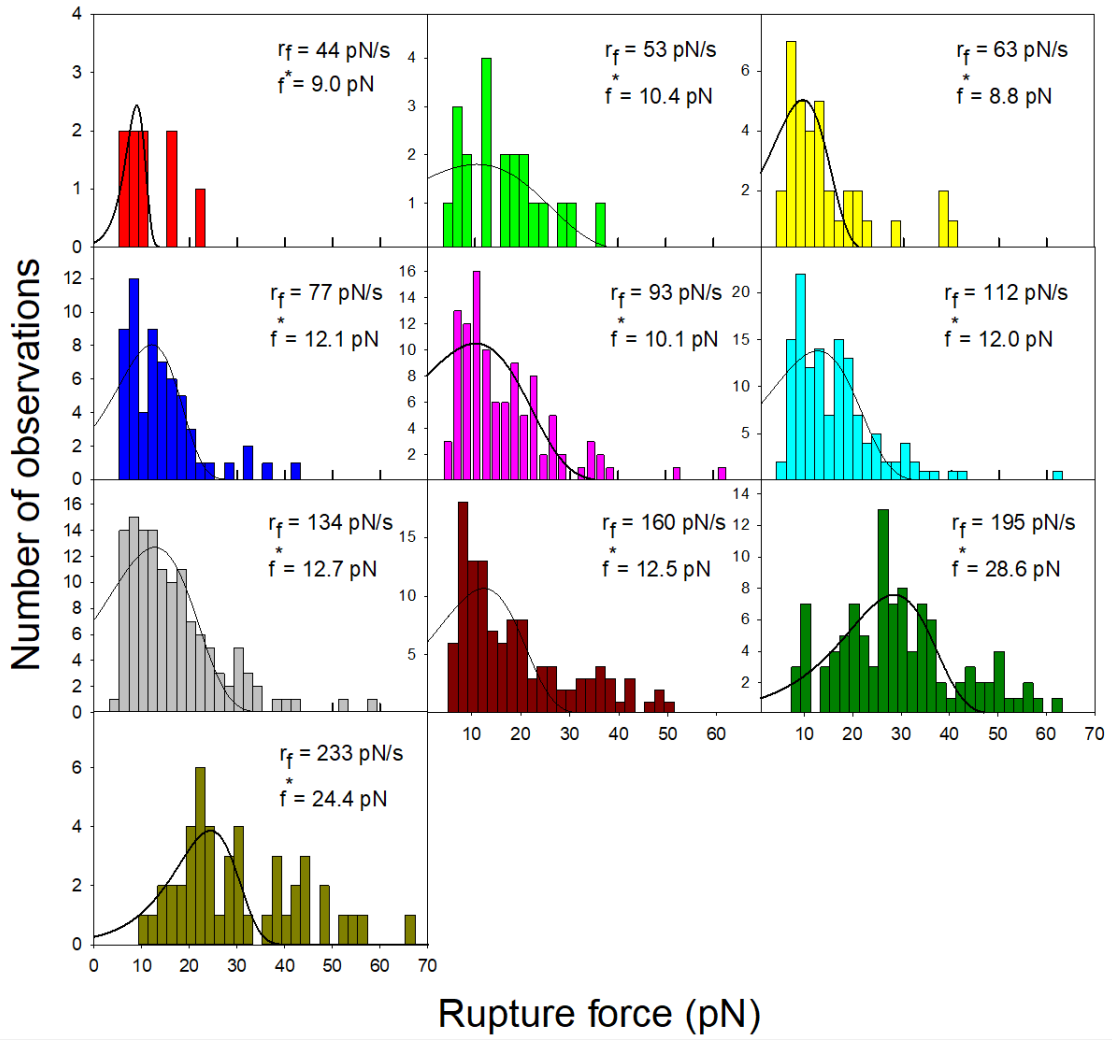

Figure 4.17: Histograms revealing the distribution of experimentally determined inter-molecular rupture forces between Gal-3 homodimer and MUC1(ST) within an interval of loading rates predefined from the continuous distribution of bond rupture observations plotted in a rupture force vs. log loading rate plot (DFS-plot). The most likely rupture force, f*, and the average loading rate, r_f, for the subgroup is included in each histogram. The continuous line shows the fit of P(f) (Eq. 2.6) to the histograms. The rupture observations were obtained from OT using polystyrene beads functionalized with Gal-3 homodimer and MUC1(ST), respectively. The colour of each histogram correspond to the defined loading rate intervals in the DFS-plot in Figure 4.16.

4.2.5 Parameters characterizing Gal-3 - glycoprotein interactions

Based on the probability density function P(f) (Eq. 2.6) fitted to the histograms presented for each system above (section 4.2.1 - 4.2.4), a set of coefficients describing the energy landscape of the interactions could be extracted using iNanoTracker, as described in section 2.3.1. Table 4.2, 4.3, 4.4 and 4.5 summarizes the number of observations in each subgroup, most likely rupture force, f*, the average loading rate, r_f and estimates of the coefficients dissociation rate, $k_{off,0}$, and the distance between the bound and transition state, x_β, for the systems Gal-3 WT- ASF, Gal-3 homodimer - ASF, Gal-3 WT - MUC1(ST) and Gal-3 homodimer - MUC1(ST), respectively. The averaged distance between bound and transition state, $\overline{x_\beta}$, dissociation rate, $\overline{k_{off,0}}$, and lifetime, τ, together with associated error calculated by standard deviation is presented in Table 4.6. For a clearer representation of the trend and comparison of the DFS-plots, the most likely rupture forces for every interval are plotted against loading rate for all the four systems in Figure 4.18a. A combined representation of the dissociation rate, $k_{off,0}$ and distance between bound and transition state (x_β) for all four systems are presented in Figure 4.18b and 4.18c, respectively. The variation in the most probable rupture force, f*, for each subgroup is visualized by box plots in Appendix B for every system.

Table 4.2: Parameters characterizing the energy landscape of the interaction between Gal-3 WT and ASF: most likely rupture force (f*), the average loading rate (r_f), dissociation rate ($k_{off,0}$), and distance between the bound and transition state (x_β).

Interval	No. of observations	r_f [pN/s]	f* [pN]	$k_{off,0}$ [1/s]	x_β [nm]
0	10	45	6.2	0.14	3.7
1	21	59	6.2	0.8	2.5
2	45	75	6.2	2.1	1.8
3	65	97	6.4	0.5	3.3
4	125	124	8.3	2.2	1.5
5	141	158	13.6	2.5	0.72

Table 4.3: Parameters characterizing the energy landscape of the interaction between Gal-3 homodimer and ASF: most likely rupture force (f*), the average loading rate (r_f), dissociation rate ($k_{off,0}$), and distance between the bound and transition state (x_β).

Interval	No. of observations	r_f [pN/s]	f* [pN]	$k_{off,0}$ [1/s]	x_β [nm]
0	79	108	11.3	2.1	0.87
1	89	126	12.2	2.9	0.63
2	110	147	10.1	2.9	1.02
3	102	171	11.8	5.1	0.45
4	84	199	14.4	1.3	1.04
5	66	231	12.9	5.5	0.55
6	39	273	13.5	6.3	0.15
7	15	316	28.1	1.8	0.42

Table 4.4: Parameters characterizing the energy landscape of the interaction between Gal-3 WT and MUC1(ST): most likely rupture force (f*), the average loading rate (r_f), dissociation rate ($k_{off,0}$), and distance between the bound and transition state (x_β).

Interval	No. of observations	r_f [pN/s]	f* [pN]	$k_{off,0}$ [1/s]	x_β [nm]
0	28	63	16.9	0.8	0.58
1	27	70	14.5	1.8	0.34
2	38	78	15.8	1.6	0.41
3	60	85	17.3	0.97	0.60
4	34	95	15.8	0.68	0.87
5	44	105	14.6	0.58	1.1
6	63	116	13.8	0.54	1.2
7	54	129	16.1	1.3	0.73
8	45	142	17.4	1.4	0.64
9	53	158	18.2	0.45	0.99
10	42	174	20.1	1.6	0.54
11	52	195	17.9	0.35	1.1
12	47	213	23.3	2.8	0.31

Table 4.5: Parameters characterizing the energy landscape of the interaction between Gal-3 homodimer and MUC1(ST): most likely rupture force (f*), the average loading rate (r_f), dissociation rate ($k_{off,0}$), and distance between the bound and transition state (x_β).

Interval	No. of observations	r_f [pN/s]	f* [pN]	$k_{off,0}$ [1/s]	x_β [nm]
0	9	44	8.95	0.3	2.0
1	21	53	10.4	1.7	0.25
2	35	63	8.82	2.5	0.65
3	62	77	12.1	1.9	0.59
4	105	93	10.1	3.3	0.33
5	131	112	12.0	3.4	0.42
6	128	134	12.7	3.7	0.42
7	115	160	12.5	4.4	0.45
8	104	195	28.6	1.0	0.44
9	48	233	24.4	0.9	0.61

Table 4.6: Summary of the average parameter values: distance from bound to transition state ($\overline{x_\beta}$), dissociation rate ($\overline{k_{off,0}}$) and lifetime ($\overline{\tau}$) for all galectin - glycoprotein systems with associated standard deviation. τ was calculated using equation 2.4.

System	$\overline{x_\beta}$ [nm]	$\overline{k_{off,0}}$ [s^{-1}]	$\overline{\tau}$ [s]
Gal-3 WT - ASF	2.3±1.1	1.4±1.0	1.0±0.8
Gal-3 HOMO - ASF	0.6±0.3	3.5±2.0	0.4±0.2
Gal-3 WT - MUC1(ST)	0.7±0.3	1.1±0.7	1.2±0.8
Gal-3 HOMO - MUC1(ST)	0.5±0.1	2.5±1.3	0.5±0.3

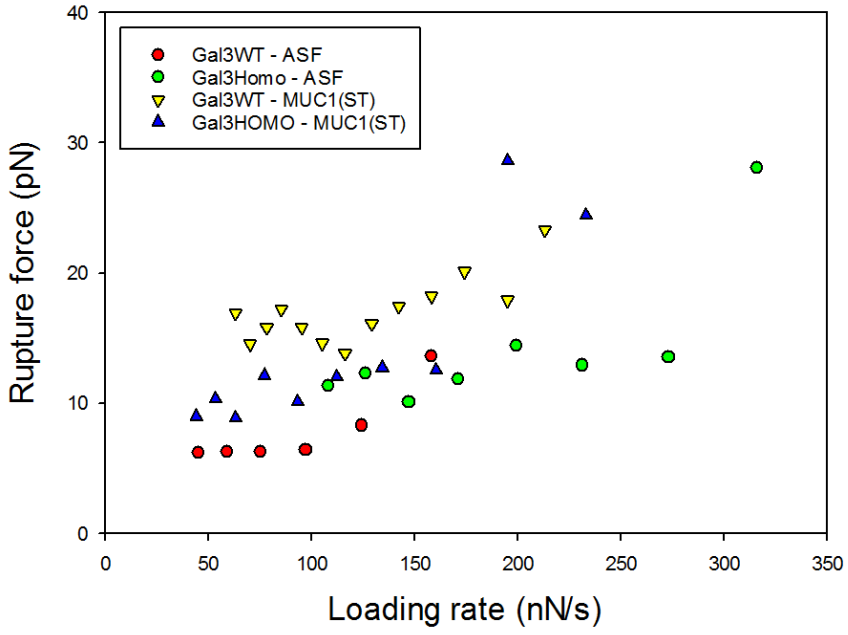
Gal3WT - ASF
Gal3Homo - ASF
Gal3WT - MUC1(ST)
Gal3HOMO - MUC1(ST)
Rupture force (pN)
Loading rate (nN/s)
0
10
20
30
40
0
50
100
150
200
250
300
350

(a) DFS

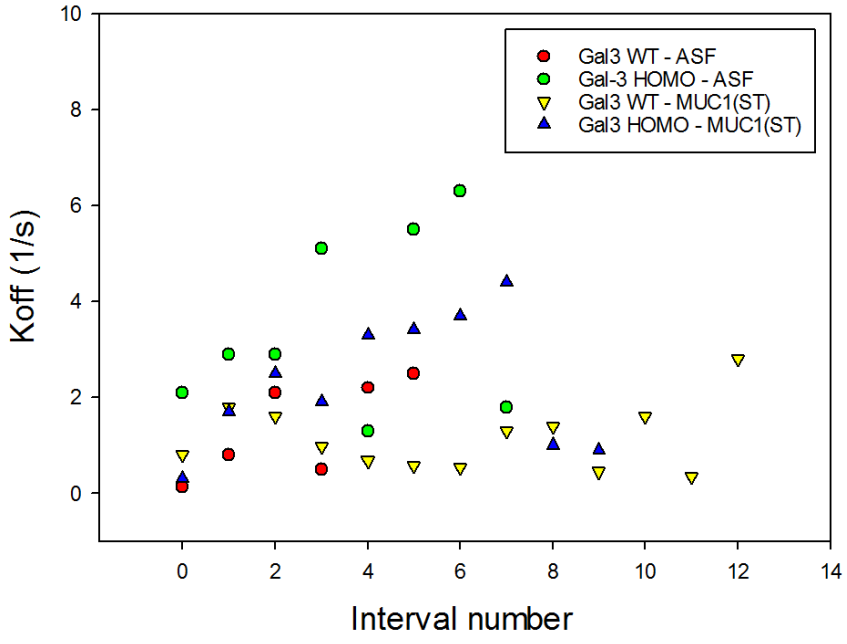
Gal3 WT - ASF
Gal-3 HOMO - ASF
Gal3 WT - MUC1(ST)
Gal3 HOMO - MUC1(ST)
Koff (1/s)
Interval number
0
2
4
6
8
10
0
2
4
6
8
10
12
14

(b) $k_{off,0}$

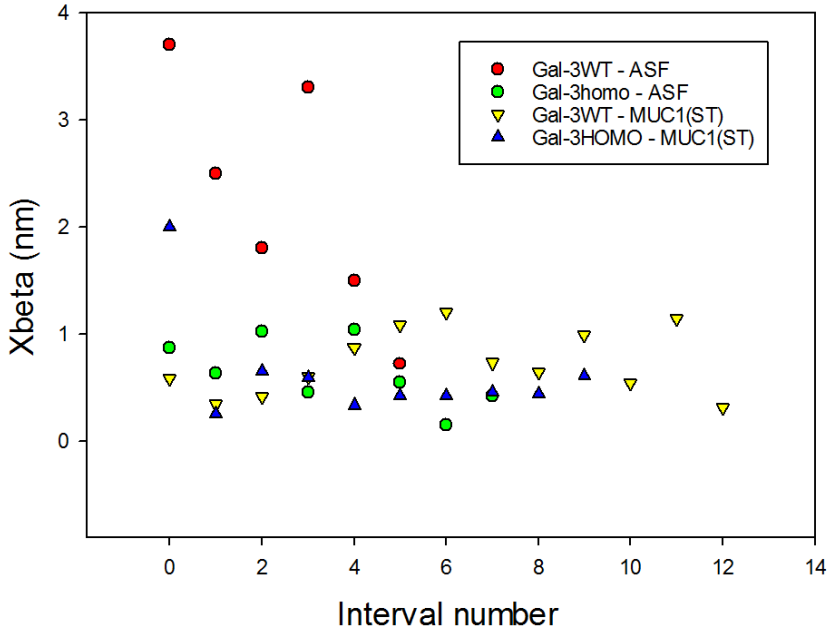

(c) x_β

Figure 4.18: Comparisons of the (a) most likely rupture forces determined from the fit of the P(f) (Eq. 2.6) to the histograms derived from the DFS, (b) dissociation rate, $k_{off,0}$, for each subgroup, and (c) distance from bound to transition state, x_β, for each subgroup for all the galectin - glycoprotein systems. The parameters are extracted from the respective DFS (Figure 4.5, 4.9, 4.13 and 4.16). Data for the plots is listed in Table 4.2, 4.3, 4.4 and 4.5.

4.3 Hybrid formation in binary mixtures of galectins

In the second part of this master thesis were the hybrid formation abilities of Gal-3 investigated by allowing Gal-3 to interact with immobilized Gal-1 WT and Gal-7 WT. For these two systems, as for the four previous ones, are galleries of normal and some characteristic curves presented together with the DFS for both systems. At the end of this part the parameters extracted from the DFS that characterizes the interactions and comparison plots, are presented.

4.3.1 Gal-3 WT - Gal-1 WT

Galleries

Figure 4.19 presents a selection of curves observed for the Gal-3 WT - Gal-1 WT molecular pair.

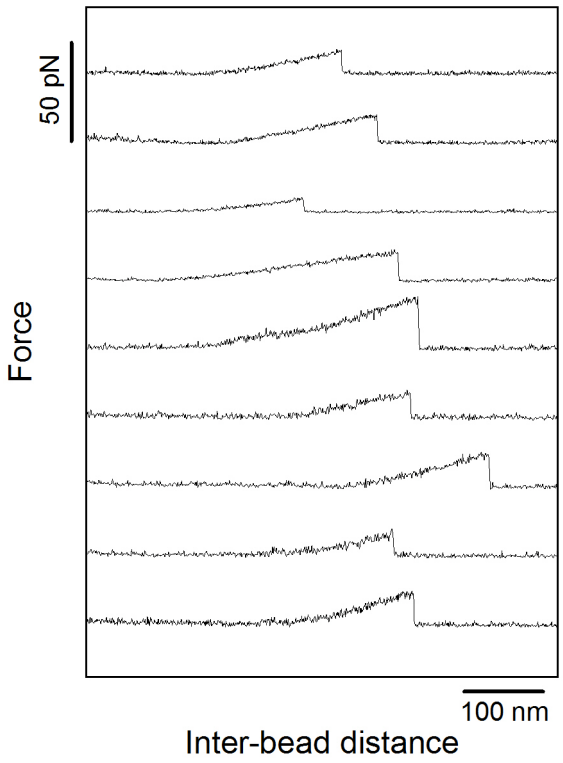

Figure 4.19: Examples of force vs. inter-bead distance curves obtained for the Gal-3 WT - Gal-1 WT system. The curves were generated using OT with polystyrene beads functionalized with Gal-3 WT and Gal-1 WT, respectively.

Dynamic force spectrum

In Figure 4.20 the DFS for the Gal-3 WT - Gal-1 WT system is presented. It was determined based on 492 recorded force curves. Histograms of the distribution of the rupture forces with a corresponding fitted line, P(f), for each subgroup are presented in Figure 4.21. The colours of the histograms corresponds with the colour in the DFS-plot. The most likely rupture force, f*, determined from the fitting line, and the average loading rate of the subgroup, r_f, is included in each histogram.

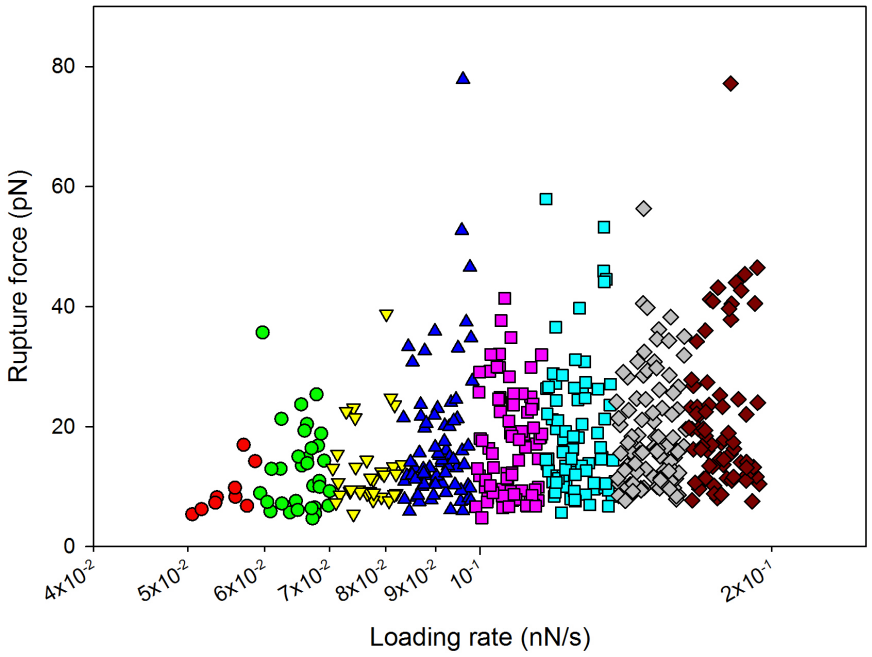

Figure 4.20: Dynamic force spectrum obtained from the interactions between Gal-3 WT and Gal-1 WT showing the distribution of the rupture force (y-axis) with increasing loading rate (logarithmic x-axis). Subgroups for further histogram analysis is indicated with different colours. The plot is generated based on information contained in force curves obtained with OT with polystyrene beads functionalized with Gal-3 WT and Gal-1 WT, respectively.

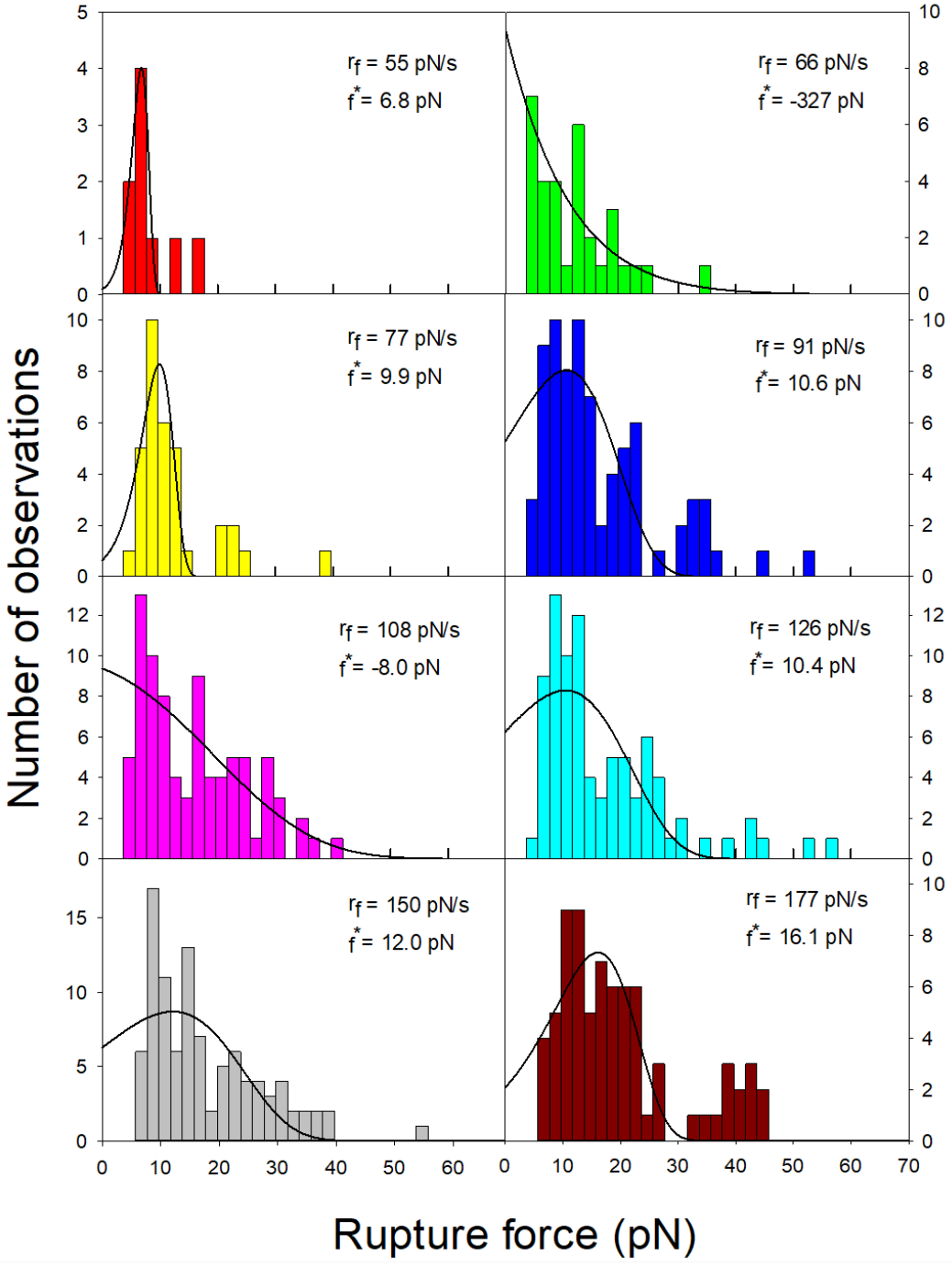

Figure 4.21: Histograms revealing the distribution of experimentally determined inter-molecular rupture forces between Gal-3 WT and Gal-1 WT within an interval of loading rates predefined from the continuous distribution of bond rupture observations plotted in a rupture force vs. log loading rate plot (DFS-plot). The most likely rupture force, f*, and the average loading rate, r_f, for the subgroup is included in each histogram. The continuous line shows the fit of P(f) (Eq. 2.6) to the histograms. The rupture observations were obtained from OT using polystyrene beads functionalized with Gal-3 WT and Gal-1 WT, respectively. The colour of each histogram correspond to the defined loading rate intervals in the DFS-plot in Figure 4.20.

4.3.2 Gal-3 WT - Gal-7 WT

Galleries

Figure 4.22 represents of typical force curves obtained during the investigation of interaction between Gal-3 WT and Gal-7 WT. Figure 4.23 shows more distinct force curves detected during analysis: multiple rupture events (Figure 4.23a) and curves with smoother peaks (Figure 4.23b). The system was found to show a higher frequency of force curves with multiple rupture events and non-exponential increase in force than the Gal-3 WT - Gal-1 WT system.

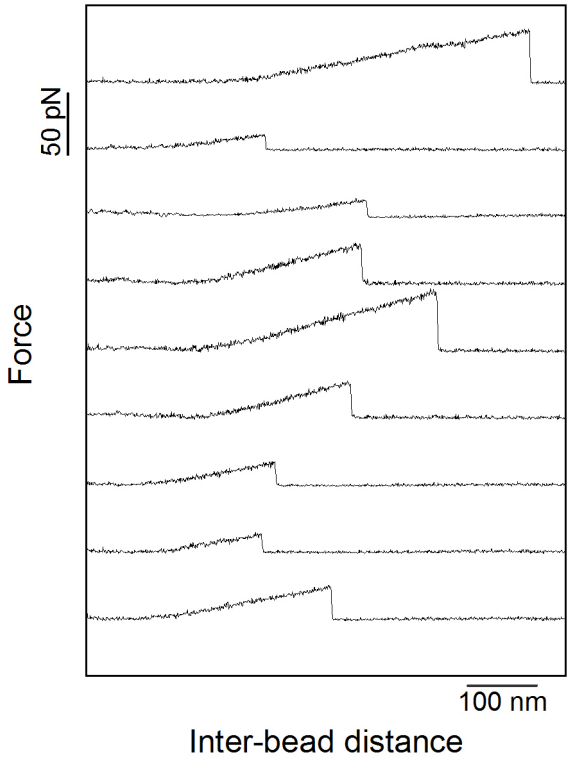

Figure 4.22: Examples of typical force vs. inter-bead distance curves obtained for the Gal-3 WT - Gal-1 WT system. The curves were generated using OT with polystyrene beads functionalized with Gal-3 WT and Gal-7 WT, respectively.

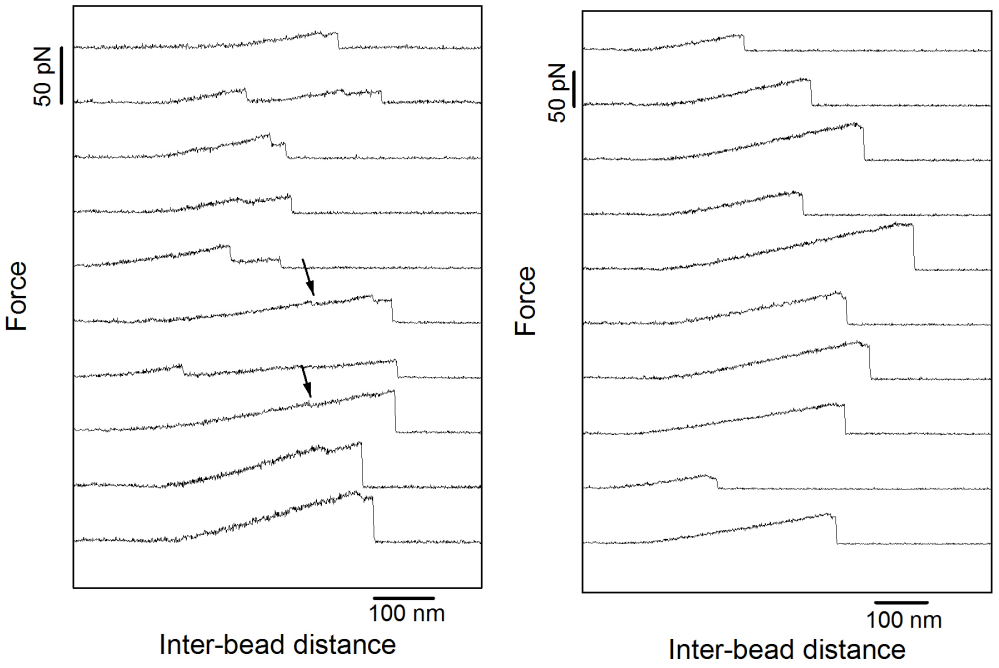

(a) Multiple rupture events **(b)** Smooth peak

Figure 4.23: Examples of distinct force vs. inter-bead distance curves obtained for the Gal-3 WT - Gal-7 WT system. (a) Selection of force versus distance curves showing multiple rupture events. (b) Examples of curves with smooth peak. The curves were generated using OT with polystyrene beads functionalized with Gal-3 WT and Gal-7 WT, respectively. Arrows indicate weak force jumps.

Dynamic force spectrum

In Figure 4.24 is the DFS plot presented for the Gal-3 WT - Gal-1 WT system, determined from 789 recorded force curves. Histograms of the distribution of the rupture forces with a corresponding fitted line, P(f), for each subgroup are presented in Figure 4.25. The colours of the histograms corresponds with the colour in the DFS-plot. The most likely rupture force, f*, determined from the fitting line, and the average loading rate of the subgroup, r_f, is included in each histogram.

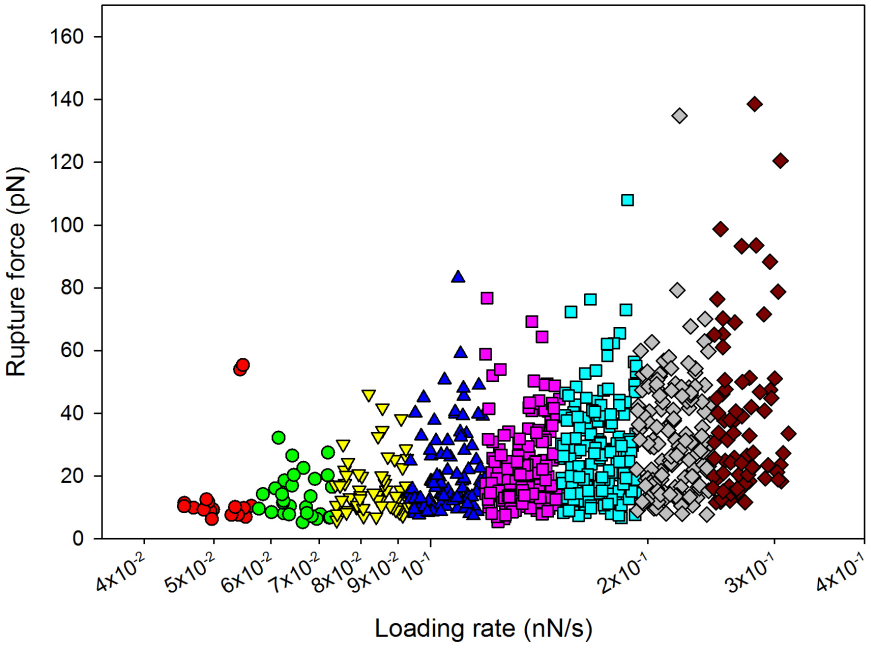

Figure 4.24: Dynamic force spectrum obtained from the interactions between Gal-3 WT and Gal-7 WT showing the distribution of the rupture force (y-axis) with increasing loading rate (logarithmic x-axis). Subgroups for further histogram analysis is indicated with different colours. The plot is generated based on information contained in force curves obtained with OT with polystyrene beads functionalized with Gal-3 WT and Gal-7 WT, respectively.

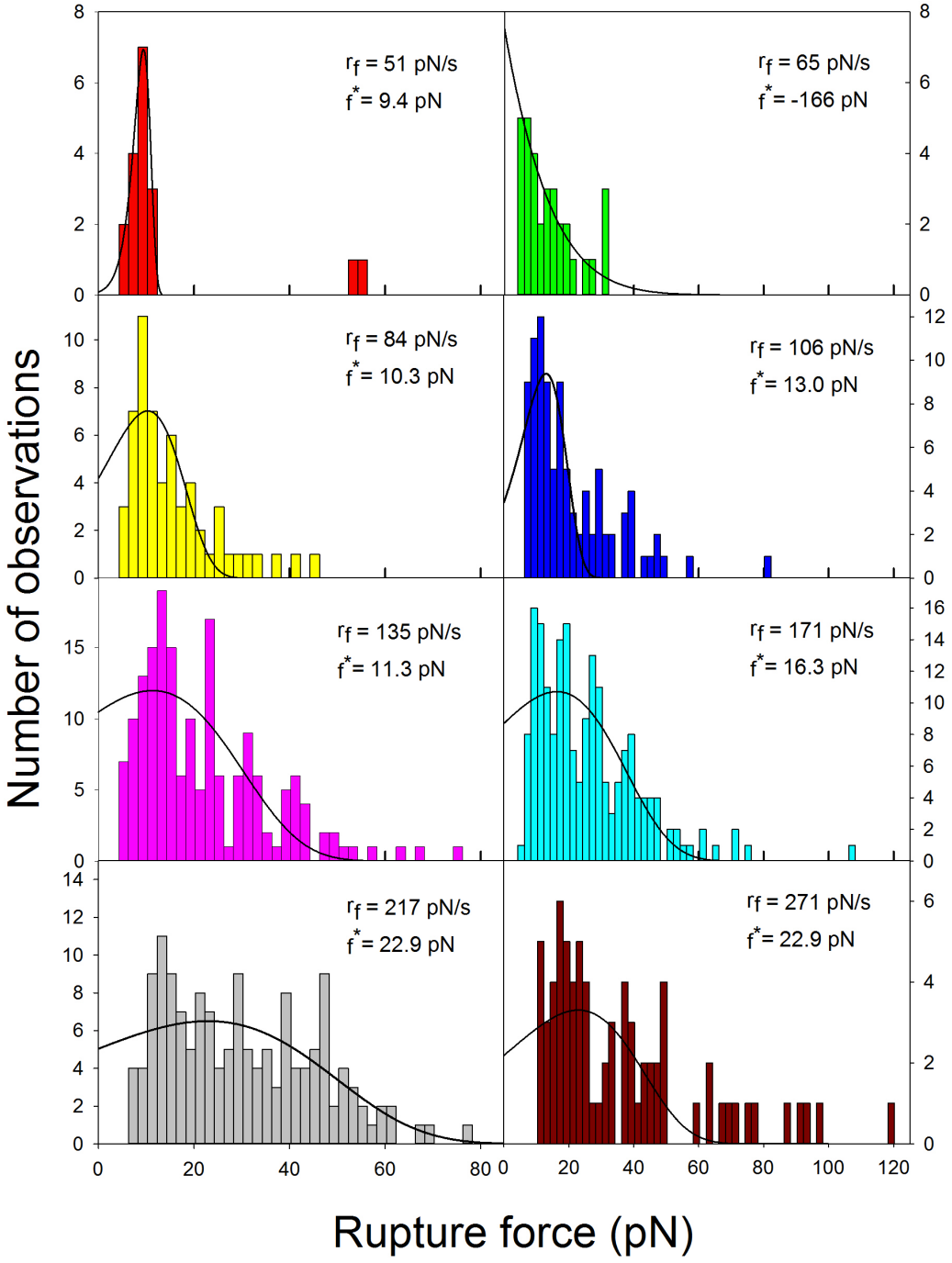

Figure 4.25: Histograms revealing the distribution of experimentally determined inter-molecular rupture forces between Gal-3 WT and Gal-7 WT within an interval of loading rates predefined from the continuous distribution of bond rupture observations plotted in a rupture force vs. log loading rate plot (DFS-plot). The most likely rupture force, f*, and the average loading rate, r_f, for the subgroup is included in each histogram. The continuous line shows the fit of P(f) (Eq. 2.6) to the histograms. The rupture observations were obtained from OT using polystyrene beads functionalized with Gal-3 WT and Gal-7 WT, respectively. The colour of each histogram correspond to the defined loading rate intervals in the DFS-plot in Figure 4.24.

4.3.3 Parameters characterizing Gal-3 - galectin interactions

Based on the probability density function P(f) (Eq. 2.6) fitted to the histograms presented for each system above (section 4.3.1 and 4.3.2), a set of coefficients describing the energy landscape of the interactions could be extracted/calculated using iNanoTracker, as described in section 2.3.1. Table 4.7 and 4.8 summarizes the number of observations in each subgroup, most likely rupture force, f*, the average loading rate, r_f and estimates of the coefficients $k_{off,0}$ and x_β, for the systems Gal-3 WT - Gal-1 WT and Gal-3 WT - Gal-7 WT, respectively. A comparison of the most likely rupture force, f*, for each DFS interval as a function of loading rate, r_f, for both systems are presented in Figure 4.26. The variation in the most probable rupture force, f*, for each subgroup is visualized by box plots in Appendix B for both systems.

Table 4.7: Parameters characterizing the energy landscape of the interaction between Gal-3 WT and Gal-1 WT: most likely rupture force (f*), the average loading rate (r_f), dissociation rate ($k_{off,0}$), and distance between the bound and transition state (x_β).

Interval	No. of observations	r_f [pN/s]	f* [pN]	$k_{off,0}$ [1/s]	x_β [nm]
0	9	55	6.8	0.3	2.8
1	32	66	N.A.*	N.A.*	N.A.*
2	34	77	9.9	0.8	1.4
3	77	91	10.6	3.1	0.41
4	83	108	N.A.*	N.A.*	N.A.*
5	85	126	10.4	4.4	0.33
6	97	150	12.0	4.6	0.31
7	75	177	16.1	2.8	0.54

* For these distributions reliable fitting of the P(f) function was not possible.

Table 4.8: Parameters characterizing the energy landscape of the interaction between Gal-3 WT and Gal-7 WT: most likely rupture force (f*), the average loading rate (r_f), dissociation rate ($k_{off,0}$), and distance between the bound and transition state (x_β).

Interval	No. of observations	r_f [pN/s]	f* [pN]	$k_{off,0}$ [1/s]	x_β [nm]
0	18	51	9.4	0.15	2.3
1	32	65	N.A.*	N.A.*	N.A.*
2	58	84	10.3	2.9	0.48
3	94	106	13.0	2.4	0.57
4	173	135	11.3	3.8	0.20
5	190	171	16.3	3.7	0.18
6	149	217	22.9	3.4	0.14
7	75	271	22.9	4.3	0.19

* For these distributions reliable fitting of the P(f) function was not possible.

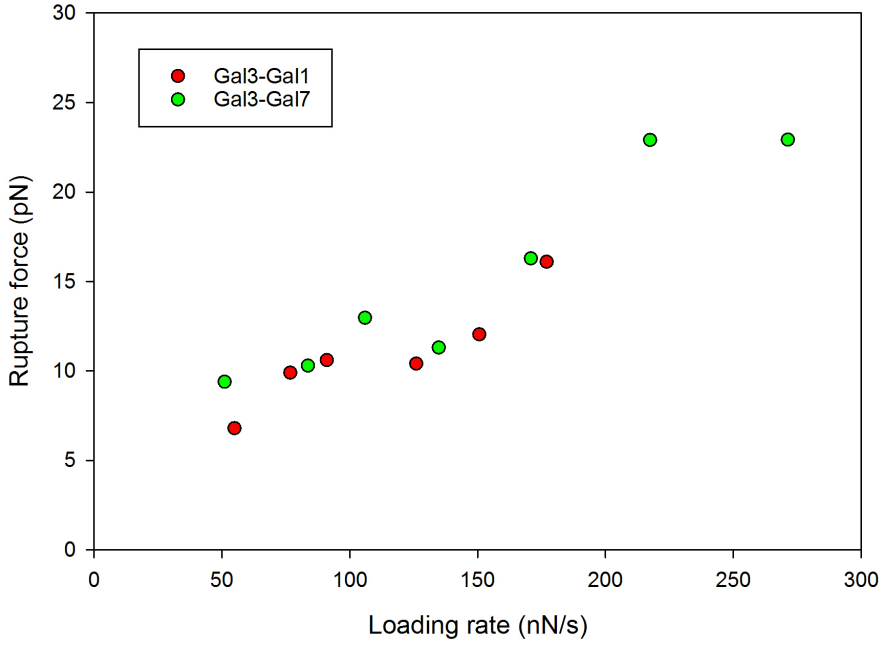

Figure 4.26: Combined dynamic force spectrum for the two systems: Gal-3 WT - Gal-1 WT and Gal-3 WT - Gal-7 WT, obtained from the most likely rupture forces determined from the fit of the P(f) (Eq. 2.6) to the histograms in Figure 4.21 and 4.25, plotted as a function of increasing loading rate.

Chapter 5

Discussion

In this chapter follows a thorough examination of the results presented in Chapter 4. The first part examines the abilities of Gal-3 to interact with the different ligands based on the interaction frequencies. In the second part are the interactions between Gal-3 and glycoprotein discussed on the basis of force - distance curves of the systems and what information can be extracted from these. The next part evaluates the DFS of the Gal-3 - glycoprotein systems and comparing the coefficients determined from these. The hybrid forming abilities of Gal-3 are discussed based on the force - distance curves and DFS. Next is an evaluation of the suitability of the Bell-Evans model to describe the systems investigated in this master thesis. Finally, an evaluation of OT as a tool to study glycan - lectin interactions is presented.

5.1 Interaction abilities of Gal-3 WT

To verify that specific interactions do occur between Gal-3 and the different ligands investigated in this thesis, a set of negative controls were executed and compared with the interaction frequencies of the main systems. The proteins Siglec-9, AlgE4 and BSA, in addition to naked NH_2-functionalized polystyrene beads were chosen as controls because of their non-glycosylated state and thus, not considered typical ligands for Gal-3. However, the results of interaction frequencies presented in Figure 4.1 revealed some interesting observations; both the Siglec9 protein and NH_2 functionalized beads were found to interact with relative high frequency with Gal-3 WT compared to the other negative controls and the main systems, as can be observed in Figure 4.1, 4.2 and Table 4.1. And especially strongly to naked NH_2-functionalized polystyrene beads. The interactions observed may originate from different nonspecific interactions when weak forces forms between the two molecules. This hypothesis is supported by the fact that the orientation of the proteins on the bead surface is random; when immobilizing molecules using the procedure described in the current study, it is not possible to observe or determine the orientation of the immobilized proteins. The EDC reagent covalently links two primary amines (one located on the bead, the other one on the protein) to yield amide bonds, but which amine group on the protein is linked, is random and thus varies from bead to bead and location on the bead itself.

These results are useful in the sense that they confirm that the beads are successfully coated with the respective proteins. Even though the interaction frequency between Gal-3 WT and naked NH_2-functionalized beads is found to be relatively high compared to the other proteins, these type of interactions can be considered to be neglected in the main experiments because of the absence of interactions when investigating AlgE4. Thus, the density of protein on the bead surface is sufficient to prevent Gal-3 WT to possibly interact with the NH_2 residues on the bead. The same protein:beads concentration ratio were used in all experiments, and are thus comparable. Based on this, it can be concluded that interactions observed for the main systems are not affected by the nonspecific Gal-3 - NH_2 interactions.

Interaction frequencies of the main systems presented in Figure 4.2 suggest that both forms of Gal-3 interacted more frequently to MUC1(ST) than to ASF and generally interacted Gal-3 homodimer less frequently to the two glycoconjugates than Gal-3 WT. One reason for this behavior may be the nature of the glycoproteins; ASF if a globular protein, whilst MUC1(ST) is a linear, more flexible protein, making contact and thus, potentially interaction, more probable.

The errors presented in Table 4.1 reflect a high variation in the data obtained for different bead pairs, which can be further explained by the underlying data presented in Appendix A. This emphasizes that the interactions may be influenced by factors that are challenging to control and quantify. Some of the observed variation is probably due to the known importance of the relative z-position of the beads (Siarpilina 2017). The interactions between the bead pair also varied during the investigation of the main systems. In most cases, several bead pairs were investigated for interaction before finding beads that did. Additionally, when determining the interaction frequency for the systems only the force jumps that were possible to fit the slope to, for which the loading rate could be determined were included in the calculation. Thus, there were interactions that occurred that were not included in the calculation of the frequency. However, this applies to all the systems further investigated in the thesis, meaning that the relative differences are most likely not affected.

Based on the arguments just discussed, it is reasonable to believe that the vast majority of interactions observed and analyzed in the current study are specific interactions between the galectin and the respective ligand.

5.2 Gal-3 - glycoprotein interaction and multivalency

Based on the force-distance curves presented for each Gal-3 - glycoprotein system in section 4.2 and the conclusions from the interaction frequencies discussed above, it is clear that Gal-3 interacts with both of the glycoproteins ASF and MUC1(ST) in both the WT and homodimer form, and that the optical tweezers instrument is able to quantify these interactions. This is consistent with previous findings (Dam *et al.* 2005, Kopitz *et al.* 2014, Artigas *et al.* 2017, Haug 2017, Bugge 2017). Figure 4.3, 4.7, 4.11a and 4.15a show examples of typical force curves obtained for the Gal-3 - glycoprotein systems. The curves show a clear increase in force with increasing inter-bead distance and a sudden force drop. This rise followed by a sudden drop in the force most likely corresponds to a bond being pulled with constant force when the beads are pulled apart until it yields to the force and ruptures. This scenario is illustrated in Figure 5.1.

The error in the force measurements by the OT is reported to be ± 1 pN (Siarpilina 2017). However, as the force curves in section 4.2 show, the error is not significant relative to the binding forces (peak height) detected, but should be kept in mind

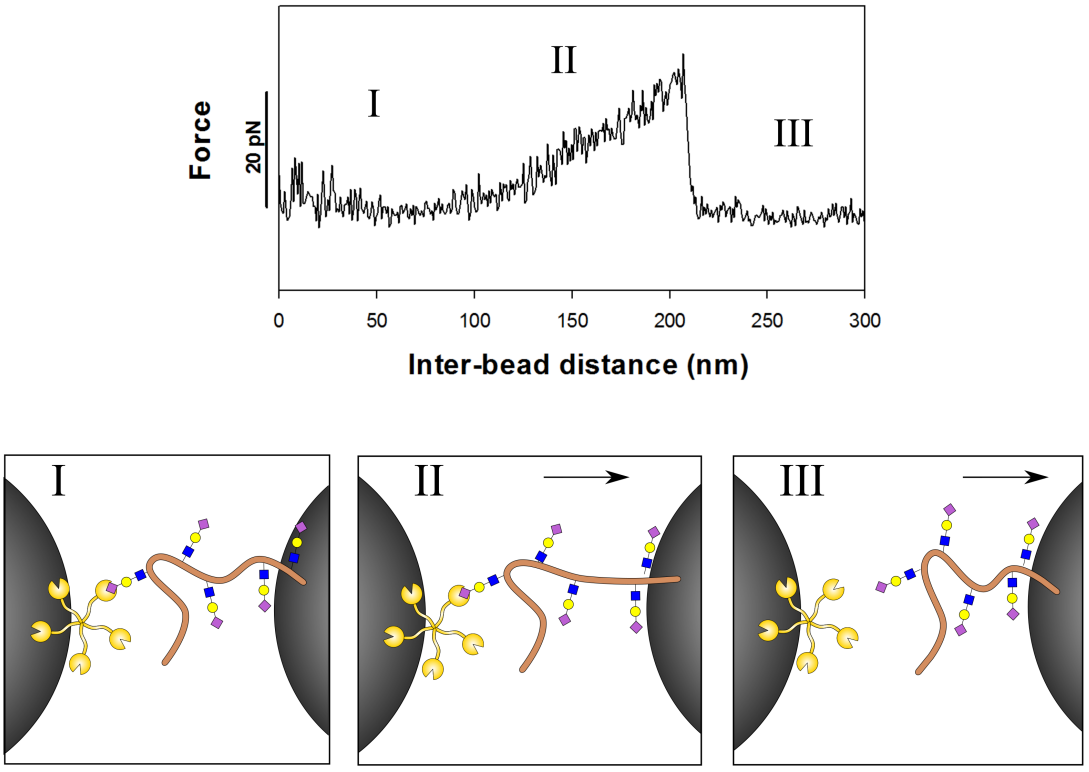

Figure 5.1: Illustration of assumed interaction scenarios between the galectin and the glycoprotein giving rise to force jumps recorded by the OT.

for future measurements in the case of observation of smaller rupture forces (<5 pN).

Figure 4.3b presents more detailed representation of a selection of curves with a clear exponential rise in force. This is a good indication of single molecular interaction, meaning only one pair of galectin - ligand is involved the interaction underlying the rupture event.

Figure 4.11b and 4.8a show rupture events indicating significantly higher rupture forces than the typical ones (up to 100 pN for Gal-3 WT - MUC1(ST) and up to 80 pN for Gal-3 homodimer - ASF). Many of these curves also show an exponential increase in rupture force, indicating that only one pair of galectin - ligand is responsible for the strong force. However, the frequency of these high rupture forces was low as shown in Figure 4.9 and 4.13. Thus, these events can be considered rare, but they are interesting as they show how strong these interactions are able to get. Rupture forces around 100 pN between Gal-3 WT and MUC-1(ST) were also observed by Øystein Haug in his master thesis studying the Gal-3 - MUC1(ST) system using the same approach (Haug 2017).

All of the Gal-3 systems also produced force curves showing multiple force jumps, as presented in Figure 4.4, 4.8b and 4.6. These curves are recognized by force events characterized by two or more jumps. Interestingly, some curves obtained for the Gal-3 WT - MUC1(ST) system presented in Figure 4.12b reveals curves

with a rounded, flat peak, compared to the other previously discussed curves. The origin of this phenomenon is difficult to identify based on this information alone. However, it can be a result of multiple bonds rupturing successively as illustrated in different scenarios in Figure 5.2. Again, a critical factor related to this situation is the concentration of galectin in the bead functionalization mixture, as well as the concentration of the crosslinker and the duration of the functionalization reaction, which together determines the density of galectin on the bead. If the concentration is high, the chance of multiple interactions increases due to the high amount of displayed proteins on the contact surface of the beads. This hypothesis may be supported by Haug's studies, where 10 - 30-fold higher incubation concentration of the proteins in the functionalization mixture than in the current study (0.1 - 0.3 g/l compared to 0.09 g/l in the current study) resulted in non-exponential, plateau-like force curves and a broad distribution of rupture forces within the force loading rate intervals (Haug 2017).

The force curves also revealed a higher frequency of multiplicity in the force curves for the MUC1(ST) systems. Again, this may be due to the linear, more flexible structure of the protein compared to the globular ASF protein. Due to this, it is reasonable to believe that MUC1(ST) has a higher probability of interacting with several Gal-3 CRD's.

However, multiple interactions can also arise due to the multiple CRDs located on the same Gal-3 molecule also illustrated in Figure 5.2. This multiplicity is a consequence of Gal-3's ability to form pentamers, as mentioned in section 2.1.2. Furthermore, as showed in Figure 2.2, both the ASF and the MUC1 ligands also possess multiple Gal-3 epitopes which increases the probability of multiple interactions. As mentioned, when immobilizing molecules using the procedure described in the current study, it is not possible to observe or determine the orientation of the immobilized proteins. Thus, orientation of the galectins and the CRD, and if they are assembled together to pentamers prior to immobilization, is difficult to determine. However, considering the distance between the rupture events, pentamer formation may be an explanation of the multiple force jumps observed in a fraction of the curves.

Even though monovalent interaction was strived for in this study, a lot of recent published articles suggests to focus more on the multivalent properties of lectins (Garcia-Moreno *et al.* 2017, Ortiz Mellet *et al.* 2017, Müller *et al.* 2016). As mentioned in the theory, this multivalency of Gal-3 can be of significant importance for its biological functions, including its functions in pathogenesis and cancer. When isolating the galectins and glycans, they are removed from their natural environment, and both the specificity and affinity are believed to be altered *in vitro* compared to *in vivo* (Cummings *et al.* 2017). Thus, it may be more relevant to study the multivalent activity of Gal-3.

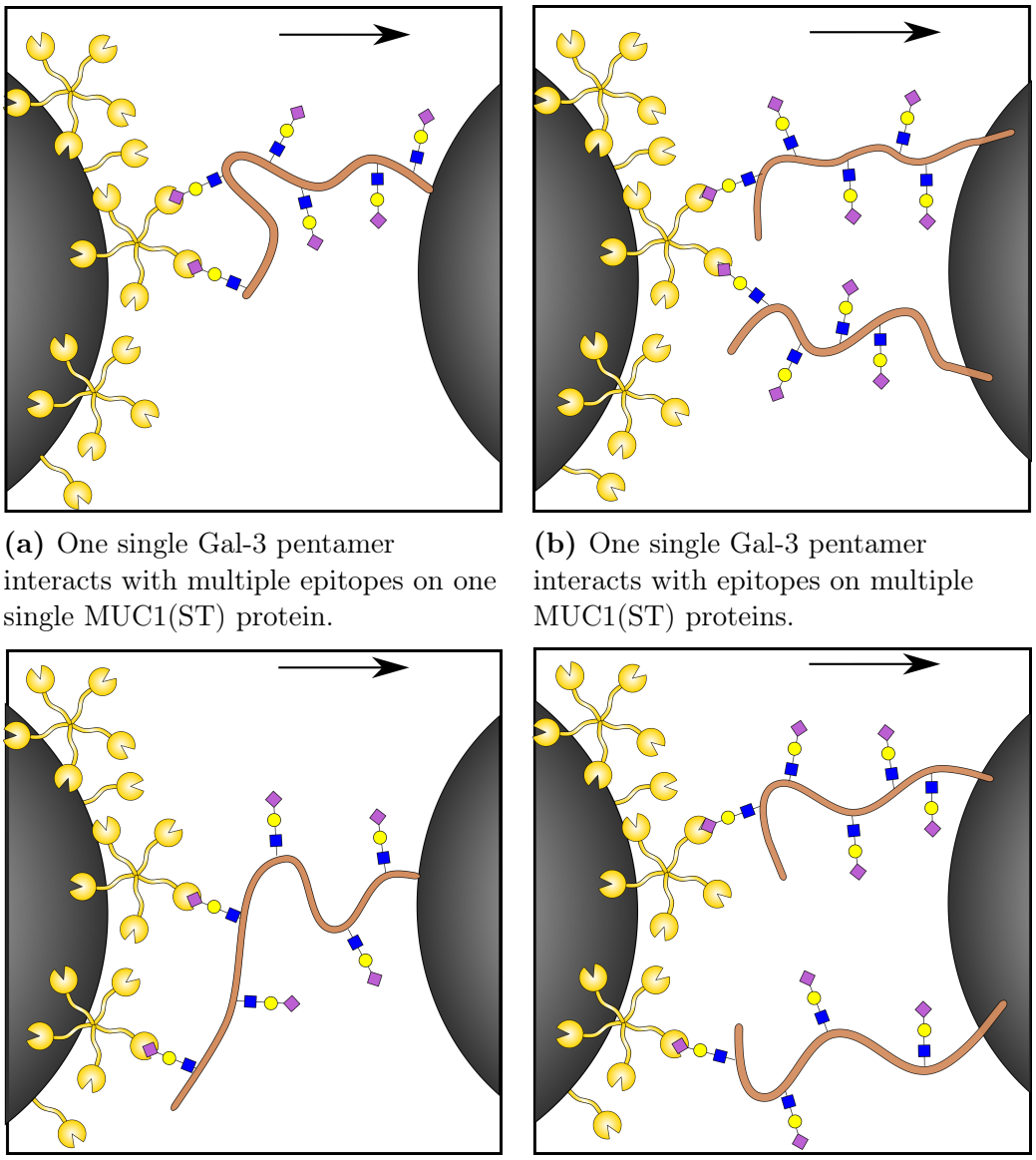

(a) One single Gal-3 pentamer interacts with multiple epitopes on one single MUC1(ST) protein.

(b) One single Gal-3 pentamer interacts with epitopes on multiple MUC1(ST) proteins.

(c) Several Gal-3 pentamers interacts with epitopes on the same MUC1(ST) protein.

(d) Several Gal-3 pentamers interacts with epitopes on two separate MUC1(ST) proteins.

Figure 5.2: Suggestions of different scenarios occurring during the investigations of intermolecular interactions between Gal-3 and glycoproteins giving rise to multiplicity observable in the recorded force curves.

5.3 Comparison of the interaction characteristics of the Gal-3 - glycoprotein systems studied

As shown in Figure 4.18a, the rupture force increases with increasing loading rate for all the systems, which correlates with theory (E. Evans and Ritchie 1997). The rupture forces range between 6.2 - 13.6 pN for loading rates between 45 - 158 pN/s for the Gal-3 WT – ASF system, between 10.1 - 28.1 pN for loading rates between

108 - 316 pN/s for Gal-3 homodimer – ASF, between 13.8 - 23.3 pN for loading rates between 63 - 213 pN/s for Gal-3 WT – MUC1(ST), and finally, between 8.8 - 28.6 pN for loading rates between 44 - 233 pN/s for Gal-3 homodimer - MUC1(ST) (Table 4.2, 4.3, 4.4 and 4.5). The figure also reveals that the results obtained in this study suggest that both structures of Gal-3 exerts stronger interactions to MUC1(ST) than to ASF at same loading rates, and strongest to Gal-3 WT. This could also be observed in the galleries and in the DFS plot (Figure 4.11b and 4.13). However, the systems can only be compared at lower loading rates as for some system it was not possible to obtain rupture forces at high loading rates. The most obvious reason for this difference may be that the sugar moieties at the epitopes of the ligands are different: LacNAc for ASF and Neu5Ac on the MUC1(ST) protein as shown in Figure 2.2. This observation is interesting in the sense that Yu *et al.* 2007 concluded in their study that Gal-3 and MUC1(ST) did not interact. Another interesting aspect is that LacNAc is believed to be the preferred ligand of Gal-3 as mentioned in the theory (Dumic *et al.* 2006). However, the results obtained in the current study suggest that the Neu5Ac monomer may not have high impact on the interaction between the Gal and GalNAc residues and the binding pocket of Gal-3. They even suggest that the residue increases the strength of the interaction to MUC1(ST). However, the high strength might also be due to the multiplicity of the glycoprotein. As discussed in the previous section, multiple rupture events were observed for all systems, especially for the MUC1(ST) systems (Figure 4.12b and 4.15b). The rupture of several bonds simultaneously may not always be directly observable in the force curves as multiple force jumps, but rather as broad distributions of strong rupture forces as can be observed in the histograms associated with the DFS for the systems (Figure 4.14 and 4.17), according to Sulchek *et al.* 2005. Sulchek *et al.* showed/concluded in their study of MUC1 - antibody interactions using the AFM approach, that rupture forces increases and histogram distributions broadens with increasing parallel individual bonds. This agrees with the DFS of the systems, as histograms at especially higher rupture forces has a broader distribution (Figure 4.6, 4.10, 4.14 and 4.17). The rupture forces and loading rates measured are comparable to Hadjialirezaei *et al.* 2017, who found increasing rupture forces from 6 pN to 37 pN over the loading rate interval from 29 to 137 pN/s, and Haug 2017 who found rupture forces increasing from 11 to 31 pN over the loading rate interval 37 - 72 pN/s.

Average $\overline{k_{\text{off},0}}$-values for the systems range between 1.1±0.7 to 3.5±2.0 s^{-1} corresponding to lifetimes between 1.2±0.8 and 0.4±0.2 s (Table 4.6). The outliers were not taken into consideration when calculating the mean (especially for the Gal-3 homodimer ASF system that have two obvious outliers). Figure 4.18b indicates that bonds forming to Gal-3 WT have a longer lifetime than for those forming to Gal-3 homodimer. However, due to the large errors, it is difficult to conclude on anything. These values are within the range of previous findings of this parameter between MUC1(Tn) and the macrophage galactose-type lectin (MGL) (Hadjialirezaei *et al.* 2017).

$\overline{x_\beta}$ presented in Table 4.6 and distribution in Figure 4.18c show a distance from bound to transition state ranging between 0.5±0.1 nm and 2.3±1.1 nm. Gal-3 WT - ASF deviates from the other systems with more than twofold the distance

of the other systems, however, there can not be observed any significant difference between the three other systems. As for the $\overline{k_{off,0}}$-values, uncertainty is high which makes it difficult to draw clear conclusions.

Generally, based on the parameters derived from the DFS-plots, no distinct relationship can be observed between the two forms of Gal-3: WT and homodimer. The reasons why the OT did not detect any difference between the homodimer and the WT may be the orientation of the proteins relative to the CRD. As earlier mentioned, it is difficult to predict and control the orientation due to the random linking of amine groups of the EDC reagent. Still, the CRDs of the homodimer is most likely linked in such way that they are pointing in opposite directions and thus, only one of the CRDs are displayed towards the ligand and only this one is thus able to create interaction. Such a scenario might explain why no significant difference can be observed between the two structural forms of Gal-3 studied. However, the orientation of the galectin is not expected to affect the binding properties, but rather the frequency of multiple binding events.

5.4 Hybrid forming abilities of Gal-3 WT

A new aspect within glycoscience which has recently been discovered, are the ability of galectins to interact with each other to form heterodimeric hybrids. In this current study Gal-3 WT were exposed to two different galectins: Gal-7 WT and Gal-1 WT, to elucidate Gal-3's ability to interact with other galectins.

Force curves obtained for the two systems presented in section 4.3 reveal that interaction between Gal-3 WT and the two galectins: Gal-1 WT and Gal-7 WT, occurs. As for the Gal-3 - glycoprotein systems, the interactions form and give rise to distinct peaks corresponding to their forced rupture as explained previously in the discussion, and illustrated in Figure 5.1. These results are consistent with the interesting findings of Miller *et al.* that recently published research revealing that trunctated Gal-3 (Gal-3 CRD) do form heterodimeric hybrids with the two galectins: Gal-1 and Gal-7 (Miller *et al.* 2018). In the current master study the chimera type Gal-3 was used in this current study, which opens up for the possibility that the N-terminal domain might be involved in the interactions with the respective galectin observed. However, due to the nature of the method, exactly how these molecules interact is difficult to predict. Similar heterodimeric hybrid interactions have also been discovered between Gal-9 and both Gal-8 and Gal-3 (Miyanishi, 2007) and other C-type tissue lectins (Zhu, 2013, Miyake, 2015). These previously published findings support the current findings.

The DFS-plots of the Gal-3 - galectin interactions are consistent with the theory in the sense that they reveal increased rupture force with increasing loading rate (E. Evans and Ritchie 1997). The rupture forces range between 6.8 - 16.1 pN for loading rates between 55 - 177 pN/s, for the Gal-3 WT – Gal-1 WT system, and between 9.4 - 22.9 pN for loading rates between 51 - 271 pN/s for the Gal-3 WT - Gal-7 WT system. As the DFS-plots in Figure 4.20 and 4.24 shows, it was

detected a higher fraction of strong rupture forces for the Gal-3 WT - Gal-7 WT system. However, compared to Gal-3 WT - Gal-1 WT system, there is no significant difference in their DFS (Figure 4.26). For some histograms, however, the P(f) equation could not be fitted and thus the most likely rupture force as well as the $k_{off,0}$ and x_β parameters could not be determined, due to deviating distribution (Figure 4.21 and 4.25). The parameters describing the energy landscape of the two systems are presented in Table 4.7 and 4.8, extracted from the DFS-plots. $\overline{x_\beta}$-values were found to be 0.6 ± 0.4 nm for the Gal-3 WT - Gal-1 WT system, and 0.3 ± 0.2 nm for the Gal-3 WT - Gal-7 WT system. And $\overline{k_{off,0}}$-values to be 3.1 ± 1.4 s^{-1} for Gal-3 WT - Gal-1 WT system, and 3.4 ± 0.6 s^{-1} for the Gal-3 WT - Gal-7 WT system. The $k_{off,0}$ value correspond to a lifetime of 0.5 ± 0.4 s and 0.30 ± 0.06 s for the Gal-3 WT - Gal-1 WT and Gal-3 WT - Gal-7 WT systems, respectively. These results suggests that the Gal-3 WT- Gal-1 WT system has twice the separation distance between the bound and transition state than of Gal-3 WT - Gal-7 WT system. However, there is very high uncertainties associated with these values, which is also reflected in the distribution in the histograms in Figure 4.21 and 4.25. Especially the distribution of the last four histograms for the Gal-3 WT - Gal-7 WT are very broad. As discussed previously, one reason for this trend might be multiplicity. This can also be observed in the galleries of the system which shows force curves with high force and non-exponential increase in force (Figure 4.22). Multiplicity might also explain the high fraction of force jumps with a smoother peak as shown in Figure 4.23b. The hybrid forming abilities of Gal-3 revealed in this thesis, might explain the interaction frequency between Gal-3 WT and Siglec9 in Figure 4.1.

Based on arguments just discussed and the results of the interaction frequencies, it is reasonable to believe that Gal-3 interacts with Gal-1 and Gal-7 with a higher specificity than to BSA and AlgE4 proteins. However, this is a very new research area within the glycobiology field. Because of this, not much research has so far been executed in this area which makes it difficult to draw conclusions. However, these are very interesting new results which can potentially change our interpretation of the behavior of galectins *in vivo* and extend their repertoire of functions such as signalling, crosslinking and lattice formation, drastically. Many new questions arises due to these findings as how they interact, when do they optionally form hybrids and in which situations. These questions should be further addressed in future studies.

5.5 Evaluation of the suitability of the Bell-Evans model in the current study

An overall trend of the investigated systems analyzed in this thesis, is non-linear loading rate vs. most probable rupture force curves (Figure 4.18a and 4.26). The curves reveal a slow increase in rupture force at lower loading rates until reaching a loading rate where the rupture force increases more rapidly. This can also be observed in DFS of the respective systems, especially Gal-3 WT - ASF and Gal-3

WT - MUC1(ST), that show a very flat distribution at lower loading rates (Figure 4.5 and 4.13).

As mentioned in section 2.3, the Bell-Evans model is based on a number of assumptions including the following: 1) such as the investigated system is far from equilibrium, due to the presence of the external force, and 2) the rupture event observed originates from a single bond rupture between a single pair of molecules (E. Evans and Ritchie 1997). Thus, the bond rupture observed is considered irreversible and the rebinding of bonds are neglected, resulting in a linear development of the loading rate vs. most probable rupture force. Observations made in this study reveal that multiple bindings do occur in all systems, hence, making the assumptions in the Bell-Evans model unjustified. As a consequence of the poor suitability of the model to explain these systems, parameters derived from the DFS will give a false interpretation of the systems. However, Friddle and colleagues has proposed an improved model based on the Bell-Evans model. They divide the curve into two regimes: far and near equilibrium (Friddle *et al.* 2012), where the near equilibrium regime takes into account that the system is reversible. The occurrence of rebinding,which seems to be the case in the current study. Both linear and non-linear regimes are found to be inherent and ubiquitous in many systems investigated, thus, the implementation of a new model is highly necessary and appropriate. Hence, the Friddle–Noy–de Yoreo model may be a better model to describe the systems in the current thesis and should be implemented and used in the analysis protocol for future experiments with similar distributions.

5.6 Evaluation of optical tweezers as a tool to study glycan-lectin interactions

Based on the results from the current study, OT can be considered a powerful tool for investigating weak single inter-molecular interaction forces. Still, both advantages and disadvantages of the technique were revealed during execution of this study, and they should be taken into consideration to address its limitations. OT is a potentially good tool to investigate the cross-linking ability of galectins. Through immobilizing the glycoprotein on all beads and add free galectins in the solution, the galectin gets the opportunity to cross-link glycoproteins on two separate beads and by retracting the cross-linked beads the interaction can be quantified and compared to situations without the cross-linking opportunity. On the contrary, OT may not be the best alternative to investigate multivalency of a single lectin molecule. Due to the type of force signal OT produce, it is difficult to distinguish if the multiple jumps originates from one or multiple lectin molecules. Regardless, as mentioned, when studying monovalent lectin-ligand interactions in isolation, an unnatural situation is created and their behavior observed *in vitro* may not be comparable to the behavior *in vivo*. Naturally, these interactions would be affected by an incredible amount of factors impossible to reproduce when immobilizing isolated molecules on the surface of polystyrene beads. One way to

address this disadvantage could be to use living cells as a surface in OT investigation. This approach was used by Herrmann and Sieben 2015 when successfully investigating the interaction between a virus and living target cells. This may also be a promising method in the sense that it allows researchers to overcome challenges with mimicking molecule density on the investigating surfaces. This approach might thus open up for new applications of OT and bring researchers one step further towards cracking the sugar code.

Conclusion

To achieve a better understanding of the binding and hybrid forming abilities of the widespread Galectin-3, it was exposed to different glycoproteins and galectins using the sensitive force probe optical tweezers. In the first part of the study, the interactions between two different structural forms of the galectin (wild type and the engineered homodimer) and the two common biological glycoproteins asialofetuin (ASF) and mucin-1 ST (MUC1(ST)) were investigated in different combinations. The results presented in this study provides evidence that interactions between Gal-3 WT and ASF, Gal-3 homodimer and ASF, Gal-3 WT and MUC1(ST) and Gal-3 homodimer - MUC1(ST) do form. The rupture forces increased between 6.2 - 13.6 pN for loading rates between 45 - 158 pN/s for the Gal-3 WT – ASF system, between 10.1 - 28.1 pN for loading rates between 108 - 316 pN/s for Gal-3 homodimer – ASF, between 13.8 - 23.3 pN for loading rates between 63 - 213 pN/s for Gal-3 WT – MUC1(ST), and finally, between 8.8 - 28.6 pN for loading rates between 44 - 233 pN/s for Gal-3 homodimer - MUC1(ST). A slight difference in rupture force was observed between the two glycosylated proteins ASF and MUC1(ST). This difference might be explained by the different sugar moieties on the epitopes: LacNAc on ASF and Neu5Ac on MUC1(ST) or multiplicity due to the structure of the glycoproteins. The results document that Gal-3 interacts with MUC1(ST), contradictory to what has been observed earlier by some researchers (Yu *et al.* 2007). In the second part of the study, the hybrid forming abilities of Gal-3 WT were elucidated by investigating the inter-molecular interactions between Gal-3 WT and the two galectins: Gal-1 WT and Gal-7 WT. It was found that Gal-3 WT seems to exhibit a certain inherent specificity to Gal-1 WT and Gal-7 WT. However, using sensitive-force curves it is difficult to reveal how widespread and specific this interaction is. This should therefore be investigated further.

The results also inspired new questions, especially related to the multivalency of the interactions, a property that is important in order to understand the function of these molecules *in vivo*. The study also showed indications of poor fit of the Bell-Evans model to the data of the systems obtained in the study, which may have resulted in misinterpretation of the parameters derived using the model. Thus, a new model should be implemented, where the Friddle-Noy-de Yoreo (Friddle *et al.* 2012) seems to be a good canidate.

Bibliography

Ahmad, Nisar *et al.* (2004). "Galectin-3 precipitates as a pentamer with synthetic multivalent carbohydrates and forms heterogeneous cross-linked complexes". In: *The Journal of biological chemistry* 279.12.

Ahmad, N *et al.* (2004). "Thermodynamic binding studies of bivalent oligosaccharides to galectin-1, galectin-3, and the carbohydrate recognition domain of galectin-3". In: *Glycobiology* 14.9, pp. 817–825.

Artigas, Gerard *et al.* (2017). "Synthetic Mucin-Like Glycopeptides as Versatile Tools to Measure Effects of Glycan Structure/Density/Position on the Interaction with Adhesion/Growth-Regulatory Galectins in Arrays". In: *Chemistry an Asian Journal* 12.1, pp. 159–167.

Ashkin, A. (1970). "Acceleration and Trapping of Particles by Radiation Pressure". In: *Physical Review Letters* 24.4, pp. 156–159.

Battistel, Marcos D. *et al.* (2014). "NMR of glycans: Shedding new light on old problems". In: *Progress in Nuclear Magnetic Resonance Spectroscopy* 79.C, pp. 48–68.

Belardi, Brian and Carolyn R Bertozzi (2015). "Chemical Lectinology: Tools for Probing the Ligands and Dynamics of Mammalian Lectins In Vivo". In: *Chemistry biology* 22.8.

Bizzarri, Anna Rita and Salvatore Cannistraro (2010). "The application of atomic force spectroscopy to the study of biological complexes undergoing a biorecognition process". In: *Chemical Society Reviews* 39.2, pp. 734–749.

Brown, Ewan R. *et al.* (2012). "Association of galectin-3 expression with melanoma progression and prognosis". In: *European Journal of Cancer* 48.6, pp. 865–874.

Bugge, Ragna Emilie (2017). *Mucins: Galectin 3 interactions measured by atomic force microscopy - Carbohydrate antigens in human health and disease.*

Burchell, Joy, Arron Mungul, and Joyce Taylor-Papadimitriou (2001). "O-Linked Glycosylation in the Mammary Gland: Changes that Occur During Malignancy". In: *Journal of Mammary Gland Biology and Neoplasia* 6.3, pp. 355–364.

Celik, Emrah and Vincent T. Moy (2012). "Nonspecific interactions in AFM force spectroscopy measurements". In: *Journal of Molecular Recognition* 25.1, pp. 53–56.

Corfield, Anthony P. (2015). "Mucins: A biologically relevant glycan barrier in mucosal protection". In: *BBA - General Subjects* 1850.1, pp. 236–252.

Cost, Anna-Lena *et al.* (2015). "How to Measure Molecular Forces in Cells: A Guide to Evaluating Genetically-Encoded FRET-Based Tension Sensors". In: *Cellular and Molecular Bioengineering* 8.1, pp. 96–105.

Cummings, Richard D., Fu-Tong Liu, and Gerardo R. Vasta (2017). *Essentials og Glycobiology, 3rd edition*. Ed. by Ajit Varki. Cold Spring Harbour.

Dam, Tk *et al.* (2005). "Galectins bind to the multivalent glycoprotein asialofetuin with enhanced affinities and a gradient of decreasing binding constants". In: *Glycobiology* 15.11, pp. 1215–1215.

Dosekova, Erika *et al.* (2016). "Nanotechnology in Glycomics: Applications in Diagnostics, Therapy, Imaging, and Separation Processes: NANOTECHNOLOGY IN GLYCOMICS". In: *Medicinal Research Reviews* 37.3.

Dumic, Jerka, Sanja Dabelic, and Mirna Flögel (2006). "Galectin-3: An open-ended story". In: *BBA - General Subjects* 1760.4, pp. 616–635.

Evans, E. and K. Ritchie (1997). "Dynamic strength of molecular adhesion bonds". In: *Biophysical Journal* 72.4, pp. 1541–1555.

Evans, Evan (1999). "Looking inside molecular bonds at biological interfaces with dynamic force spectroscopy". In: *Biophysical Chemistry* 82.2, pp. 83–97.

Evans, Evan and David Calderwood (2007). "Forces and Bond Dynamics in Cell Adhesion". In: *Science (Washington)* 316.5828, pp. 1148–1153.

Farinha, Dina, Maria C. Pedroso de Lima, and Henrique Faneca (2014). "Specific and efficient gene delivery mediated by an asialofetuin-associated nanosystem". In: *International Journal of Pharmaceutics* 473.1-2, pp. 366–374.

Florin, Ernst-Ludwig, Vincent T. Moy, and Hermann E. Gaub (1994). "Adhesion Forces Between Individual Ligand-Receptor Pairs". In: *Science* 264.5157, pp. 415–417.

Friddle, Raymond W., Aleksandr Noy, and James J. De Yoreo (2012). "Interpreting the widespread nonlinear force spectra of intermolecular bonds". In: *Proceedings of the National Academy of Sciences* 109.34.

Gabius, Hans-Joachim, ed. (2009). *The Sugar code : fundamentals of glycosciences*. Weinheim: Wiley-Blackwell. ISBN: 9783527320899.

Gabius, Hans-Joachim and Jürgen Roth (2017). "An introduction to the sugar code". In: *Histochemistry and cell biology* 147.2.

Garcia-Moreno, M. Isabel *et al.* (2017). "The Impact of Heteromultivalency in Lectin Recognition and Glycosidase Inhibition: An Integrated Mechanistic Study". In: *Chemistry – A European Journal* 23.26, pp. 6295–6304.

Hadjialirezaei, Soosan *et al.* (2017). "Interactions between the breast cancer-associated MUC1 mucins and C-type lectin characterized by optical tweezers". In: *PLoS ONE* 12.4.

Han, Liang and Catherine Costello (2013). "Mass spectrometry of glycans". In: *Biochemistry (Moscow)* 78.7, pp. 710–720.

Haug, Øystein (2017). *Studies of MUC1 - Gal3 lectin interaction by the sensitive force probe Optical Tweezers (OT)*.

Herrmann, Andreas and Christian Sieben (2015). "Single-virus force spectroscopy unravels molecular details of virus infection". In: *Integr. Biol.* 7 (6), pp. 620–632.

Huang, Mia L and Kamil Godula (2016). "Nanoscale materials for probing the biological functions of the glycocalyx". In: *Glycobiology* 26.8, pp. 797–803.

JPK, Instruments (n.d.). *NanoTracker 2*. https://www.jpk.com/products/force-sensing-optical-tweezers-and-optical-trapping/nanotracker-2. [Online; accessed 08-December-2017].

Kim, H R *et al.* (1999). "Cell cycle arrest and inhibition of anoikis by galectin-3 in human breast epithelial cells". In: *Cancer research* 59.16.

Klyosov, Anatole A (2008). *Galectins*. Wiley. ISBN: 1-281-38211-6.

Kopitz, JuRgen *et al.* (2014). "Human chimera-type galectin-3: Defining the critical tail length for high-affinity glycoprotein/cell surface binding and functional competition with galectin-1 in neuroblastoma cell growth regulation". In: *Biochimie* 104.

Kuklinski, Stephan and Rainer Probstmeier (1998). "Homophilic Binding Properties of Galectin-3: Involvement of the Carbohydrate Recognition Domain". In: *Journal of Neurochemistry* 70.2, pp. 814–823.

Kuo, Scot C. and Michael P. Sheetz (1992). "Optical tweezers in cell biology (Product Review)". In: *Trends in Cell Biology* 2.4, pp. 116–118.

Liang, Chi-Hui and Chung-Yi Wu (2009). "Glycan array: a powerful tool for glycomics studies". In: *Expert Review of Proteomics* 6.6, pp. 631–645.

Manning, Joachim *et al.* (2017). "Lectins: a primer for histochemists and cell biologists". In: *Histochemistry and Cell Biology* 147.2, pp. 199–222.

Miller, Michelle C *et al.* (2018). "Adhesion/growth-regulatory galectins tested in combination: evidence for formation of hybrids as heterodimers". In: *The Biochemical journal* 475.5.

Moffitt, Jeffrey R. *et al.* (2008). "Recent Advances in Optical Tweezers". In: 77, pp. 205–228.

Müller, Christian, Guillaume Despras, and Thisbe K. Lindhorst (2016). "Organizing multivalency in carbohydrate recognition". In: *Chemical Society Reviews* 45.11, pp. 3275–3302.

Nakahara, S., N. Oka, and A. Raz (2005). "On the role of galectin-3 in cancer apoptosis". In: *Apoptosis* 10.2, pp. 267–275.

Nelson, David L. (2013). *Lehninger principles of biochemistry*. New York.

Neuman, Keir C. and Steven M. Block (2004). "Optical trapping". In: *Review of Scientific Instruments* 75.9, pp. 2787–2809.

Neuman, Keir C. and Attila Nagy (2008). "Single-molecule force spectroscopy: optical tweezers, magnetic tweezers and atomic force microscopy". In: *Nature Methods* 5.6.

Ortiz Mellet, Carmen, Jean-Franois Nierengarten, and Jos M. Garca Fernndez (2017). "Multivalency as an action principle in multimodal lectin recognition and glycosidase inhibition: a paradigm shift driven by carbon-based glyconanomaterials". In: *Journal of Materials Chemistry B* 5.32, pp. 6428–6436.

Oyelaran, Oyindasola and Jeffrey C Gildersleeve (2009). "Glycan arrays: recent advances and future challenges". In: *Current Opinion in Chemical Biology* 13.4, pp. 406–413.

Ruvolo, Peter P. (2016). "Galectin 3 as a guardian of the tumor microenvironment". In: *BBA - Molecular Cell Research* 1863.3, pp. 427–437.

Sciacchitano, Salvatore *et al.* (2018). "Galectin-3: One Molecule for an Alphabet of Diseases, from A to Z". In: *International Journal of Molecular Sciences* 19.2.

Serizawa, Nobuko *et al.* (2013). "Tu1606 Galectin-3 Regulates Gastric Cancer Cell Proliferation Through EGFR Signaling Pathway." In: *Gastroenterology* 144.5.

Siarpilina, Katsiaryna (2017). *Elucidating glycan-mediated interactions at cell surfaces by optical tweezers*.

Solís, Dolores *et al.* (2015). "A guide into glycosciences: How chemistry, biochemistry and biology cooperate to crack the sugar code". In: *BBA - General Subjects* 1850.1, pp. 186–235.

Spiro, Robert G. (1973). "Glycoproteins". In: *Biochemistry* 27, pp. 599–638.

Stockert, R. J. (1995). "The asialoglycoprotein receptor: relationships between structure, function, and expression". In: *Physiological Reviews* 75.3, pp. 591–609.

Sulchek, Todd A. *et al.* (2005). "Dynamic force spectroscopy of parallel individual Mucin1–antibody bonds". In: *Proceedings of the National Academy of Sciences of the United States of America* 102.46.

Sundqvist, Martina *et al.* (2018). "Galectin-3 type-C self-association on neutrophil surfaces; The carbohydrate recognition domain regulates cell function". In: *Journal of Leukocyte Biology* 103.2, pp. 341–353.

Takenaka, Yukinori, Tomoharu Fukumori, and Avraham Raz (2002). "Galectin-3 and metastasis". In: *Glycoconjugate Journal* 19.7, pp. 543–549.

Yang, R Y *et al.* (1998). "Role of the carboxyl-terminal lectin domain in self-association of galectin-3". In: *Biochemistry* 37.12.

Yu, Lu-Gang *et al.* (2007). "Galectin-3 Interaction with Thomsen-Friedenreich Disaccharide on Cancer-associated MUC1 Causes Increased Cancer Cell Endothelial Adhesion". In: *Journal of biological chemistry* 282.1, pp. 773–781.

Appendix A

Interaction frequency data

Table A.1 provides the data used for calculating the interaction frequency (P_{int}) between Gal-3 WT and the negative control ligands.

Table A.1: Interaction frequency data for negative controls and the systems investigated in this thesis. The associated standard deviation (SD) is also included in the table.

Ligand	Bead pair no.[a]	No. of force curves	No. of interactions
Siglec9	1	150	6
	2	200	35
	3	120	52
AlgE4	1	50	0
	2	150	0
	3	50	0
	4	70	0
	5	100	39
	6	150	0
BSA	1	150	1
	2	150	2
	3	150	2
	4	150	3
	5	150	2
NH_2 beads	1	100	22[b]
	2	100	3[b]
	3	150	59
	4	50	1[b]

[a] For every bead pair were 3 different z-positions of the bead with ligands immobilized, used.
[b] After the specified number of force curves, the bead pair got stuck together due to very strong interactions, making the lasers unable to tear them apart.

Appendix B

DFS box plots

Figure B.1 presents box plots giving an interpretation of the variation in the rupture force within each subgroup in the DFS for all systems investigated in this thesis.

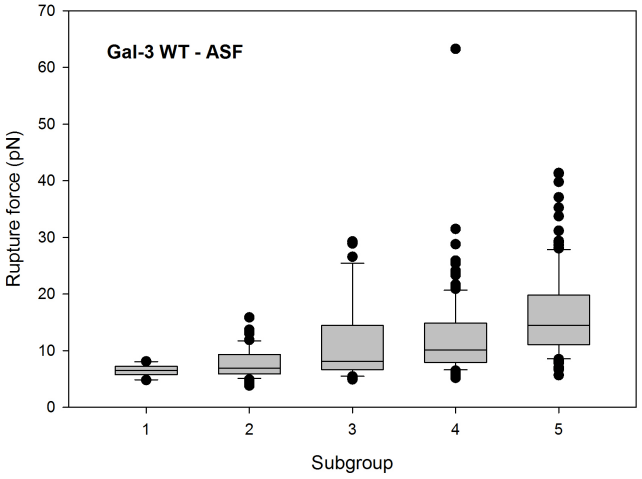

(a) Gal-3 WT - ASF

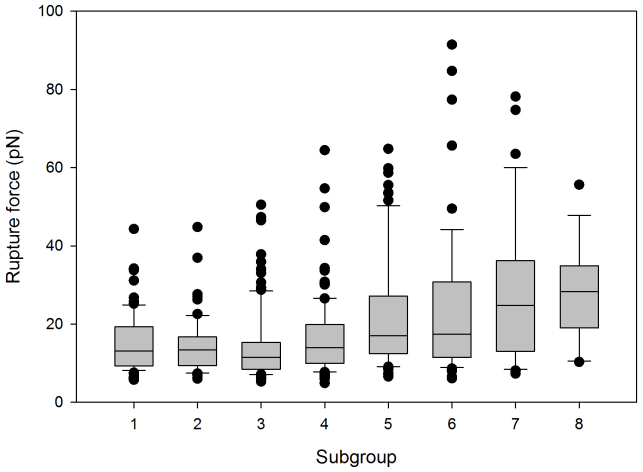

(b) Gal-3 HOMO - AFS

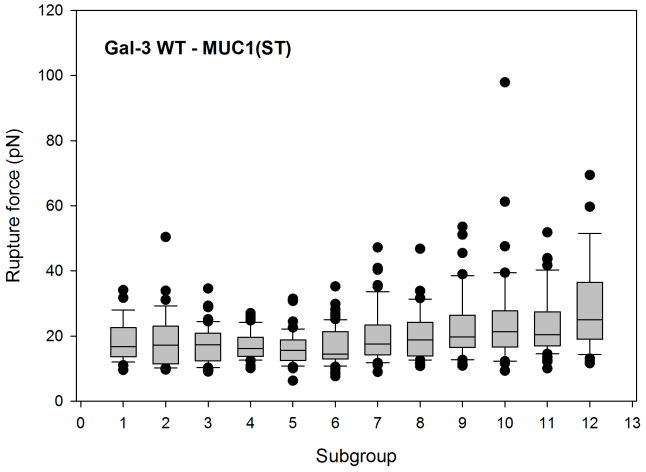

(c) Gal-3 WT - MUC1(ST)

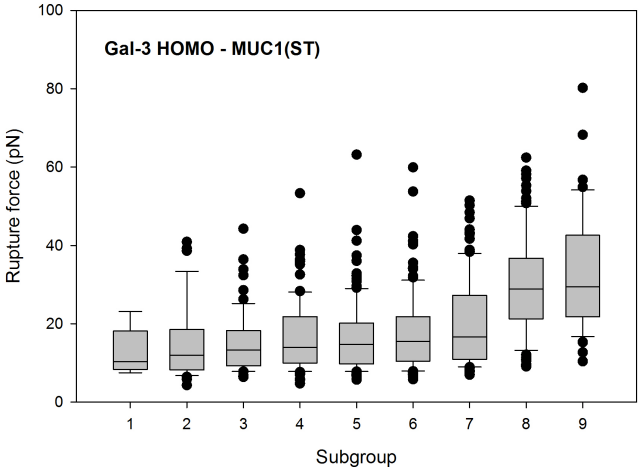

(d) Gal-3 HOMO - MUC1(ST)

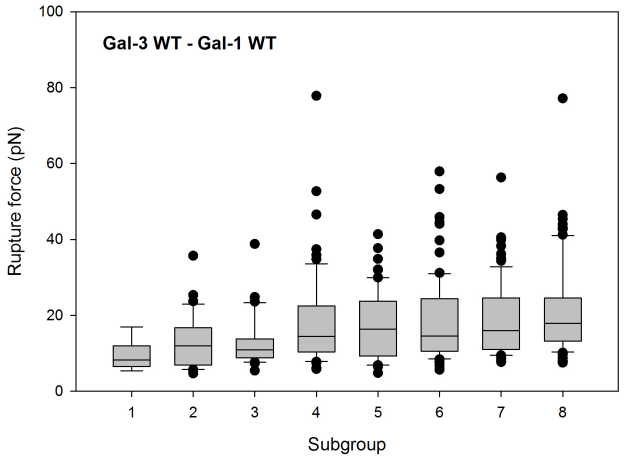

(e) Gal-3 WT - Gal-1 WT

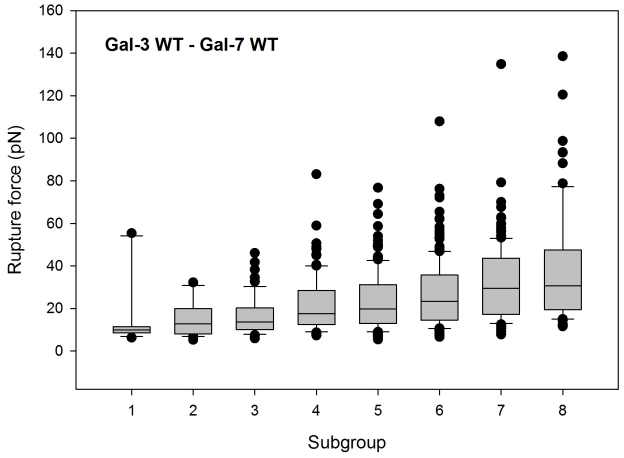

(f) Gal-3 WT - Gal-7 WT

Figure B.1: Box plots of all the dynamic force spectra showing the variation in each subgroup for each system indicated.